Electronic and Transport Properties in Mn-doped Silicon

Sekika Yamamoto

DISSERTATION IN PHYSICS

THE OSAKA UNIVERSITY

GRADUATE SCHOOL OF SCIENCE

TOYONAKA, OSAKA

Electronic and Transport Properties in Mn-doped Silicon

Sekika Yamamoto

Abstract

In this paper, the properties of Mn atoms doped in various Si hosts and their effects to the transport properties are investigated. For the former, DLTS, ESR, SIMS, PL and DC measurements are utilized, and for the latter, the cyclotron resonance measurement is done. The samples were prepaired by thermal diffusion technique after the deposition of Mn. The samples are quenched after diffusion to avoid the precipitation of Mn atoms. It is known that Mn atoms in n or p-type Si compensate the shallow impurities and ionize itself, and that a Mn atom easily form a complex with an acceptor. On the other hand, Mn atoms in pure Si retain their neutral feature because of the absense of shallow impurities and they are easy to form Mn_4 clusters while Coulomb repulsion prevents the clustering of Mn atoms in the n or p-type Si host. The ESR signal intensity of interstitialy configured Mn atoms are found to decrease rapidly for first 100 days even when the samples are put in room temperature while the density of Mn_4 clusters do not change so much. This decreasing feature seems due to the precipitation of Mn atom onto surface. The concentration of Mn_4 cluster is obtained to be under $10^{15}cm^{-3}$ by executing the Hall measurement, and its activation energy is found to be 227meV.

The width of the cyclotron resonance line for Si:Mn sample exhibits the remarkable broadening compared to host Si. This broadening is mainly due to Mn_4 formation because the line width do not decrease propotionaly to the concentration of interstitial Mn which is obtained by ESR measurement. But the width shows the initial decrease according to the decrease

of the ESR signal intensity of interstitial Mn atom. It is concluded that the scattering is mainly caused by Mn_4 cluster and partly by interstitial Mn atom. The temperature dependence of the line width is obtained to be about $T^{\frac{1}{2}}$, which is ascribed to the potential narrowing compared to that of the shallow impurities. The scattering by such narrow potential is treated by analogy with the scattering by the square well potential or the hard core potential.

Contents

1 Introduction 1

2 Theoretical Background 12

2.1 Cyclotron resonance in the classical region 12

2.2 General formulation of scattering relaxation time 17

2.3 Various scattering process in semiconductor 19

2.3.1 Acoustic deformation potential scattering 19

2.3.2 Ionized impurity scattering 20

2.3.3 Neutral impurity scattering 22

2.3.4 Other scattering mechanisms 25

2.4 Deep impurities in semiconductor 28

2.4.1 Formulation of impurity model in semiconductor . . 28

2.4.2 Effective mass approximation 31

2.4.3 Scattering state in crystal 34

2.5 Transition metals in silicon 35

2.5.1 Localized (3d) states in the crystal field 35

2.6 Scattering of electron by deep level center 36

2.6.1 Quantum well scattering and zero energy resonance 36

2.6.2 Spin scattering 43

3 Experimental Procedures 46

3.1 Sample preparation 46

3.2 Microwave Cyclotron Resonance 49

3.3 Far Infrared Cyclotron Resonance 51

3.4 Deep Level Transient Spectroscopy 51
3.5 Electron Spin Resonance 55
3.6 Photoluminescence 57
3.7 DC measurements 57

4 Experimantal Results **59**
4.1 DLTS measurements 59
4.2 Cyclotron resonance 61
4.3 ESR measurements 63
4.4 PL measurements 66
4.5 DC measurements 67
4.6 FIR cyclotron resonance 68
4.7 Room temperature postannealing 69
4.8 Stress effect on line width of cyclotron resonance 69

5 Discussions **72**
5.1 ESR, DLTS and DC measurements 72
5.2 Cyclotron resonance 75
5.3 Neutral impurity scattering 76
5.3.1 Spin scattering 76
5.3.2 Resonant scattering 78
5.4 Ionized impurity scattering 79

6 Conclusions **83**

Acknowledgement **86**

A Gauss-Neuton Fitting of resonance curve 87

1 Introduction

Investigations of carrier scattering in materials have been widely done since the earliest stages of solid state physics. When semiconductor devices such as the transistor were invented, it became essential to get improved knowledge of the scattering mechanisms of carriers to control the mobility and the conductivity which decide the response speed of the device. This need prompted many researchers to investigate the carrier scattering properties of semiconductors. Besides the technological requirement, pure physical interest also exist in the semiconductor scattering problem. The scattering problem is quantum mechanically expressed using the formalism of continuum eigenvalue problem and its study made rapid progress after the Lipmann-Schwinger formalism was developed.

Cyclotron resonance is one of the most useful techniques to investigate the scattering process in semiconductors. Cyclotron resonance in material was first predicted by W.Schockley [1] theoretically and observed by B.Lax [2] and G.Dresselhans et. al. [3] experimentally. This technique initially exhibited its usefulness in investigations of band structure as an almost unique method to decide the details of the band structure. After that, as the measurement technique improved, other applications of cyclotron resonance were developed. One of these is the application for investigation of scattering mechanisms of current carriers and another is to study the transient behavior of non equilibrium carrier systems. The former utilizes the fact that the cyclotron resonance line width is proportional to the inverse momentum relaxation time of the carrier. When the resonance

signal is measured using a fixed radio frequency and with varying magnetic field, the resonance line width is expressed as $\Delta B = 2B_c/\omega\tau$ where τ is the momentum relaxation time of the carrier which is related to the differential scattering cross section $\sigma(\theta, \phi)$ by the formula,

$$\frac{1}{\tau} = Nv\sigma_m = Nv \int (1 - \cos\theta)\sigma(\theta, \phi) d\Omega \qquad (1.0.1)$$

where N is the number of scatterers and v is the velocity of the electron. Usually, $\sigma(\theta, \phi)$ can be calculated by the Born approximation or by partial wave approximation techniques, and justified by comparing with experimental results. On the other hand, the transport properties are investigated by DC measurements in many cases. One of the advantages of using cyclotron resonance in investigating the transport properties compared to DC measurements is that cyclotron resonance does not require electrodes which may damage the sample surface. The presence of the electrodes also causes uncertainty in the measurements when the ohmic contact is not reliable, as is often the case in measurements on semiconductor at low temperatures. Moreover, when the carrier density is sufficiently small, the cyclotron resonance line width is almost independent of carrier density and it makes a more accurate determination of momentum relaxation time possible while DC measurements yield uncertainty caused by combining Hall and resistivity measurements.

The scattering mechanism of electrons by lattice vibrations have attracted attention and have been widely studied not only in semiconductors but also in metals because it is the most essential factor to decide high temperature resistivity in both cases. The process of this scattering was

first described by Bardeen and Shockley using their formulation of deformation potential, and showed that the inverse relaxation time of electrons is linearly dependent on temperature in metals and has $T^{3/2}$ dependence in semiconductors respectively. The main difference between scattering in semiconductors and metals is band degeneracy. In the case of non degenerate semiconductors, almost all electrons participate in the scattering process and the change of Boltzmann distribution with temperature also changes the mean scattering probability of electrons. This results in the factor $T^{\frac{1}{2}}$ multiplying the inverse relaxation time. On the other hand, in metals, electrons which may undergo scattering are restricted to only those that occupy states around the Fermi level due to its strong degeneracy. Therefore, the scattering probabilities for one scatterer are in many cases independent of temperature. The fact that only electrons around the Fermi level suffer scattering leads to the enhancement of the Shubnikov-de-Haas effect, and Kondo effect in the special case of metals with magnetic impurity.

The most interesting scattering problem in semiconductors is the case where the effective mass approximation may be used to describe the scatterer. In this case, the scattering problem can be handled as if electrons and scatterers were simply in vacuum. It is firstly justified by Erginsoy in the neutral impurity scattering case. He utilized Massey and Moiseiwitch's calculation of cross section for the scattering of an electron by a hydrogen atom in vacuum and derived the scattering cross section in a semiconductor by substituting the dielectric constant with that in the semiconductor,

and the electron mass with its effective mass. The effective mass approximation can equally well be applied to potential scattering and was used for the ionized impurity scattering problem where incident electrons can be regarded as electron plane wave. Conwell and Weisskopf (C-W) constructed a formula for ionized impurity scattering by setting a limi for the minimum scattering angle to avoid divergence in the integration of the cross section, and well explained experimental results. Brooks and Herring (B-H) used a screened coulomb potential for the scattering potential instead of C-W's physically unrealistic truncated potential, and extended the applicable region of C-W formula as a result.

As described above, the effective mass technique solved most scattering problems in semiconductors. However in the region where the effective mass approximation is not applicable, there are only a few articles which discuss the scattering problems.

In general, the effective mass approximation is good when the spatial extent of the impurity potential is large compared to the lattice constant, and can be described by a small number of Fourier components. If the impurity potential varies as rapidly as the lattice potential, the effective mass approximation is no longer applicable. The impurity level will deviate from the energy calculated by the effective mass theorem, and may construct a deep lying level in the band gap in many cases. The application of an effective-mass-like approach for such deep levels needs a large number of Fourier components to construct its potential. As a result it may need tens of thousands of Bloch functions to construct its wave func-

tion, whereas the usual effective mass approximation needs only one Bloch function. There are two usual approaches to the deep level problem. One starts from the theory for an extended potential, and the other starts from the localized features of the potential. In the former, an effective mass theory is evolved using bases which contain the localized feature such as Wannier functions instead of Bloch functions to expand the impurity Green's function. This enables us to construct impurity states with much smaller number of bases. The pioneering work for this method was done by Koster and Slater. Recently, this method was much advanced and led to an impurity Green's function method which includes a first principles calculation. This was applied to several types of point defects in Si such as lattice vacancies and gave substantial understanding to energy level, formation energy and so on. The second approach starts from localizability of the potential and can be represented by a cluster method which utilizes the shortness of the effective range of the impurity potential, and calculates the whole energy of the small cluster including a finite number of host atoms and an impurity. This method sometimes succeeds, but its results may be strongly affected by boundary conditions at the cluster surface which make the problem very difficult. Even in the case where the effective mass approximation is generally usable, the impurity potential often deviates from an ideal coulomb potential near the atom. This deviation is referred to as the central cell correction. If the impurity ground state energy lies near an energy where such corrections affect the coulomb potential, the ground state energy will be affected by the central

cell potential. Generally speaking, excited states are less affected by the central cell potential.

If we define a deep impurity as an impurity in which the ground state energy is dominated by a central cell potential, the effective mass approximation is no longer applicable. However, its ground state energy is not always deep and can have a shallow or even positive energy level. A positive energy state is referred to as the resonant state. Hjalmarson revealed theoretically that in the case of substitutional isoelectric deep impurities, the impurity binding energy is almost independent of band structure and only depends on the difference of atomic energy of the impurity to host atom. In the case of nitrogen impurities in $GaAs_xP_{1-x}$, the band edge energy of the Γ and X points move up and down according to the composition x, but the impurity state energy follows neither of these band energies and changes like a dangling bond energy. The nitrogen impurity binding energy can in fact be shallow with an appropriate value of x. If impurity energy goes into band continuum, it can not exist as a pure bound state and forms a resonant state. This state is also referred to as a virtual bound state and has rather localized feature around the impurity atom compared to an extended Bloch state. The energy of the resonant state is expressed mathematically in the complex plane and its imaginary part expresses the lifetime of the electron trapped to the localized states around the impurity. This resonant state efficiently scatters electrons whose energy coincides with the resonant state according to the Breit-Wigner formula. Sankey and Dow showed theoretically that this res-

onant scattering can occur, and dominates the low temperature mobility in the case of defects in GaAs. Fisher, Adams and O'Reilly reported that they observed resonant scattering by the central cell potential of Si and Sn impurities in $Al_{1-x}Ga_xAs$. They applied hydrostatic pressure to the sample to change the band edge energy, and observed the change of mobility with pressure caused by relative position of impurity level to band edge energy. They used the DC technique to observe such scattering, but it is likely that cyclotron resonance measurements may give more explicit results.

It is possible that both the ideal coulomb potential and the central cell potential equally affect the impurity scattering of electrons. El-Ghanem and Ridley calculated the scattering cross section and mobility analytically for a combined potential, but it has not yet been observed explicitly.

Besides the above described substitutional isoelectronic impurity, other types of impurities put into interstitial sites also form deep states in the band gap. Among them, transition metal impurities in Si have been investigated for a long period. DLTS and ESR measurements have revealed their energy level, spin state and hyperfine interactions with nuclei and so on. Unfortunately, theoretical treatment of these impurities lags behind experiment. Recent rapid progress using super computers now make first principle calculations possible. These calculations yield the results which explain the experimental data in certain problems. Zunger and Yoshida calculated the various characteristic values of transition metal impurities in Si using an impurity Green's function method, and explained the ex-

perimental result.

When a transition metal atom is put into vacuum, its d-electrons are configured according to the Fund's rule and tend to maximize their total spin. however if they are put into a material, the circumstance is different due to the existence of the crystal field. There are two approaches for the splitting of spin multiplets of d-electrons in the crystal field and they are generally complicated. One is called the weak crystal field method and the other is called the strong crystal field method. In general, if the crystal field energy is greater than the exchange energy among the d-electrons, the low spin state should be favorable because they tend to lower the crystal field energy by making their spins parallel each other even though it raises the exchange energy. On the other hand, if the crystal field energy is weaker than the exchange energy, the higher spin state becomes favorable. If transition metals are put into a semiconductor with high covalency such as Si, the crystal field energy is enhanced due to the hybridization of the metal d state and the semiconductor p state. On the other hand, p-d hybridization expands the d-electron wave function and therefore lowers the exchange energy. As a result, transition metal impurities tend to have low spin state compared to those in ionic crystals. Table 1 shows the spin state for various transition metal in Si interstitial sites given by Yoshida. Many of them are observed by ESR measurement. Another characteristic feature of transition metals in Si is that they can have many charge states. For example, it is known from calculation that interstitial Mn can exist with several charge states from Mn^{3+} to Mn^{-} (

Mn^{3+} has not yet been observed) by changing the Fermi level in the band gap. This behavior is caused by the strong covalency of Si. Because the d-electron wave function is extended due to the p-d hybridization caused by covalency, the correlation energy of d-electrons become as small as 0.1 eV $\sim$ 0.2 eV. The effects of these transition metal impurities on the scattering properties for conduction electrons have not been revealed yet.

Besides investigating the scattering properties, there is an approach to investigate the interaction of transition metal impurities in Si with conduction electrons, namely spin relaxation by conduction electrons. The excited spin state of a transition metal impurity relaxes when collisions with electrons occur. In general, spin-spin relaxation overwhelms the spin-lattice relaxation, and spin relaxation by collision with electrons may detected by ESR measurement when the number of conduction electrons is large enough. Vikhnin, Deigen, Semenov and Shanina calculated the spin relaxation rate for Fe impurities in Si by using the s-d exchange interaction formalism and by calculating the exchange integral. It is well known that the s-d spin exchange interaction causes the Kondo effect in 3d-spin doped metal. Similarly, spin-spin interaction can also cause momentum relaxation of electrons. Its cross section generally depends on the magnitude of spins and the exchange integral. The exchange integral can be deduced to be small in the case of deep impurities because of their localized feature. Vikhnin's calculation implies about 10^{-7} s relaxation time for s-d interaction caused momentum relaxation.

Calculations by Zunger and Yoshida showed the general low spin state

for transition metal impurities in Si, but they also showed that impurities such as Mn and Cr can have a high spin state.

As described above, transition metals in Si have two physical aspect. One is a deep impurity and the other is spin impurity. This work examines the electronic state of transition metal impurities in Si with special attention to Mn, and its effect on the electron scattering process by studying the cyclotron resonance line width and combined with other experimental methods.

Charge	Sc	Ti	Cr	Mn	Fe	Co	Ni	Cu
3+	NM	H/L	H/L	H		NM		
2+	H/L	H/L	H	H		L		
+	H/L	H/L	H	H	H	H/L		NM
0	H/L	L	H	H	H/L	H/L	NM	
-		L		H/L		NM		
2-		NM						

Table 1: Spin states calculated by Yoshida for various transition metals in Si interstitial site. NM means nonmagnetic, H means a high spin state and L means a low spin state. H/L means that either of a high or a low spin states can exist.

2 Theoretical Background

2.1 Cyclotron resonance in the classical region

When magnetic field H is applied to an electron, it is affected by the Lorentz force of $\dot{\boldsymbol{k}} = \frac{e}{c\hbar}\boldsymbol{v} \times \boldsymbol{H}$ and moves on the spiral trajectory. In solid state, electron group velocity is expressed as $\boldsymbol{v} = \frac{1}{\hbar}\nabla_{\boldsymbol{k}} E(\boldsymbol{k})$ so that the time variation of $\boldsymbol{k}$ must be perpendicular to both $\boldsymbol{H}$ and normal vector of iso-energy plane. Therefore the motion of electron in $\boldsymbol{k}$-space is bound in the closed curve on the iso-energy surface cut by the plane perpendicular to the magnetic field. If electron do not suffer any scattering, the period of motion is

$$T = \oint \frac{dk}{\dot{k}} = \oint \frac{dk}{\frac{e}{c\hbar} v H \sin\theta} = \frac{c\hbar}{eH} \oint \frac{dk}{v_\perp} \tag{2.1.1}$$

where θ is the angle of $\boldsymbol{v}$ and $\boldsymbol{H}$. Cyclotron frequency is defined as $\omega_c \equiv \frac{2\pi}{T}$. If we define the cyclotron effective mass as $m^*_H \equiv \frac{eH}{\omega_c c}$, it becomes

$$\begin{aligned} m^*_H &= \frac{eH}{c} \cdot \frac{T}{2\pi} \\ &= \frac{\hbar}{2\pi} \oint \frac{dk}{v_\perp} \\ &= \frac{\hbar^2}{2\pi} \oint \left(\frac{dE}{dk_\perp}\right)^{-1} dk \end{aligned} \tag{2.1.2}$$

where we used the relation $v_\perp = \frac{1}{\hbar}\frac{\partial E}{\partial k_\perp}$. In the case of free electron in vacuum where $E = \frac{\hbar^2 k^2}{2m_0}$, $k_\perp = k$, the cyclotron mass is the same to bare electron mass.

$$m^*_H = \frac{\hbar}{2\pi} \frac{m_0}{\hbar^2} \oint \frac{dk}{k} = m_0 \tag{2.1.3}$$

If the oscillating electric field is applied on such system, and if its frequency coincides to ω_c, electron resonantly absorb the energy of electric field and

will be accelerated. This is the so-called cyclotron resonance.

First, we should start from the classical Boltzmann equation to handle the statistical behavior of carriers. We can think of the distribution function $f(\boldsymbol{k}, \boldsymbol{r}, t)$. The Boltzmann equation is the equation represents the static state of the distribution function, therefore it is expressed as

$$\frac{\partial f}{\partial t}\Big]_{diffuse} + \frac{\partial f}{\partial t}\Big]_{field} + \frac{\partial f}{\partial t}\Big]_{scatter} = 0 \tag{2.1.4}$$

Making use of the Liouville's theorem, we can assume $f(\boldsymbol{k}, \boldsymbol{r}, t) = f(\boldsymbol{k}, \boldsymbol{r} - \boldsymbol{v}_k t, 0)$. Then the diffusion term becomes,

$$\frac{\partial f}{\partial t}\Big]_{diffuse} = -\boldsymbol{v}_k \cdot \nabla_r f(\boldsymbol{k}, \boldsymbol{r}, t) \tag{2.1.5}$$

When external field is applied, electron momentum changes due to Lorentz force of $\dot{\boldsymbol{k}} = \frac{e}{\hbar}(\boldsymbol{E} + \frac{1}{c}\boldsymbol{v}_k \times \boldsymbol{H})$. Again, Liouville's theorem allows us regarding $f(\boldsymbol{k}, \boldsymbol{r}, t) = f(\boldsymbol{k} - \dot{\boldsymbol{k}}t, \boldsymbol{r}, 0)$. Then the field term becomes,

$$\begin{aligned} \frac{\partial f}{\partial t}\Big]_{field} &= -\dot{\boldsymbol{k}} \cdot \nabla_k f(\boldsymbol{k}, \boldsymbol{r}, t) \\ &= -\frac{e}{\hbar}(\boldsymbol{E} + \frac{1}{c}\boldsymbol{v} \times \boldsymbol{H}) \cdot \nabla_k f(\boldsymbol{k}, \boldsymbol{r}, t) \end{aligned} \tag{2.1.6}$$

Distribution change also occurs when electrons are scattered by lattice or other scattering center. The way this happens accords the transition matrix element $W_{\boldsymbol{k}'\boldsymbol{k}}$ and distribution function of initial and final states of scattering.

$$\frac{\partial f}{\partial t}\Big]_{scatter} = \sum_{\boldsymbol{k}'} \left\{ W_{\boldsymbol{k}'\boldsymbol{k}} f(\boldsymbol{k}') \left[1 - f(\boldsymbol{k})\right] - W_{\boldsymbol{k}\boldsymbol{k}'} f(\boldsymbol{k}) \left[1 - f(\boldsymbol{k}')\right] \right\} \tag{2.1.7}$$

where

$$W_{\boldsymbol{k}\boldsymbol{k}'} = \frac{2\pi}{\hbar} |\left\langle \boldsymbol{k}' \right| T \left| \boldsymbol{k} \right\rangle|^2 \delta(E_i - E_f) \tag{2.1.8}$$

In the case of semiconductor, we can assume that the condition $f(\boldsymbol{k}) \ll 1$ is satisfied, the scattering term becomes

$$\left.\frac{\partial f}{\partial t}\right]_{scatter} = \sum_{\boldsymbol{k}'} \left\{ W_{\boldsymbol{k}'\boldsymbol{k}} f(\boldsymbol{k}') - W_{\boldsymbol{k}\boldsymbol{k}'} f(\boldsymbol{k}) \right\} \tag{2.1.9}$$

In the equilibrium condition which we represent by $f_0(\boldsymbol{k})$, the number of transition $\boldsymbol{k} \rightarrow \boldsymbol{k}'$ is equal to that of $\boldsymbol{k}' \rightarrow \boldsymbol{k}$ transition. This is called as the detailed balance and expressed by

$$W_{\boldsymbol{k}'\boldsymbol{k}} f_0(\boldsymbol{k}') = W_{\boldsymbol{k}\boldsymbol{k}'} f_0(\boldsymbol{k}) \tag{2.1.10}$$

which leads to

$$\begin{aligned} \left.\frac{\partial f}{\partial t}\right]_{scatter} &= \sum_{\boldsymbol{k}'} W_{\boldsymbol{k}\boldsymbol{k}'} \left\{ \frac{W_{\boldsymbol{k}'\boldsymbol{k}}}{W_{\boldsymbol{k}\boldsymbol{k}'}} f(\boldsymbol{k}') - f(\boldsymbol{k}) \right\} \\ &= -\sum_{\boldsymbol{k}'} W_{\boldsymbol{k}\boldsymbol{k}'} \left\{ f(\boldsymbol{k}) - \frac{f_0(\boldsymbol{k})}{f_0(\boldsymbol{k}')} f(\boldsymbol{k}') \right\} \end{aligned} \tag{2.1.11}$$

If we assume that all scattering processes is elastic, that is, $|\boldsymbol{k}| = |\boldsymbol{k}'|$ and $f_0(\boldsymbol{k}) = f_0(\boldsymbol{k}')$ is satisfied, the scattering term becomes

$$\begin{aligned} \left.\frac{\partial f}{\partial t}\right]_{scatter} &= -\sum_{\boldsymbol{k}'} W_{\boldsymbol{k}\boldsymbol{k}'} \left\{ f(\boldsymbol{k}) - f(\boldsymbol{k}') \right\} \\ &= -\frac{V}{(2\pi)^3} \int_{-\infty}^{\infty} d\boldsymbol{k}' W_{\boldsymbol{k}\boldsymbol{k}'} \left\{ f(\boldsymbol{k}) - f_0(\boldsymbol{k}) \right\} \\ &\quad \times \left[\frac{f(\boldsymbol{k}) - f_0(\boldsymbol{k}) + f_0(\boldsymbol{k}) - f(\boldsymbol{k}')}{f(\boldsymbol{k}) - f_0(\boldsymbol{k})} \right] \\ &= -\frac{g(\boldsymbol{k})}{\tau(\boldsymbol{k})} \end{aligned} \tag{2.1.12}$$

where,

$$g(\boldsymbol{k}) = f(\boldsymbol{k}) - f_0(\boldsymbol{k}) \tag{2.1.13}$$

$$\frac{1}{\tau(\boldsymbol{k})} = \frac{V}{(2\pi)^3} \int_{-\infty}^{\infty} d\boldsymbol{k}' W_{\boldsymbol{k}\boldsymbol{k}'} \left(1 - \frac{g(\boldsymbol{k}')}{g(\boldsymbol{k})} \right) \tag{2.1.14}$$

$\tau(\boldsymbol{k})$ is referred to as the momentum relaxation time. $g(\boldsymbol{k})$ is the deviation of distribution function from the equilibrium. When $g(\boldsymbol{k})$ is small, $g(\boldsymbol{k}')/g(\boldsymbol{k})$ can be approximated by $\cos\theta$ where θ is the scattering angle.

$$\frac{1}{\tau(\boldsymbol{k})} = \frac{V}{(2\pi)^3}\int_{-\infty}^{\infty} d\boldsymbol{k}' W_{\boldsymbol{k}\boldsymbol{k}'}(1-\cos\theta) \tag{2.1.15}$$

In the constant relaxation time approximation, it is assumed that the relaxation time is independent of $\boldsymbol{k}$. The distribution function attempt to recover the initial distribution with single exponential decay.

$$g(\boldsymbol{k},t) = g(\boldsymbol{k},0)\exp\left(-\frac{t}{\tau}\right) \tag{2.1.16}$$

and,

$$\left.\frac{\partial f}{\partial t}\right]_{scatter} = -\frac{1}{\tau}g(\boldsymbol{k},t) \tag{2.1.17}$$

Substituting (2.1.6) and (2.1.17) into (2.1.4), and neglecting spatial distribution, we obtain explicit expression of boltzmann equation for our problem.

$$-\frac{e}{\hbar}(\boldsymbol{E}+\boldsymbol{v}\times\boldsymbol{B})\cdot\nabla_{\boldsymbol{k}} f = -\frac{g}{\tau} \tag{2.1.18}$$

Using the effective mass m^* defined in section (2.4.2), we can use $\boldsymbol{v} = \frac{\hbar}{m^*}\boldsymbol{k}$ for electron velocity. The equation (2.1.18) becomes

$$g = \frac{\hbar e}{m^*}\frac{\tau}{1+(\omega_c\tau)^2}\frac{\partial f_0}{\partial E}\left[\boldsymbol{E}+\frac{e\tau}{m^*}(\boldsymbol{B}\times\boldsymbol{E})+\left(\frac{e\tau}{m^*}\right)^2(\boldsymbol{B}\cdot\boldsymbol{E})\boldsymbol{B}\right]\cdot\boldsymbol{k} \tag{2.1.19}$$

where $w_c = \frac{eB}{m^*}$ is the cyclotron frequency and

$$\nabla_{\boldsymbol{k}} f_0 = \frac{\partial f_0}{\partial E}\nabla_{\boldsymbol{k}} E = \frac{\partial f_0}{\partial E}\hbar v_{\boldsymbol{k}} \tag{2.1.20}$$

was used.

Here we assume for the simplicity $\boldsymbol{E} = (E_x, E_y, 0)$ and $\boldsymbol{B} = (0,0,B)$ and

express (2.1.19) as $g = \boldsymbol{c} \cdot \boldsymbol{k}$ which leads to

$$\begin{cases} c_x &= \dfrac{e\tau}{m^*} \dfrac{\tau}{1+(\omega_c\tau)^2} \dfrac{\partial f_0}{\partial E} [E_x - \omega_c \tau E_y] \\ c_y &= \dfrac{e\tau}{m^*} \dfrac{\tau}{1+(\omega_c\tau)^2} \dfrac{\partial f_0}{\partial E} [E_y + \omega_c \tau E_x] \\ c_z &= 0 \end{cases} \tag{2.1.21}$$

and

$$\begin{aligned} g &= c_x k_x + c_y k_y \\ &= ev_x \frac{\partial f_0}{\partial E} \left[\frac{\tau}{1+(\omega_c\tau)^2} E_x - \frac{\omega_c \tau^2}{1+(\omega_c\tau)^2} E_y \right] \\ &\quad + ev_y \frac{\partial f_0}{\partial E} \left[\frac{\omega_c \tau^2}{1+(\omega_c\tau)^2} E_x + \frac{\tau}{1+(\omega_c\tau)^2} E_y \right] \end{aligned} \tag{2.1.22}$$

Using the obtained distribution function we can evaluate the current density.

$$\begin{aligned} \boldsymbol{J} &= \frac{1}{(2\pi)^3} \int d^3k (-e\boldsymbol{v}) f(\boldsymbol{k}) \\ &= -\frac{e}{(2\pi)^3} \int d^3k \boldsymbol{v} g(\boldsymbol{k}) \end{aligned} \tag{2.1.23}$$

Substituting (2.1.22) into (2.1.23),

$$J_x = \frac{ne^2}{m^*} \left[\left\langle \frac{\tau}{1+(\omega_c\tau)^2} \right\rangle E_x - \left\langle \frac{\omega_c\tau^2}{1+(\omega_c\tau)^2} \right\rangle E_y \right] \tag{2.1.24}$$

$$J_y = \frac{ne^2}{m^*} \left[\left\langle \frac{\omega_c\tau^2}{1+(\omega_c\tau)^2} \right\rangle E_x + \left\langle \frac{\tau}{1+(\omega_c\tau)^2} \right\rangle E_y \right] \tag{2.1.25}$$

To evaluate the interaction of carrier with light field, we can think of the simple vibrating field, $E_x = E_{0x} e^{i\omega t}, E_y = E_{0y} e^{i\omega t}$. The light absorption can be obtained using Joule's formula.

$$\begin{aligned} P(\omega) &= \overline{Re(\boldsymbol{J}) \cdot Re(\boldsymbol{E})} = \frac{1}{2} Re(\boldsymbol{J} \cdot \boldsymbol{E}^*) \\ &= \frac{ne^2 \langle\tau\rangle}{4m^*} E_0^2 \left[\frac{1}{(\omega-\omega_c)^2 \langle\tau\rangle^2 + 1} + \frac{1}{(\omega+\omega_c)^2 \langle\tau\rangle^2 + 1} \right] \end{aligned} \tag{2.1.26}$$

Translating this into the function of magnetic field using $\omega_c = \dfrac{eB}{m^*}$,

$$P(B) = \frac{ne^2\langle\tau\rangle}{4m^*}E_0^2\left[\frac{1}{(B-B_c)^2\left(\frac{e\langle\tau\rangle}{m^*}\right)^2+1}+\frac{1}{(B+B_c)^2\left(\frac{e\langle\tau\rangle}{m^*}\right)^2+1}\right] \tag{2.1.27}$$

where

$$B_c = \frac{m^*\omega}{e} \tag{2.1.28}$$

This shows the absorption peak at $B = \pm B_c$ from which we can evaluate the effective mass of carrier. Here we have the classical cyclotron resonance absorption of light by carriers with a effective mass.

By observing the cyclotron resonance line width, we can evaluate the momentum relaxation time by utilizing the relation

$$\Delta B = \frac{B_c}{\omega\langle\tau\rangle} \tag{2.1.29}$$

where ΔB is the half width of absorption curve.

2.2 General formulation of scattering relaxation time

In usual scattering theory, a scattering relaxation time for one particle is expressed as

$$\tau = \frac{1}{N_I v\sigma} \tag{2.2.1}$$

where N_I is the number of scattering center, v the particle velocity and σ the scattering cross section.

$$\begin{aligned}\sigma &= \int\sigma(\theta,\phi)d\Omega \\ &= 2\pi\int_{-\pi}^{\pi}|f(\theta)|^2\sin\theta d\theta\end{aligned} \tag{2.2.2}$$

where $f(\theta)$ is the scattering amplitude and is appear in the boundary condition for the Schrödinger equation in the scattering problem.

$$\Phi^{(+)} \sim e^{i\boldsymbol{k}\cdot\boldsymbol{r}} + \frac{e^{ikr}}{r} f(\theta) \qquad (r \to \infty) \tag{2.2.3}$$

$f(\theta)$ can be expressed in the partial wave technique as

$$f(\theta) = \sum_{l=0}^{\infty} \frac{i}{2k}(2l+1)\exp(i\delta_l)\sin\delta_l P_l(\cos\theta) \tag{2.2.4}$$

where $P_l(\cos\theta)$ is Legendre Polynomial. Substituting (2.2.4) into (2.2.2), we get the total scattering cross section.

$$\sigma = \frac{4\pi}{k^2}\sum_{l=0}^{\infty}(2l+1)\sin^2\delta_l \tag{2.2.5}$$

where δ_l is referred to as the phase shift of l-th partial wave. The partial wave approximation which omits the partial wave with large l is only applicable when the spatial extension of scattering potential is under several times of electron de Bloglie wave length of the electron. That is the case that electron velocity is so small. In the case of such low energy scattering, cross section is usually concerned to a few of lowest l-th partial wave.

In the transport problem, the momentum transfer cross section σ_m is more important instead of (2.2.5)

$$\begin{aligned} \sigma_m &= \int(1-\cos\theta)\,|f(\theta)|^2\,d\Omega \\ &= \frac{4\pi}{k^2}\sum_{l=0}^{\infty}(l+1)\sin^2(\delta_l - \delta_{l+1}) \end{aligned} \tag{2.2.6}$$

Indeed, in the case that electron velocity is very small as in the case of low temperature electron scattering in semiconductor, σ and σ_m can be regarded to be the same since the condition $\delta_{l+1} \ll \delta_l$ is satisfied. As the

velocity of electron rises, the partial wave technique becomes more difficult and instead, the Born approximation becomes applicable in which $f(\theta)$ is approximated using the transition matrix element.

$$f(\theta) = -\frac{1}{4\pi}\left(\frac{2m}{\hbar^2}\right)\langle \boldsymbol{k}'|\, V\, |\boldsymbol{k}\rangle \tag{2.2.7}$$

where θ is the angle between $\boldsymbol{k}'$ and $\boldsymbol{k}$. This leads to the momentum relaxation time expressed in (2.1.15) and usually easy to solve. But the partial wave treatment using (2.2.6) is more accurate for scattering of slow particle.

In the non degenerate semiconductor where all of the electrons participate in the scattering, it is necessary to take thermal average with Boltzmann distribution to compare with the scattering relaxation time obtained by experiment.

$$\langle\tau\rangle = \frac{\int_0^\infty \tau\epsilon^{\frac{3}{2}} \exp\left(-\frac{\epsilon}{k_BT}\right) dE}{\int_0^\infty \epsilon^{\frac{3}{2}} \exp\left(-\frac{\epsilon}{k_BT}\right) dE} \tag{2.2.8}$$

when τ is a power of ϵ, that is, $\tau = a\epsilon^s$, it becomes

$$\begin{aligned}\langle\tau\rangle &= a(k_BT)^s \frac{\Gamma(\frac{5}{2}+s)}{\Gamma(\frac{5}{2})} \\ &= \frac{4}{3\sqrt{\pi}} a(k_BT)^s \Gamma\left(\frac{5}{2}+s\right)\end{aligned} \tag{2.2.9}$$

2.3 Various scattering process in semiconductor

Here we briefly survey the various scattering processes in semiconductor.

2.3.1 Acoustic deformation potential scattering

Acoustic phonon scattering problem is treated first in history among various scattering processes in solid, because for the most part it dominates

the room temperature mobility of metals and semiconductors.

Bardeen and Shockley [4] derived that the interaction of an electron with acoustic phonon can be expressed as $\delta\epsilon = \epsilon_{ac}(\nabla_r \cdot \delta \boldsymbol{r})$ where ϵ_{ac} is the acoustic deformation potential constant. The obtained relaxation time is expressed by

$$\frac{1}{\langle\tau\rangle} = \frac{3m^{*\frac{3}{2}}\epsilon_{ac}^2(k_BT)^{\frac{3}{2}}}{2^{\frac{3}{2}}\pi^{\frac{1}{2}}\hbar^4\rho v_s^2} \tag{2.3.1}$$

where ρ is the crystal density, $v_s = \frac{\omega_q}{q}$ the sound velocity. This shows that the cyclotron resonance line broadening caused by acoustic phonon scattering has the temperature dependence of $T^{\frac{3}{2}}$. This partly comes from the temperature dependence of the number of phonon that is proportional to the temperature and partly from that of electron mean velocity according to equation (2.2.1) which has the temperature dependence of $T^{\frac{1}{2}}$.

2.3.2 Ionized impurity scattering

Ionized impurity scattering dominates the low temperature mobility of semiconductors especially in the case that the compensation is rather strong. The first formulation of this type of scattering has been done by E.Conwell and V.F.Weisskopf.[5] They used the model potential in which the bare coulomb potential is interrupted at the certain length to avoid the divergence of the cross section at small scattering angle. They set one-half the average distance between neighboring impurities as the cut-off length. They obtained the following formula based on the Born approximation,

$$\tau = \frac{\kappa^2(2m^*)^{\frac{1}{2}}\epsilon^{\frac{3}{2}}}{\pi e^4 N_I \ln[1 + (2ka)^2(\kappa^2\hbar^2\epsilon/2m^*e^4)]} \tag{2.3.2}$$

where N_I is the concentration of ionized impurities, κ the dielectric constant, ϵ the electron energy, e the electronic charge and a the cut-off length defined by

$$a = \frac{1}{2\sqrt{N_I}} \tag{2.3.3}$$

This formula is applicable when the compensation is small and free carrier density is relatively low. The threshold density for ionized impurities is $N_I = 10^{17} cm^{-3}$ in the case ot n-type Ge.

Brooks and Herring [6], on the other hand, suggested that instead of the cut-off length, the screened coulomb potential should be used. They obtained the formula based on the Born approximation.

$$\tau = \frac{\kappa^2 (2m^*)^{\frac{1}{2}} \epsilon^{\frac{3}{2}}}{\pi e^4 N_I \left\{ \ln[1 + (2k\lambda)^2] - \frac{1}{1+1/(2k\lambda)^2} \right\}} \tag{2.3.4}$$

where λ is the Debye-Hückel screening length defined by

$$\lambda = \left(\frac{\kappa k_B T}{4\pi e^2 n} \right)^{\frac{1}{2}} \tag{2.3.5}$$

In either case above two formulas have the energy dependence of $\epsilon^{\frac{3}{2}}$. We can expect that the scattering rate thus, the line-broadening of the cyclotron resonance has the $T^{-\frac{3}{2}}$ dependence by considering the equations (2.1.29) and (2.2.9). Brooks-Herring formula is widely used as the standard formula for the ionized scattering in semiconductors. But it is based on the Born approximation which is not applicable to low energy scattering as in the case of the electron scattering at low temperature in semiconductors. Sclar [7] derived another formulation by use of partial wave method. He approximated the attractive and repulsive coulomb potential by a square well with radius a and depth V and a square barrier

with radius a and height V, respectively. He obtained the formula for the repulsive potential

$$\tau = \frac{(2m^*)^{\frac{1}{2}}\epsilon^{-\frac{1}{2}}}{8\pi N_I a^2}\left(\frac{\tanh \alpha a}{\alpha a} - 1\right)^{-\frac{1}{2}} \tag{2.3.6}$$

where

$$\alpha = \left[k^2 - \left(\frac{2m^*V}{\hbar^2}\right)a^2\right]^{\frac{1}{2}} \tag{2.3.7}$$

and for the attractive potential

$$\tau = \frac{(2m^*)^{\frac{1}{2}}\epsilon^{-\frac{1}{2}}}{8\pi N_I a^2}\left(\frac{\tan \alpha a}{\alpha a} - 1\right)^{-\frac{1}{2}} \tag{2.3.8}$$

It can be easily seen that these two formulas yields the $T^{\frac{1}{2}}$ dependence of cyclotron resonance line width both for the attractive and for the repulsive potential.

While Sclar used the square potential approximation, Blatt [8] evaluated the scattering rate for the ionized impurity based on the static screened coulomb potential by partial wave method and obtained the numerical result. After that, El-Ghanem and Ridley [9] developed the problem as the scattering by the co-existing system, i.e., the coulomb potential and the central cell potential.

2.3.3 Neutral impurity scattering

The neutral impurity scattering in semiconductors was firstly formulated by Erginsoy [10] who utilized the result of numerical calculation of scattering cross section on the electron-Hydrogen atom by Massey and Moiseiwitch [11] and extended it to the scattering problem in semiconductor by

replacing electron mass with the effective mass and vacuum electric susceptibility with that of semiconductor. Massey and Moiseiwitsch's result for the scattering cross section is approximated by

$$\sigma = \frac{20 a_B}{k} \tag{2.3.9}$$

where $a_B = \frac{4\pi\kappa_0\hbar^2}{me^2}$ is the Bohr radius of Hydrogen atom. Erginsoy derived the following inverse relaxation time for electron-neutral donor scattering by replacing a_B with an effective Bohr radius $a_B = \frac{m}{m^*}\kappa$

$$\begin{aligned} \frac{1}{\tau} = Nv\sigma &= \frac{20 N v a_B^*}{k} \\ &= \frac{20 a_B^* \hbar N}{m^*} \end{aligned} \tag{2.3.10}$$

where $v = \frac{\hbar k}{m^*}$ is used.

Erginsoy's result holds true for the neutral donors which are well approximated by the effective mass theory. The extensions of Erginsoy's result to the impurities which deviate from the effective mass theory has been tried by many researchers but there has not yet been explicit agreement with experiments. As for the usual shallow impurity scattering in semiconductor, Erginsoy's theory well accounts for the low temperature mobility of semiconductor under the condition that the number of ionized impurities is negligible.

Erginsoy's result is for neutral donors. In the case of scattering of electron by neutral acceptor, the situation is not the same. In the case of donors, the particle bound by the impurity is an electron and the analogy to e-H scattering is suitable where the electron-electron exchange interaction affect the cross section effectively. On the other hand, acceptor

atom binds an hole and there is no exchange with an incident electron. Its scattering process should be considered on the analogy of positron-Hydrogen atom scattering instead of electron-Hydrogen atom scattering. This problem is vigorously investigated by Otsuka et. al. [12] Their theoretical analysis based on Schwartz's calculation for e^+-H scattering cross section and obtained the inverse relaxation time for electron neutral acceptor scattering as

$$\frac{1}{\langle\tau\rangle} = 3.4 N_A \frac{\hbar}{m^*} \left(\frac{\hbar^2}{2m^* k_B}\right)^{\frac{3}{2}} \left(12.5T + \frac{\hbar^2}{2m^* k_B a_B^*}\right)^{-\frac{3}{2}} a_B^{*-2} \qquad (2.3.11)$$

where N_A is the density of neutral acceptors and $\langle\ \ \rangle$ means the thermal average. This formula exhibits slight temperature dependence. For low temperature limit,

$$\frac{1}{\langle\tau\rangle} \sim 3.4 \frac{\hbar a_B^* N_A}{m^*} \qquad (2.3.12)$$

If the impurity is double donor or double acceptor, it can be treated on the analogy of electron-Helium atom and positron-Helium atom scattering respectively. Kestner et al. [13] calculated the cross section for e-He and e^+-He scattering. The inverse relaxation time for low temperature obtained from their result is; For e-He scattering,

$$\frac{1}{\langle\tau\rangle} = 22.5 a_B^* N_I \left(\frac{3k_B T}{m^*}\right)^{\frac{1}{2}} \qquad (2.3.13)$$

and for e^+-He scattering,

$$\frac{1}{\langle\tau\rangle} = 0.25 \frac{\hbar a_B^*}{m^*} N_I \qquad (2.3.14)$$

2.3.4 Other scattering mechanisms

Besides the scattering mechanisms described above, there are many scattering processes in semiconductor.

- Non-polar optical deformation potential scattering

  The interaction energy of an electron with optical phonon is expressed as,

$$\delta\epsilon = D\delta r \tag{2.3.15}$$

  where D is the optical deformation potential constant. The scattering matrix element for this interaction is given by

$$|M_{k\pm q,k}| = D\left[\frac{\left(N_q + \frac{1}{2} \mp \frac{1}{2}\right)\hbar}{2\rho V\omega_0}\right]^{\frac{1}{2}} \tag{2.3.16}$$

  where ρ is the density of crystal and N_q is the mean number of phonon.

$$\begin{aligned} N_q &= \left[\exp\left(\frac{\hbar\omega_0}{k_BT}\right) - 1\right]^{-1} \\ &= \left[\exp\left(\frac{\Theta}{T}\right) - 1\right]^{-1} \end{aligned} \tag{2.3.17}$$

  and $\Theta = \frac{\hbar\omega_0}{T}$ is the Debye temperature. The result for the momentum relaxation time is,

$$\frac{1}{\langle\tau\rangle} = \frac{3m^{\frac{3}{2}}D^2}{4\sqrt{2\pi}\hbar^2\rho(k_B\Theta)^{\frac{1}{2}}f\left(\frac{T}{\Theta}\right)} \tag{2.3.18}$$

  where

$$f\left(\frac{T}{\Theta}\right) = (2z)^{\frac{5}{2}}(e^{2z} - 1)\int_0^\infty \frac{y^{\frac{3}{2}}e^{-2zy}dy}{\sqrt{y+1} + e^{2z}Re\{\sqrt{y-1}\}} \tag{2.3.19}$$

$$z = \frac{\Theta}{2T}, \qquad y = \frac{\epsilon}{k_B\Theta}$$

  Optical deformation potential scattering is not effective at low temperature because the number of optical phonon is so small.

- Piezo electric scattering

  If a crystal has the piezo electricity, electron scattering caused by the potential energy due to phonon polarization may occur. The potential energy is expressed as

$$\delta\epsilon = \frac{|e|\, e_{pz}}{\kappa\kappa_0 q}(\nabla_r \cdot \delta r) \tag{2.3.20}$$

  where e_{pz} is the piezo electric constant, κ the dielectric constant and q is the phonon wave number. The matrix element for the scattering is

$$|H_{k'k}| = \frac{|e|\, e_{ps}}{\kappa\kappa_0 q}\left(\frac{k_B T}{2V c_l}\right)^{\frac{1}{2}} = \left(\frac{e^2 K^2 k_B T}{2V\kappa\kappa_0 q^2}\right)^{\frac{1}{2}} \tag{2.3.21}$$

  where V is the volume of unit cell, $c_l = \rho\omega_l^2/q_l^2$ the elastic constant and

$$\frac{K^2}{1-K^2} = \frac{e_{pz}^2}{\kappa\kappa_0 c_l} \tag{2.3.22}$$

  where K^2 is called as an electro-mechanical coupling coefficient. The momentum relaxation time is

$$\frac{1}{\langle\tau\rangle} = \frac{3m^{\frac{1}{2}} e^2 K^2 (k_B T)^{\frac{1}{2}}}{2^{\frac{9}{2}}\sqrt{\pi}\hbar^2\kappa\kappa_0} \tag{2.3.23}$$

  which has $T^{\frac{1}{2}}$ dependence on temperature, but it is not effective for the non-piezoelectric crystal like Si.

- Polar optical deformation scattering

  In the semiconductor with large ionicity, the interaction of carrier with optical phonon is strong, and it yields large deformation energy and causes the scattering of carrier. The potential energy is expressed as

$$\delta\epsilon = \frac{|e|\, E}{q} \tag{2.3.24}$$

where E is the electric field caused by the polarization P, and

$$E = -\frac{P}{k_0} = -\frac{N_u e_c \delta r}{\kappa_0 q} \tag{2.3.25}$$

where N_u is the number of lattice point in the unit cell and e_c is the Callen effective charge

$$e_c = \omega_l \left[\frac{\kappa_0(\kappa_{opt}^{-1} - \kappa^{-1})M}{N_u}\right]^{\frac{1}{2}} \tag{2.3.26}$$

where M is the reduced atomic mass.

The matrix element becomes

$$|H_{k\pm q,k}|^2 = \frac{2^{\frac{3}{2}}\pi\hbar\alpha(\hbar\omega_0)^{\frac{3}{2}}}{Vm^{\frac{1}{2}}q^2}\left(N_u + \frac{1}{2} \mp \frac{1}{2}\right) \tag{2.3.27}$$

where

$$\alpha = \frac{\hbar\,|e|\,E_0}{2^{\frac{1}{2}}m^{\frac{1}{2}}(\hbar\omega_0)^{\frac{3}{2}}} \tag{2.3.28}$$

$$E_0 = \frac{|e|\,mk_B\Theta}{4\pi\kappa_0\hbar^2}(\kappa_{opt}^{-1} - \kappa^{-1}) \tag{2.3.29}$$

α is referred to as the polar constant.

The momentum relaxation time is

$$\frac{1}{\langle\tau\rangle} = \alpha\omega_o\left(\frac{\hbar\omega_0}{\epsilon}\right)^{\frac{1}{2}} N_q\left[\ln\left|\frac{a+1}{a-1}\right| + \exp\left(\frac{\Theta}{T}\right)\ln\left|\frac{1+b}{1-b}\right|\right] \tag{2.3.30}$$

where

$$a = \left[1 + \frac{\hbar\omega_0}{\epsilon}\right]^{\frac{1}{2}}, \qquad b = Re\left[1 - \frac{\hbar\omega_0}{\epsilon}\right]^{\frac{1}{2}} \tag{2.3.31}$$

When $T \ll \Theta$ is satisfied, the conditions $\epsilon \ll \hbar\omega_0$, $b \sim 0$, and $N_q \sim \exp\left(-\frac{\Theta}{T}\right)$ are also satisfied. Then momentum relaxation time becomes

$$\frac{1}{\langle\tau\rangle} = 2\alpha\omega_0 \exp\left(-\frac{\Theta}{T}\right) \tag{2.3.32}$$

2.4 Deep impurities in semiconductor

2.4.1 Formulation of impurity model in semiconductor

The problem of impurities in solid state can be attributed to solve an static Schrödinger equation.

$$\mathcal{H}\left|\phi\right\rangle = E\left|\phi\right\rangle \tag{2.4.1}$$

$$\mathcal{H} = \mathcal{H}_0 + U(\boldsymbol{r}) \tag{2.4.2}$$

where $\mathcal{H}_l$ is the host crystal Hamiltonian which includes the kinetic energy of electron (or hole) and periodic lattice potential, and $U(\boldsymbol{r})$ is the additional potential energy due to the existence of impurity. Now we expand $\left|\phi\right\rangle$ with complete set of Bloch function $\left|\boldsymbol{k}\right\rangle$ which is eigen states of $\mathcal{H}_0$, that is, $\mathcal{H}_0\left|\boldsymbol{k}\right\rangle = E_{\boldsymbol{k}}\left|\boldsymbol{k}\right\rangle$.

$$\left|\phi\right\rangle = \sum_{\boldsymbol{k}}\left|\boldsymbol{k}\right\rangle\left\langle\boldsymbol{k}|\phi\right\rangle = \sum_{\boldsymbol{k}}\left|\boldsymbol{k}\right\rangle\phi(\boldsymbol{k}) \tag{2.4.3}$$

Here, We call $\phi(\boldsymbol{k})$ "Bloch representation of $\left|\phi\right\rangle$". Equation(2.4.1) becomes,

$$\sum_{\boldsymbol{k}} E_{\boldsymbol{k}}\left|\boldsymbol{k}\right\rangle\phi(\boldsymbol{k}) + U(\boldsymbol{r})\sum_{\boldsymbol{k}}\left|\boldsymbol{k}\right\rangle\phi(\boldsymbol{k}) = E\sum_{\boldsymbol{k}}\left|\boldsymbol{k}\right\rangle\phi(\boldsymbol{k}) \tag{2.4.4}$$

multiplying $\left\langle\boldsymbol{k}'\right|$ from the left hand side of the equation (2.4.4) and replacing $\boldsymbol{k}$ and $\boldsymbol{k}'$,

$$(E_{\boldsymbol{k}} - E)\phi(\boldsymbol{k}) + \sum_{\boldsymbol{k}'} U(\boldsymbol{k},\boldsymbol{k}')\phi(\boldsymbol{k}') = 0 \tag{2.4.5}$$

where $U(\boldsymbol{k},\boldsymbol{k}') = \left\langle\boldsymbol{k}\right| U(\boldsymbol{r})\left|\boldsymbol{k}'\right\rangle$. This equation is to be applied to all appropriate $\boldsymbol{k}$ exists. So, this is the set of linear equation about $\phi(\boldsymbol{k})$'s and has nonzero solution when the secular determinant of equations (2.4.5)

vanishes. And this restriction leads eigenenergy E_n and set of eigenvector $\{\phi_n(\boldsymbol{k})\}$. For the bound state, expectation value of the velocity must be zero, that is,

$$\langle v \rangle = \left\langle \frac{1}{\hbar} \frac{\partial E}{\partial \boldsymbol{k}} \right\rangle = 0$$

Then, nonzero $\phi(\boldsymbol{k})$ constructing $\phi(\boldsymbol{r})$ must be taken from the area centered at critical point of $\boldsymbol{k}$ space. It may be maximum (M_1), minimum (M_2) or saddle (M_3) point. So, we should divide $\boldsymbol{k}$–space into subzone Ω_i centered at ith critical point.

In the region $\boldsymbol{k} \in \Omega_i$, equation (2.4.5) becomes

$$(E_{\boldsymbol{k}} - E)\phi_i(\boldsymbol{k}) + \sum_j \sum_{\boldsymbol{k}' \in \Omega_j} U_{ij}(\boldsymbol{k}, \boldsymbol{k}')\phi(\boldsymbol{k}') = 0 \qquad (2.4.6)$$

Where,

$$\phi(\boldsymbol{k}) = \begin{cases} \phi_1(\boldsymbol{k}) & for \quad \boldsymbol{k} \in \Omega_1 \\ \phi_2(\boldsymbol{k}) & for \quad \boldsymbol{k} \in \Omega_2 \\ \vdots & \vdots \end{cases}$$

In general case, $|\phi\rangle$ may be expressed as

$$|\phi\rangle = \sum_i \sum_{\boldsymbol{k}' \in \Omega_j} |\boldsymbol{k}\rangle \, \phi(\boldsymbol{k}) \qquad (2.4.7)$$

If the intervallay transition matrix element $U_{ij}(\boldsymbol{k}, \boldsymbol{k}')$ is very small compared to internal matrix element, we can neglect $U_{ij}(i \neq j)$, equation(2.4.6) becomes,

$$(E_{\boldsymbol{k}} - E)\phi_i^0(\boldsymbol{k}) + \sum_{\boldsymbol{k}' \in \Omega_i} U_{ii}(\boldsymbol{k}, \boldsymbol{k}')\phi_i^0(\boldsymbol{k}') = 0 \qquad (2.4.8)$$

from which we can obtain solutions E_{in}^0 and $\phi_{in}^0(\boldsymbol{k})$ for the first approximation. $\phi_{in}^0(\boldsymbol{k})$ should taken to be normalized and orthogonalized.

$$\sum_{\boldsymbol{k} \in \Omega_i} \phi_{in}^0(\boldsymbol{k})\phi_{in'}^0(\boldsymbol{k}) = \delta_{nn'} \qquad (2.4.9)$$

To estimate the effect of intervalley mixing, $\phi_i(\boldsymbol{k})$ can be expanded using $\phi^0_{in}(\boldsymbol{k})$,

$$\phi_i(\boldsymbol{k}) = \sum_n C_{in}\phi^0_{in}(\boldsymbol{k}) \tag{2.4.10}$$

and substituting this into equation (2.4.6), we get

$$(E_k - E)\sum_n C_{in}\phi^0_{in}(\boldsymbol{k}) + \sum_j \sum_{\boldsymbol{k}'\in\Omega_j} U_{ij}(\boldsymbol{k},\boldsymbol{k}')\sum_n C_{jn}\phi^0_{jn}(\boldsymbol{k}) = 0 \tag{2.4.11}$$

By utilizing the relation (2.4.8), this equation becomes,

$$\sum_n (E^0_{in} - E)C_{in}\phi^0_{in}(\boldsymbol{k}) + \sum_{i\neq j}\sum_n C_{jn} \sum_{\boldsymbol{k}'\in\Omega_j} U_{ij}(\boldsymbol{k},\boldsymbol{k}')\phi^0_{jn}(\boldsymbol{k}) = 0 \tag{2.4.12}$$

Multiplying $\sum_{\boldsymbol{k}\in\Omega_i}\phi^0_{in'}(\boldsymbol{k})$ from left hand side of the equation and using the orthogonality of $\phi^0_{in}(\boldsymbol{k})$ and replacing n and n',

$$(E^0_{in} - E)C_{in} + \sum_{i\neq j}\sum_n C_{jn'}u_{injn'} = 0 \tag{2.4.13}$$

where,

$$u_{injn'} = \sum_{\boldsymbol{k}\in\Omega_i}\sum_{\boldsymbol{k}'\in\Omega_j} \phi^0_{in}(\boldsymbol{k})U_{ij}(\boldsymbol{k},\boldsymbol{k}')\phi_{jn'}(\boldsymbol{k}') \tag{2.4.14}$$

secular determinant equation of (2.4.13) becomes,

$$\left|(E^0_{in} - E)\delta_{ij}\delta nn' + (1-\delta_{ij})u_{injn'}\right| = 0 \tag{2.4.15}$$

which leads to solution E_{in} and set of eigen vector $\{C_{in}\}$. Finally, here we have the complete representation of global impurity problem. If the transition matrix element $U(\boldsymbol{k},\boldsymbol{k}')$ is confined into the narrow region of Brillouin zone, and the secular determinant has small dimension according to the equation (2.4.5), This problem become easy to solve. But, once $U(\boldsymbol{k},\boldsymbol{k}')$ spread widely in the $\boldsymbol{k}$-space and include the intervalley scattering ($U_{ij} \neq 0$) in worse case, $|\phi\rangle$ need to consists of thousands of bloch

states and the secular determinant becomes too big to solve even with a help of the super computer.

2.4.2 Effective mass approximation

In the absence of intervalley scattering, equation which represent the impurity system simply becomes,

$$(E_{\boldsymbol{k}} - E)\phi_i^0(\boldsymbol{k}) + \int_{\boldsymbol{k}' \in \Omega_i} U_{ii}(\boldsymbol{k}, \boldsymbol{k}')\phi_i^0(\boldsymbol{k}') = 0 \qquad (2.4.16)$$

If we define $U_{ii}(\boldsymbol{k}, \boldsymbol{k}') = 0$ for $\boldsymbol{k} \notin \Omega_i$ or $\boldsymbol{k}' \notin \Omega_i$, we can expand integration region to whole $\boldsymbol{k}$–space.

Writing $U_{ii}(\boldsymbol{k}, \boldsymbol{k}')$ in more explicit manner, we get

$$\begin{aligned} U_{ii}(\boldsymbol{k}, \boldsymbol{k}') &= \langle \boldsymbol{k} | \, U(\boldsymbol{r}) \, | \boldsymbol{k}' \rangle \\ &= \int d\boldsymbol{r} \, \langle \boldsymbol{k} | \boldsymbol{r} \rangle \, U(\boldsymbol{r}) \, \langle \boldsymbol{r} | \boldsymbol{k}' \rangle \\ &= \int d\boldsymbol{r} \psi_{\boldsymbol{k}}^*(\boldsymbol{r}) U(\boldsymbol{r}) \psi_{\boldsymbol{k}'}(\boldsymbol{r}) \end{aligned} \qquad (2.4.17)$$

Because the Bloch function must be in the form of $\psi_{\boldsymbol{k}}(\boldsymbol{r}) = u_{\boldsymbol{k}}(\boldsymbol{r}) \exp(i\boldsymbol{k} \cdot \boldsymbol{r})$, $U_{ii}(\boldsymbol{k}, \boldsymbol{k}')$ becomes,

$$U_{ii}(\boldsymbol{k}, \boldsymbol{k}') = \int d\boldsymbol{r} \exp\left[-i(\boldsymbol{k} - \boldsymbol{k}') \cdot \boldsymbol{r}\right] U(\boldsymbol{r}) u_{\boldsymbol{k}}^*(\boldsymbol{r}) u_{\boldsymbol{k}'}(\boldsymbol{r}) \qquad (2.4.18)$$

As $u_{\boldsymbol{k}}(\boldsymbol{r})$ has the translation symmetry same to that of lattice, $u_{\boldsymbol{k}}^*(\boldsymbol{r}) u_{\boldsymbol{k}'}(\boldsymbol{r})$ can be expanded by reciprocal lattice vector.

$$u_{\boldsymbol{k}}^*(\boldsymbol{r}) u_{\boldsymbol{k}'}(\boldsymbol{r}) = \sum_{\boldsymbol{h}} C_{\boldsymbol{h}}(\boldsymbol{k}, \boldsymbol{k}') \exp(-i\boldsymbol{h} \cdot \boldsymbol{r}) \qquad (2.4.19)$$

Therefore, $U_{ii}(\boldsymbol{k}, \boldsymbol{k}')$ becomes

$$U_{ii}(\boldsymbol{k}, \boldsymbol{k}') = \sum_{\boldsymbol{h}} C_{\boldsymbol{h}}(\boldsymbol{k}, \boldsymbol{k}') \int d\boldsymbol{r} \exp[-i(\boldsymbol{k} - \boldsymbol{k}' + \boldsymbol{h}) \cdot \boldsymbol{r}] U(\boldsymbol{r})$$

$$= \sum_{\boldsymbol{h}} C_{\boldsymbol{h}}(\boldsymbol{k},\boldsymbol{k}')\widetilde{U}(\boldsymbol{k}-\boldsymbol{k}'+\boldsymbol{h}) \tag{2.4.20}$$

where $\widetilde{U}(\boldsymbol{k})$ is the Fourier transform of $U(\boldsymbol{r})$. If $U(\boldsymbol{r})$ varies very slowly compared to host lattice period, $\widetilde{U}(\boldsymbol{k})$ has significant value only for $|\boldsymbol{k}| \ll |\boldsymbol{h}|$. Now $\boldsymbol{k}$ and $\boldsymbol{k}'$ are confined in the region Ω_{ii}, $\boldsymbol{k}-\boldsymbol{k}'$ is much smaller than $\boldsymbol{h}$. So, $\boldsymbol{h}$ must be zero. Then $U_{ii}(\boldsymbol{k},\boldsymbol{k}')$ becomes

$$U_{ii}(\boldsymbol{k},\boldsymbol{k}') = C_0(\boldsymbol{k},\boldsymbol{k}')\widetilde{U}(\boldsymbol{k}-\boldsymbol{k}') \tag{2.4.21}$$

Moreover, if one approximate $C_0(\boldsymbol{k},\boldsymbol{k}')$ by $C_0(\boldsymbol{k}_0,\boldsymbol{k}_0)$, normalization condition $|u_{\boldsymbol{k}_0}|^2 = 1$ forces $C_0(\boldsymbol{k}_0,\boldsymbol{k}_0) = 1$ where $\boldsymbol{k}_0$ is the central critical point of Ω_i.

Expanding $E_{\boldsymbol{k}}$ around the critical point $\boldsymbol{k}_0$, the first term vanishes and $E_{\boldsymbol{k}}$ becomes

$$E_{\boldsymbol{k}} = E_{\boldsymbol{k}_0} + \frac{1}{2}\left\{(\boldsymbol{k}-\boldsymbol{k}_0)\cdot\nabla_{\boldsymbol{k}-\boldsymbol{k}_0}\right\}^2 E_{\boldsymbol{k}} + \cdots \tag{2.4.22}$$

Now we can define inverse effective math tensor.

$$\overleftrightarrow{\left(\frac{1}{m^*}\right)} = \frac{1}{\hbar}\left[\frac{\partial^2 E}{\partial k_i \partial k_j}\right]_{i,j=1,2,3} \tag{2.4.23}$$

If we choose the principal axis appropriately to diagonalize the effective mass tensor, (2.4.23) becomes,

$$E_{\boldsymbol{k}} = E_{\boldsymbol{k}_0} + \sum_{s=1}^{3}\frac{\hbar^2}{m_s^*}(k_s - k_{0s})^2 \tag{2.4.24}$$

Substituting this into (2.4.16), we get

$$\left\{\sum_{s=1}^{3}\frac{\hbar^2}{2m_s^*}(k_s-k_{0s})^2 - (E-E_{\boldsymbol{k}_0})\right\}\phi_i(\boldsymbol{k}) + \int d\boldsymbol{k}' U(\boldsymbol{k}-\boldsymbol{k}')\phi_i(\boldsymbol{k}') = 0 \tag{2.4.25}$$

Simply translating the origin,

$$\left\{\sum_{s=1}^{3}\frac{\hbar^2}{2m_s^*}k_s^2-(E-E_0)\right\}f_i(\boldsymbol{k})+\int d\boldsymbol{k}'U(\boldsymbol{k}-\boldsymbol{k}')f_i(\boldsymbol{k}')=0 \qquad (2.4.26)$$

where $f_i(\boldsymbol{k})=\phi_i(\boldsymbol{k}+\boldsymbol{k}_0)$.

Usual Fourier transform technic translate this into $\boldsymbol{r}$-representation. The result is,

$$\left\{\sum_{s=1}^{3}\left[-\frac{\hbar^2}{2m_s^*}\frac{\partial^2}{\partial x_s^2}\right]-(E-E_{0i})\right\}F_i(\boldsymbol{r})+U(\boldsymbol{r})F_i(\boldsymbol{r})=0 \qquad (2.4.27)$$

$$\left\{\sum_{s=1}^{3}\left[-\frac{\hbar^2}{2m_s^*}\frac{\partial^2}{\partial x_s^2}\right]+U(\boldsymbol{r})\right\}F_i(\boldsymbol{r})=(E-E_{0i})F_i(\boldsymbol{r}) \qquad (2.4.28)$$

This is referred to as the effective mass equation. In the Fourier transformation procedure, the following formula is used.

$$\int dk\exp(ikx)k^n f(k)=(-i)^n\frac{d^n}{dx^n}F(x) \qquad (2.4.29)$$

$$\int dk\exp(ikx)\int dt f(k-t)g(t)=F(x)G(x) \qquad (2.4.30)$$

where $F(x)$ and $G(x)$ are the Fourier transform of $f(k)$ and $g(k)$ respectively.

The wave function is of the form,

$$\begin{aligned}\phi(\boldsymbol{r}) &= \int d\boldsymbol{k}\psi_{\boldsymbol{k}}(\boldsymbol{r})\phi(\boldsymbol{k})\\ &\simeq \int d\boldsymbol{k}u_{\boldsymbol{k}_0}\exp(i\boldsymbol{k}\cdot\boldsymbol{r})f_i(\boldsymbol{k}-\boldsymbol{k}_0)\\ &= u_{\boldsymbol{k}_0}(\boldsymbol{r})\exp(i\boldsymbol{k}_0\cdot\boldsymbol{r})\int d\boldsymbol{k}f_i(\boldsymbol{k}-\boldsymbol{k}_0)\exp[i(\boldsymbol{k}-\boldsymbol{k}_0)\cdot\boldsymbol{r}]\\ &= \psi_{\boldsymbol{k}_0}(\boldsymbol{r})F_i(\boldsymbol{r}) \qquad (2.4.31)\end{aligned}$$

Effective mass approximation neglects the following points.

- Non parabolicity of band structure which emerges from the higher order in the expansion of energy around critical point (2.4.22)

- $\boldsymbol{h} \neq 0$ term in the expansion of $U_{ii}(\boldsymbol{k}, \boldsymbol{k}')$.
- Effect of intervalley scattering or scattering into higher excited states (U_{ij}).

And therefore the effective mass approach to the deep impurity problem will start from the procedure which extend above points.

2.4.3 Scattering state in crystal

Scattering state of impurity is expressed by the Lipmann-Schwinger equation with the incident Bloch function. In the Bloch representation, it is

$$\phi(\boldsymbol{k}) = \delta(\boldsymbol{k} - \boldsymbol{k}') - \frac{\int d\boldsymbol{k}'' U(\boldsymbol{k}, \boldsymbol{k}'')\phi(\boldsymbol{k}'')}{\epsilon_{\boldsymbol{k}} - \epsilon - i\eta} \tag{2.4.32}$$

$$\begin{aligned} |\phi\rangle &= \int d\boldsymbol{k} \, |\boldsymbol{k}\rangle \, \phi(\boldsymbol{k}) \\ &= \int d\boldsymbol{k} \, |\boldsymbol{k}\rangle \left[\delta(\boldsymbol{k} - \boldsymbol{k}') - \frac{\int d\boldsymbol{k}'' \, \langle \boldsymbol{k}| \, U(\boldsymbol{r}) \, |\boldsymbol{k}''\rangle \, \langle \boldsymbol{k}''|\phi\rangle}{\epsilon_{\boldsymbol{k}} - \epsilon - i\eta} \right] \\ &= |\boldsymbol{k}'\rangle - \int d\boldsymbol{k} \frac{|\boldsymbol{k}\rangle \, \langle \boldsymbol{k}|}{\epsilon_{\boldsymbol{k}} - \epsilon - i\eta} U(\boldsymbol{r}) \, |\phi\rangle \\ &= |\boldsymbol{k}'\rangle - G_0(\epsilon) U(\boldsymbol{r}) \, |\phi\rangle \end{aligned} \tag{2.4.33}$$

Multiplying $\langle \boldsymbol{r}|$ from the left hand side and using $\int d\boldsymbol{r}' \, |\boldsymbol{r}'\rangle \, \langle \boldsymbol{r}'| = 1$,

$$\begin{aligned} \phi(\boldsymbol{r}) &= \langle \boldsymbol{r}|\phi\rangle \\ &= \langle \boldsymbol{r}|\boldsymbol{k}'\rangle - \int d\boldsymbol{r}' \int d\boldsymbol{k} \frac{\langle \boldsymbol{r}|\boldsymbol{k}\rangle \, \langle \boldsymbol{k}|\boldsymbol{r}\rangle}{\epsilon_{\boldsymbol{k}} - \epsilon - i\eta} U(\boldsymbol{r}) \, \langle \boldsymbol{r}'|\phi\rangle \\ &= \Psi^*_{\boldsymbol{k}'}(\boldsymbol{r}) - \int d\boldsymbol{r}' G_0(\boldsymbol{r}, \boldsymbol{r}') U(\boldsymbol{r}) \phi(\boldsymbol{r}') \end{aligned} \tag{2.4.34}$$

where

$$G_0(\boldsymbol{r}, \boldsymbol{r}') = \int d\boldsymbol{k} \frac{\Psi^*_{\boldsymbol{k}}(\boldsymbol{r}) \Psi_{\boldsymbol{k}}(\boldsymbol{r})}{\epsilon_{\boldsymbol{k}} - \epsilon - i\eta} \tag{2.4.35}$$

This is the Lippman-Schwinger equation in $\boldsymbol{r}$-representation for the scattering problem. If we omit the incident Bloch function $\Psi^*_{\boldsymbol{k}'}(\boldsymbol{r})$, this is equivalent to the equation for the bound state (2.4.5).

2.5 Transition metals in silicon

2.5.1 Localized (3d) states in the crystal field

For simplicity, we treat $(3d)^1$ case where many body effect is cannot be found. If (3d)-atom exists in the absence of crystal field, the system Hamiltonian has the full rotational group symmetry and the electron wave function with an angular momentum l is the basis of corresponding irreducible representation $D^{(l)}$ and which has $(2l+1)$-folded degeneracy. But, if one put the (3d)-atom into the crystal field, symmetry of the system Hamiltonian will be reduced to that of crystal field. If the group of symmetry operation that conserves the crystal field Hamiltonian is expressed by $\mathcal{G}$, $(2l+1)$ folded states are separated into the levels which correspond to the irreducible representation of $\mathcal{G}$. This is equivalent to reducing $D^{(l)}$ into the irreducible representation of $\mathcal{G}$ ($\Gamma_\alpha, \Gamma_\beta, \cdots$), which is expressed by,

$$D^{(l)} \downarrow \mathcal{G} = \Gamma_\alpha + \Gamma_\beta + \cdots \tag{2.5.1}$$

Here we treat the case of interstitial Mn in Si for instance which we now mostly interested in. In crystal Si, it is said that Mn favors the interstitial position and surrounding Si atoms are tetrahedraly configured around Mn. Therefore d-electron of Mn suffers the crystal field of T_d-symmetry and its irreducible representation can be reduced using the character table of T_d,

that is,

$$D^{(2)} \downarrow T_d = T_2 + E \tag{2.5.2}$$

If the crystal field is strong enough to neglect the many body effect, electrons start occupying from the lower energy level of the two representation of (2.5.2). In this case, total spin becomes minimum because the electrons with an up-spin and with a down-spin occupy the same level. When the crystal field is weak and the coulomb interaction among the d-electrons is relatively strong, electrons tend to satisfy Fund's rule and arrange their spins and as a result, the total spin is enhanced. In the case of transition metal in Si, the total spin is said to be generally lowered because of the covalent nature and the strong crystal field [14, 15, 16].

2.6 Scattering of electron by deep level center

2.6.1 Quantum well scattering and zero energy resonance

Schrödinger equation for scattering problem is

$$\mathcal{H}\Phi_k^{(+)}(r) = E_k\Phi_k^{(+)} \tag{2.6.1}$$

$$\mathcal{H} = -\frac{\hbar^2}{2m}\nabla^2 + V(r) \tag{2.6.2}$$

Expanding $\Phi_k^{(+)}$ with spherical function,

$$\Phi_k^{(+)} = \sum_{l=0}^{\infty}\sum_{m=-l}^{l} C_{lm}R_l^{(+)}(r)Y_{lm}(\theta,\phi) \tag{2.6.3}$$

and substituting this into (2.6.1), we get

$$-\frac{\hbar^2}{2m}\left[\frac{1}{r^2}\frac{d}{dr}\left(r^2\frac{d}{dr}\right) - \frac{l(l+1)}{r^2}\right]R_l^{(+)}(r) + V(r)R_l^{(+)}(r) = E_kR_l^{(+)}(r) \tag{2.6.4}$$

$$\left[\frac{d^2}{dr^2} + k^2 - \frac{l(l+1)}{r^2} - U(r)\right] u_l(r) = 0 \tag{2.6.5}$$

where $u_l(r) = rR_l^{(+)}(r)$, $E_k = \frac{\hbar^2 k^2}{2m}$ and $V = \frac{\hbar^2}{2m}U$. Here we assume that the potential is the square well with the radius a and the depth V_0. Because u_l must smoothly smoothly at the surface of the well even though the potential is discontinuous, the following equations should hold.

$$u_l^{in}(a) = u_l^{out}(a), \qquad \left.\frac{du_l^{in}}{dr}\right|_{r=a} = \left.\frac{du_l^{out}}{dr}\right|_{r=a} \tag{2.6.6}$$

Therefore,

$$R_l^{(+)in}(a) = R_l^{(+)out}(a), \qquad \left.\frac{dR_l^{(+)in}}{dr}\right|_{r=a} = \left.\frac{dR_l^{(+)out}}{dr}\right|_{r=a} \tag{2.6.7}$$

This leads to the continuous condition of logarithmic derivative,

$$\left[\frac{1}{R_l^{(+)in}}\frac{dR_l^{(+)in}}{dr}\right]_{r=a} = \left[\frac{1}{R_l^{(+)out}}\frac{dR_l^{(+)out}}{dr}\right]_{r=a} \tag{2.6.8}$$

If we define f_l^{in} as

$$f_l^{in} \equiv \frac{1}{k}\left[\frac{1}{R_l^{(+)in}}\frac{dR_l^{(+)in}}{dr}\right]_{r=a} \tag{2.6.9}$$

and substituting into equation (2.6.8), we get

$$kf_l^{in} = \left[\frac{1}{R_l^{(+)out}}\frac{dR_l^{(+)out}}{dr}\right]_{r=a} \tag{2.6.10}$$

At the outer side of the well, the potential is zero and the equation (2.6.4) yields the solution,

$$R_l^{(+)out}(r) \propto \eta_l h_l^{(1)}(kr) + h_l^{(2)}(kr) \tag{2.6.11}$$

where $h_l^{(1)}(kr)$ and $h_l^{(2)}(kr)$ are the Hankel function of the first and the second kind, and $\eta_l = \exp(2i\delta_l)$ where δ_l is the phase shift for the l-th

partial wave. Substituting (2.6.11) into (2.6.10),

$$f_l^{in} = \frac{\eta_l h_l^{(1)\prime}(ka) + h_l^{(2)\prime}(ka)}{\eta_l h_l^{(1)}(ka) + h_l^{(2)}(ka)} \tag{2.6.12}$$

Solving this for η_l, we get

$$\eta_l = -\frac{h_l^{(2)}(ka) f_l^{in} - h_l^{(2)\prime}(ka)}{h_l^{(1)}(ka) f_l^{in} - h_l^{(1)\prime}(ka)} \tag{2.6.13}$$

We can get solution $\eta_l^{(c)}$ for the hard core potential by extrapolating $V_0 \to \infty$, which corresponds to $R_l^{in} = 0$, and $f_l^{in} = \infty$, and

$$\eta_l^{(c)} = -\frac{h_l^{(2)}(ka)}{h_l^{(1)}(ka)} \tag{2.6.14}$$

Relation $\eta_l = \exp(2i\delta_l)$ yields

$$\tan \delta_l = \frac{1}{i} \frac{\eta_l - \eta_l^*}{\eta_l + \eta_l^* + 2} \tag{2.6.15}$$

Therefore, we can determine the phase shift for the l-th partial wave concerned with the hard core scattering.

$$\tan \delta_l^{(c)} = \frac{j_l(ka)}{n_l(ka)} \tag{2.6.16}$$

For small ka, $j_l(ka)$ and $\eta_l(ka)$ can be approximated by

$$j_l(ka) \sim \frac{(ka)^l}{(2l+1)!!} \tag{2.6.17}$$

$$n_l(ka) \sim \frac{(2l-1)!!}{(ka)^{l+1}} \tag{2.6.18}$$

and then the phase shift becomes

$$\tan \delta_l^{(c)} = -\frac{(ka)^{2l+1}}{(2l+1)!!(2l-1)!!} \tag{2.6.19}$$

This decreases rapidly with l. For s-wave,

$$\tan \delta_0^{(c)} = -ka \tag{2.6.20}$$

Therefore the total cross section for s-wave is

$$\sigma^{(c)} = \frac{4\pi}{k^2}\sin^2\delta_0^{(c)} \sim 4\pi a^2 \tag{2.6.21}$$

This yields the inverse relaxation time of

$$\frac{1}{\langle\tau\rangle} = \frac{3\sqrt{2}N_I\pi^{\frac{3}{2}}a^2}{m^{*2}}(k_BT)^{\frac{1}{2}} \tag{2.6.22}$$

This shows $T^{\frac{1}{2}}$ dependence on temperature according to the variation of the mean thermal velocity of carriers.

Using $\eta_l^{(c)}$, general representation of η becomes,

$$\eta_l = \eta_l^{(c)}\frac{f_l^{in} - r_l(kar) + is_l(ka)}{f_l^{in} - r_l(ka) - is_-(ka)} \tag{2.6.23}$$

$$= \eta_l^{(c)}\left[1 + \frac{2is_l(ka)}{f_l^{in} - r_l(ka) - is_l(ka)}\right] \tag{2.6.24}$$

where definitions,

$$\frac{h_l^{(1)\prime}(ka)}{h_l^{(1)}(ka)} \equiv r_l(ka) + is_l(ka) \tag{2.6.25}$$

$$\frac{h_l^{(2)\prime}(ka)}{h_l^{(2)}(ka)} \equiv r_l(ka) - is_l(ka) \tag{2.6.26}$$

are used.

For the scattering of s-wave ($l = 0$), the equation for $u_l^{in}(r)$ becomes

$$\left[\frac{d}{dr^2} + (k^2 + U_0)\right]u_0^{in}(r) = 0 \tag{2.6.27}$$

Because $R_l^{(+)}$ must have finite value at the origin, the condition $u_0^{in}(0) = 0$ should be satisfied. This restriction leads to the solution of the form

$$u_0^{in}(r) = A\sin\kappa r, \qquad (\kappa = \sqrt{k^2 + U_0}) \tag{2.6.28}$$

therefore, $R_0^{(+)}$ becomes

$$R_0^{(+)}(r) = \frac{u_0^{in}(r)}{r} = A\frac{\sin \kappa r}{r} \tag{2.6.29}$$

and

$$f_0^{in} = \frac{1}{k}\left[\frac{1}{R_0^{(+)in}}\frac{dR_0^{(+)in}}{dr}\right]_{r=a} = \frac{1}{ka}\left[\kappa a \cot \kappa a - 1\right] \tag{2.6.30}$$

Here we define

$$F_0(ka) \equiv kaf_0^{in} - 1 = \kappa a \cot \kappa a \tag{2.6.31}$$

For s-wave and small ka, $\delta^{(c)} = -ka$, $r_0(ka) = -\frac{1}{ka}$ and $s_0(ka) = 1$ are satisfied. Then (2.6.24) becomes

$$\eta_0 = \exp(-2ika)\frac{F_0(ka) + ika}{F_0(ka) - ika} \tag{2.6.32}$$

By making use of the approximation $\exp(-2ika) \simeq 1 - 2ika$,

$$|1 - \eta_0|^2 \simeq 4(ka)^2\frac{(ka)^2 + [F_0(ka) - 1]^2}{(ka)^2 + [F_0(ka)]^2} \tag{2.6.33}$$

For small ka, we can approximate $F_0(ka)$ by $F_0(0)$ when $F_0(0)$ has a finite value. Then the total cross section becomes

$$\sigma = \frac{\pi}{k^2}|1 - \eta_0|^2 \simeq 4\pi a^2\left[1 - \frac{1}{F_0(0)}\right]^2 \tag{2.6.34}$$

This cross section vanishes when $F_0(0)$ approaches to unity. It is referred to as Ramsauer-Townsend effect.

When $F_0(0) = 0$, we must expand $F_0(ka)$ with $(ka)^2$, and

$$\begin{aligned} F_0(ka) &= F_0(0) + F_0^{(1)}(0)(ka)^2 + \cdots \\ &\simeq F_0^{(1)}(0)(ka)^2 \end{aligned} \tag{2.6.35}$$

where

$$F_0^{(1)} = \frac{dF_0(ka)}{d(ka)^2} \tag{2.6.36}$$

then (2.6.33) becomes

$$|1-\eta_0|^2 \simeq 4(ka)^2 \frac{(ka)^2 + [F_0^{(1)}(ka)^2 - 1]^2}{(ka)^2 + [F_0^{(1)}(0)(ka)^2]^2} \tag{2.6.37}$$

When ka approaches to zero, equation (2.6.37) approaches to 4, that is, $\eta_0 \to -1$ and $\delta_0 \to \frac{\pi}{2}$ which leads the total cross section

$$\sigma = \frac{\pi}{k^2}|1-\eta_0|^2 = \frac{4\pi}{k^2} \to \infty \tag{2.6.38}$$

This is referred to as zero energy resonance.

The wave function of the resonant state inside the well is also expressed by (2.6.28). But it is not the perfect bound state and the wave function oozes out of the well. If we assume this oozing as spherical wave of the form $u_0^{out}(r) = B\exp(ikr)$, the resonant state is constructed by connecting u_0^{in} and u_0^{out} smoothly. The boundary condition is,

$$\left[\frac{1}{u_0^{in}}\frac{du_0^{in}}{dr}\right]_{r=a} = \left[\frac{1}{u_0^{out}}\frac{du_0^{out}}{dr}\right]_{r=a} \tag{2.6.39}$$

The right hand side is identical to ik. Multiplying a by the both side of (2.6.39), the left hand side becomes $F_0(ka)$ and (2.6.39) gives

$$F_0(ka) = a\sqrt{k^2+U_0}\cot a\sqrt{k^2+U_0} = ika \tag{2.6.40}$$

We can get k and $\epsilon = \hbar^2k^2/2m$ for the resonant state by solving this equation. In the case that $k=0$, this leads to the zero energy resonance.

In order to solve (2.6.40), we should firstly get the zero point of $F_0(ka)$, i.e.,

$$a\sqrt{k^2+U_0}\cot a\sqrt{k^2+U_0} = 0 \tag{2.6.41}$$

Then solution is

$$k^2 = \left[\frac{\pi}{2a}(2n+1)\right]^2 - U_0 \tag{2.6.42}$$

and

$$E_s = \frac{\hbar^2 k^2}{2m} = \frac{\hbar^2 \pi^2}{2ma^2}(n+\frac{1}{2})^2 - \frac{\hbar^2 U_0}{2m} = \frac{\hbar^2 \pi^2}{2ma^2}(n+\frac{1}{2})^2 - V_0 \quad (2.6.43)$$

Expanding $F_0(E) = F_0(ka)$ around E_s,

$$F_0(ka) = F_0(E_s) + F_0^{(1)}(E_s)(E-E_s) + \frac{1}{2}F_0^{(1)}(E_s)(E-E_s)^2 + \cdots \simeq F_0^{(1)}(E_s)(E-E_s) \quad (2.6.44)$$

Then (2.6.40) becomes to

$$F_0^{(1)}(E_s)(E-E_s) = ika \quad (2.6.45)$$

Therefore the solution of (2.6.40) is approximated by

$$E = E_s + \frac{ika}{F_0^{(1)}(E_s)} = E_s - \frac{i}{2}\Gamma_s \quad (2.6.46)$$

where

$$\Gamma_s = -\frac{2ka}{F_0^{(1)}(E_s)} \quad (2.6.47)$$

Now we have the energy for the resonant state. Substituting (2.6.47) into (2.6.44), we have

$$F_0(E) = -\frac{2ka}{\Gamma_s}(E-E_s) \quad (2.6.48)$$

The total cross section is,

$$\sigma = \frac{\pi}{k^2}|1-\eta_0|^2 = \frac{\pi}{k^2}\left|1-\exp(-2ika)\frac{F_0(ka)+ika}{F_0(ka)-ika}\right|^2 = \frac{\pi}{k^2}\left|1-\exp(-2ika)\frac{2ika}{F_0(ka)-ika}\right|^2 = \frac{\pi}{k^2}\left|\frac{-i\Gamma_s}{(E-E_s)+\frac{i}{2}\Gamma_s}+1-\exp(-2ika)\right|^2 \quad (2.6.49)$$

The first term shows the resonant scattering and the second shows the hard core scattering. If we neglect the hard core part, total cross section becomes

$$\sigma = \frac{\pi}{k_s^2} \frac{\Gamma_s^2}{(E_k - E_s)^2 + \left(\frac{\Gamma_s}{2}\right)^2} \tag{2.6.50}$$

The resonant state appears dependent on the shape of potential. In the solid, it also depends on the band structure and in general it easily appears than in vacuum (see section 2.4.1). The simple calculation for the resonant scattering is presented in Fig.33 which is derived by taking the thermal average of relaxation time obtained using (2.6.50) It is noticed from the figure that the temperature dependence of inverse relaxation time is approximately $T^{\frac{1}{2}}$

2.6.2 Spin scattering

The interaction of the localized spin with the spin of conduction electron is expressed by the s-d interaction model, i.e.,

$$\mathcal{H} = -2Jv\delta(\boldsymbol{r})\boldsymbol{s}\cdot\boldsymbol{S} \tag{2.6.51}$$

$$= -\frac{2J}{N}\sum_{\boldsymbol{q}} \exp(-i\boldsymbol{q}\cdot\boldsymbol{r})\boldsymbol{s}\cdot\boldsymbol{S} \tag{2.6.52}$$

where $\boldsymbol{s}$ is the spin of the conduction electron, $\boldsymbol{S}$ spin of the localized magnetic impurity, v the volume per a lattice point and J is the exchange integral. J is assumed to be less affected by $\boldsymbol{k}$ of electrons. Here we write the transition matrix using T-operator, $T(\epsilon_k + i\eta_k)$,

$$T(\boldsymbol{k}', \sigma', M'; \boldsymbol{k}, \sigma, M) \equiv \left\langle \boldsymbol{k}', \sigma', M' \middle| T(\epsilon_k + i\eta_k) \middle| \boldsymbol{k}, \sigma, M \right\rangle \tag{2.6.53}$$

where σ is z component of s and M is that of S. The scattering relaxation time τ of the electron is expressed by the golden rule.

$$\frac{1}{\tau(\boldsymbol{k})} = \sum_{\boldsymbol{k}'} \sum_{\sigma,\sigma'} \sum_{M,M'} \frac{2\pi}{\hbar} \left| T(\boldsymbol{k}', \sigma', M'; \boldsymbol{k}, \sigma, M) \right|^2 \delta(\epsilon_{\boldsymbol{k}} - \epsilon_{\boldsymbol{k}'}) \tag{2.6.54}$$

Because J is less affected by $\boldsymbol{k}$, T do not depend on $\boldsymbol{k}$ and $\tau(\boldsymbol{k})$ can be regarded as the function of $\epsilon_{\boldsymbol{k}}$. Then (2.6.54) becomes

$$\begin{aligned} \frac{1}{\tau(\epsilon_{\boldsymbol{k}})} = \frac{2\pi}{\hbar} \rho(\epsilon_{\boldsymbol{k}}) \sum_{M} w_M \{ & \quad |T(\epsilon_{\boldsymbol{k}'}, \uparrow, M; \epsilon_{\boldsymbol{k}}, \uparrow, M)|^2_{\epsilon_{\boldsymbol{k}}=\epsilon_{\boldsymbol{k}'}} \\ & + |T(\epsilon_{\boldsymbol{k}'}, \downarrow, M+1; \epsilon_{\boldsymbol{k}}, \uparrow, M)|^2_{\epsilon_{\boldsymbol{k}}=\epsilon_{\boldsymbol{k}'}} \} \end{aligned} \tag{2.6.55}$$

where the inelastic scattering is neglected and only the elastic process is considered. $\rho(\epsilon_{\boldsymbol{k}})$ is the density of state at energy $\epsilon_{\boldsymbol{k}}$, w_M the probability in the case that z component of S is M. The term other than these two are omitted because they do not preserve the total spin.

For the s-d exchange interaction, T-operator for the one electron scattering can be written as,

$$T(\epsilon + i\eta) = t(\epsilon + i\eta) + \tau(\epsilon + i\eta)\boldsymbol{\sigma} \cdot \boldsymbol{S} \tag{2.6.56}$$

where $t(\epsilon + i\eta)$ is the part which do not contain spin flip, $\tau(\epsilon + i\eta)$ that with spin flip. Making use of the relation, $\boldsymbol{\sigma} \cdot \boldsymbol{S} = \frac{1}{2}(\sigma_+ S_- + \sigma_- S_+) + \sigma_z S_z$, we can calculate the matrix element, i.e.,

$$T(\epsilon_{\boldsymbol{k}}, \uparrow, M; \epsilon_{\boldsymbol{k}}, \uparrow, M) = t(\epsilon_{\boldsymbol{k}}) + \tau(\epsilon_{\boldsymbol{k}}) M \tag{2.6.57}$$

$$T(\epsilon_{\boldsymbol{k}}, \downarrow, M+1; \epsilon_{\boldsymbol{k}}, \uparrow, M) = \tau(\epsilon_{\boldsymbol{k}}) \sqrt{(S-M)(S+M+1)} \tag{2.6.58}$$

where $i\eta(\epsilon_{\boldsymbol{k}})$ is omitted. We can calculate the inverse relaxation time by substituting these into (2.6.55). When the magnetic field is not applied,

linear term on M is canceled out and we can get,

$$\frac{1}{\tau(\epsilon_k)} = \frac{2\pi}{\hbar}\rho(\epsilon_k)\left\{|t(\epsilon_k)|^2 + |\tau(\epsilon_k)|^2 S(S+1)\right\} \tag{2.6.59}$$

In the first Born approximation, $T(\epsilon + i\eta)\,|\boldsymbol{k}\rangle = V\,|\boldsymbol{k}\rangle$ can be assumed, then

$$t(\epsilon_k) = 0, \qquad \tau(\epsilon_k) = -\frac{J}{2N} \tag{2.6.60}$$

Therefore the inverse relaxation time is

$$\frac{1}{\tau(\epsilon_k)} = \frac{2\pi}{\hbar}\rho(\epsilon_k)\left\{\left(\frac{J}{2N}\right)^2 S(S+1)\right\} \tag{2.6.61}$$

Using the density of states of the conduction band,

$$\rho(\epsilon_k) = \frac{(2m^*)^{3/2}}{2\pi^2\hbar^3}(\epsilon_k - \epsilon_c)^{\frac{1}{2}} \tag{2.6.62}$$

and making thermal average of (2.2.8), we get the final result for the relaxation time.

$$\frac{1}{\langle\tau\rangle} = \frac{3m^{*\frac{3}{2}}}{\sqrt{\pi}\hbar^4}\left\{\left(\frac{J}{2N}\right)^2 S(S+1)\right\}(kT)^{\frac{1}{2}} \tag{2.6.63}$$

Note that this has $T^{\frac{1}{2}}$ dependence on temperature.

3 Experimental Procedures

3.1 Sample preparation

Samples are prepared by doping of transition metal impurity into FZ pure Si single crystal with resistivity of $\sim 3000\Omega - cm$. Residual shallow impurity is boron of which concentration is less than $10^{12} cm^{-3}$. Doping of transition metals was carried out by evaporation onto Si surface and diffusing at high temperature of $\sim 1100\ ^{\circ}C$. Firstly, host Si wafer with (100) surface was prepared from 1 inch ingot. Before evaporation of metal, the sample wafer was ultrasonically rinsed out by trichloroethylene and etched by HF to remove the oxide layer. Transition metal was then evaporated from the alumina coated tungsten basket or bare tungsten boat onto silicon surface under the vacuum of $\sim 10^{-5}$ Torr. Deposition was continued until the closely configured glass plate becomes perfectly opaque. The evaporation chamber is not necessarily kept at a high vacuum, but the main components of residual gases are expected to be oxygen and water vapor which have much less diffusivity in Si crystal compared to transition metals and they should have less effect in diffusion process and measurements. In the first place, we evaluate the diffusion depth based on the following simple calculation.

Diffusion equation is,

$$\frac{\partial n(\boldsymbol{r},t)}{\partial t} = -div(\boldsymbol{a}n(\boldsymbol{r},t)) + D\nabla^2 n(\boldsymbol{r},t) \qquad (3.1.1)$$

where $n(\boldsymbol{r},t)$ is the density of impurity, D the diffusion constant and $\boldsymbol{a}$ is the drift vector. For thermal diffusion, we assume $\boldsymbol{a}$ to be zero. Then in

one dimensional case, equation (3.1.1) becomes,

$$D\frac{\partial^2}{\partial x^2}n(x,t) = \frac{\partial}{\partial t}n(x,t) \tag{3.1.2}$$

Because the quantity of deposited metal onto surface was so large in comparison with the maximum solubility of transition metal in Si (usually of the order of 10^{16} cm^{-3} at 1100 °C), we can assume that the density of metal at Si surface is constant. A solution of equation (3.1.2) under such boundary condition is given by,

$$\begin{aligned} n(x,t) &= n_0\left[1-\mathrm{erf}\left(\frac{x}{2\sqrt{Dt}}\right)\right] \\ &\sim \frac{n_0}{\frac{x}{2}\sqrt{\pi Dt}}\exp\left[-\frac{x^2}{4Dt}\right] \end{aligned} \tag{3.1.3}$$

where $\mathrm{erf}(x)$ is the error function.

$$\mathrm{erf}(x) = \frac{2}{\sqrt{\pi}}\int_0^x \exp[-t^2]dt \tag{3.1.4}$$

In this case, the penetration depth of impurity can be regarded to be the order of $2\sqrt{Dt}$. Table 2 shows the diffusion constant of various element in

Metal	Temperature(C)	D(cm^2/s)	Reference
Mn	1038	$1.68 \sim 2.49 \times 10^{-6}$	Gilles [17]
Mn	854	$2.3 \sim 8.4 \times 10^{-7}$	Gilles [17]
Mn	700	$7 \times 10^{-8} \sim 5 \times 10^{-9}$	Gilles [17]
Fe	920	1.7×10^{-6}	Gilles [17]
Co	700	$2.4 \times 10^{-7} \sim 4 \times 10^{-11}$	Gilles [17]

Table 2: Diffusion Constant of various element in Si

Si crystal from which we can evaluate the time for impurity perfectly to diffuse to opposite side of wafer. For the case of Mn element, the diffusion constant is known as $D = 2 \times 10^{-6} cm^2/s$ at T=1100 $°C$. Assuming the thickness of the wafer is 1mm, the time for Mn to diffuse to the back surface is evaluated to be $\sim$ 20 minutes. In the case of substitutional shallow impurity such as B on the other hand, the diffusion constant is about $D \sim 10^{-13} cm^2/s$ at T=1100$°C$ [18] which is 10^{-7} times smaller than that for transition metals and it will take 4.2×10^8 minutes to reach to the back surface. In practice, samples are annealed for 8$\sim$24 hours at 1100°C considering the surface barrier to penetrate into Si bulk such as silicide formation and to obtain the uniform distribution of metal atom. For 24 hours annealing, substitutional shallow impurity will penetrate into Si for only 2 μm.

In the end of thermal diffusion, samples were dropped into glycerin and quickly quenched to avoid the precipitation of metal impurity onto surface. After quenching, sample surface was polished with emery paper to remove the surface metal layer, and etched by HF+NO_3(HF:NO_3=1:5) solution. Diffusion of metal was confirmed by two methods, namely, SIMS (Secondary Electron Mass Spectroscopy) and DLTS (Deep Level Transient Spectroscopy). Procedure of DLTS measurement will be described later. SIMS measurement was done by Matsushita Techno-Research Co. The result is shown in Fig. 1. It can be seen that Mn of $\sim 2 \times 10^{15} cm^{-3}$ has diffused uniformly except for near surface. Together with the Mn diffusion, we acknowledge the co-diffusion of Cu of $\sim 10^{16} cm^{-3}$. But it

will become clear in Section 4.2 that Cu is unimportant for the scattering of electrons. In addition, there can be seen the signals from Al and Na, but they are not exceeding the lower detectable limit for Al and Na that is about $3 \times 10^{14} cm^{-3}$ and $1 \times 10^{14} cm^{-3}$, respectively. Furthermore, it became clear in PL measurements that no shallow impurity such as Al did not diffuse into specimen so much as to affect the electron scattering and the fact supports our expectation.

3.2 Microwave Cyclotron Resonance

Figure 3 shows the experimental diagram of microwave cyclotron resonance. Prior to the measurements, a sample surface was washed by trichloroethylene ultrasonically and etched again by HF+HNO_3 solution for several seconds and set into the bottom of the wave guide with grease and then immersed into the liquid Helium. In the measurements, the sample was illuminated by Xe flash lamp through the glass lod to obtain free carriers. The pulse width of Xe flash lamp is the order of sub μs. In order to eliminate the high energy component which generates the hot carrier and make carrier density high at near surface because of its high absorption coefficient, and IR filter was emplayed. So, the light actually used to excite the sample is which include the energy components near band gap which has low absorption coefficient compared to higher energy. Sample were expected to be uniformly excited. The pulse rate was set to 20Hz which may not raise the sample temperature. Microwave is generated at the Klystron and guided into 8mm size wave guide through the

attenuator and divided at magic–T. One part is guided to sample direction and the other is guided to the opposite direction at where the phase shifter was settled. Finally the divided two wave were again mixed at the magic–T after the appropriate phase and amplitude matching operation and reached to the GaAs diode detector. As the detector output is nearly proportional to the square of the amplitude of electric field, We can obtain power absorption directly from the detector output. The signal was then put into two channel boxcar integrator equipped with two plug-in amplifier gated at an arbitrary time position. Output from the boxcar integrator was recorded using both of analog recorder and personal computer with digital voltmeter equipped with GP-IB interface. The signal was taken after the appropriate interval from the excitation to avoid the carrier–carrier scattering contribution to line width. Usual sample temperature was 4.2K cooled by liquid He. Temperature can be varied down to 1.5K by evacuating liquid He, and up to about 12K by thermally shielding by evacuating only around the sample and heating with manganine heater near the sample. Sample temperature was measured using both of closely settled carbon resistance and manometer (only under 4.2K). Magnetic field up to 6000 gauss was applied using an ordinary split magnet. Magnetic field direction was perpendicular to the (100) direction and choosed to separate the six-folded conduction band of Si into three two-folded ones as depicted in the inset of the figure 3.

3.3 Far Infrared Cyclotron Resonance

The experimental diagram of far–infrared (FIR) light cyclotron resonance was depicted in Fig. 4. Sample was attached on the bake plate with GE varnish and settled into the cryostat and immersed into the liquid helium. Far infrared laser was optically pumped by electric discharge excitation type CO_2 infrared laser and generate the 513 μm line. FIR light was guided to sample by about 10mmϕ light pipe. The light passed through the sample was detected by the appropriately biased InSb detector where the detection was realized using photothermal conduction mechanism. Sample was illuminated by Xe flash lamp to generate the free carrier in the similar way to microwave experiment. Minor difference is that in the FIR case the glass lod is slightly bent due to the existence of FIR light pipe which considerably lowered the excitation efficiency. Magnetic field was applied using superconducting magnet up to 5 Tesra. This time the magnet is in (100) direction which is perpendicular to the sample surface and pallarel to the FIR light propagation vector (Faraday configuration). The sample temperature was fixed to 4.2K all the time by immersing the cryostat into the liquid helium directly. The signal from the detector was put into two channel boxcar integrator also in the similar way to microwave experiment and recorded and treated in the personal computer.

3.4 Deep Level Transient Spectroscopy

DLTS measurement was firstly introduced by D.V.Lang [19] and until now, it is widely used to characterize the deep level traps in the semiconductor.

Wide properties of deep traps such as activation energy, concentration profile and capture cross-section can be obtained by this method. This method is based on the thermal emission properties of traps which is almost unique to each traps. So, DLTS can be the powerful method to distinguish the various traps in semiconductors. Here we present the brief description of the DLTS measurement process.

DLTS measurement is done by utilizing the transient change of the capacitance of the depletion layer of Schottky barrier or p-n junction. Here we assume the n-type semiconductor case where the current carrier is electrons and Schottky barrier is for electrons. Capacitance of Schottky barrier as a bias voltage is approximated by the formula,

$$C = \left(\frac{e\epsilon_s N_d}{2}\right)^{\frac{1}{2}} \left(V_{d0} + V_r - \frac{kT}{e}\right)^{-\frac{1}{2}} \tag{3.4.1}$$

where ϵ_s is the dielectric constant of the sample, N_d the shallow donor concentration, V_r is the reverse bias and V_{d0} is the diffusion voltage at zero bias. DLTS measurement is usually executed under the reverse bias condition where the most shallow impurities existing near surface are ionized and depletion layer is so wide and capacitance is rather small. When sufficiently long forward pulse voltage is applied to the junction, the shallow impurities are fully neutralized and the capacitance becomes large. At the same time, if there exist the deep electron traps, they are also filled. After the pulse voltage is finished to apply and initial reverse bias is recovered, shallow impurities are ionized again and depletion layer is also widen again. But the deep trap filled by the pulse bias takes rather much time to release electrons compared to shallow ones according to their large

activation energy, which prevent the concurrent recovering of capacitance and causes the time dependent capacitance change in the Schottky barrier. Such time dependence is related to the activation energy and capture cross-section of deep trap and expressed by

$$C(t,T) = C(0,T) - \Delta C_0 \exp\left[-e_n(T)t\right] \tag{3.4.2}$$

$$e_n(T) = N_c v_n \sigma_n \exp\left[-\frac{E_i}{kT}\right] \tag{3.4.3}$$

where N_c is the effective density of states of conduction band, v_n is the thermal velocity of electron and σ_n the electron capture cross section of impurity considered here. They are,

$$N_c = \left(\frac{2\pi m^* kT}{h^2}\right)^{\frac{3}{2}} \tag{3.4.4}$$

$$v_n = \left(\frac{3kT}{m_e^*}\right)^{\frac{1}{2}} \tag{3.4.5}$$

$$\sigma_n = \sigma_\infty \exp\left(-\frac{E_B}{kT}\right) \tag{3.4.6}$$

Substituting (3.4.4), (3.4.5) and (3.4.6) into (3.4.3), explicit temperature dependence of e_n can be obtained as,

$$e_n(T) = CT^2 \exp\left(-\frac{E_i + E_B}{kT}\right) \tag{3.4.7}$$

and

$$C = \frac{(2\pi k)^{\frac{3}{2}} m_e^* \sqrt{3}\sigma_\infty}{h^3} \tag{3.4.8}$$

Measuring capacitance at two different time t_1 and t_2 after the injection of a pulse, one can get,

$$\begin{aligned} S(T) &= C(t_2,T) - C(t_1,T) \\ &= \Delta C_0 \left\{\exp[-e_n(T)t_1] - \exp[-e_n(T)t_2]\right\} \end{aligned} \tag{3.4.9}$$

For temperature which maximize $S(T)$, it needs $\frac{dS(T)}{dT}|_{T_m} = 0$, we obtain the equation,

$$a \equiv \frac{\ln t_1 - \ln t_2}{t_1 - t_2} = e_n(T_m) \tag{3.4.10}$$

Notation a is referred to as rate window. By plotting T_m^2/a against $1/T_m$, one can get $E_i + E_B$ from its slope according to the relation (3.4.7). Here we must remind the capacitance of Schottky barrier is expressed by the equation (3.4.1). If there are considerable amount of deep electron traps, the same amount of charges of ionized shallow impurity are canceled out until the traps release their charges. It leads the modification of capacitance,

$$\Delta C_0 = -\frac{1}{2}(q\epsilon)^{\frac{1}{2}} N_s^{-\frac{1}{2}} \Delta N_s \left(V_{d_0} + V_r - \frac{kT}{q} \right)^{-\frac{1}{2}} \tag{3.4.11}$$

then,

$$\begin{aligned} \frac{\Delta C}{C} &= \frac{\Delta N_s}{2N_s} \\ N_d &= \Delta N_s = 2N_s \frac{\Delta C_0}{C} \end{aligned} \tag{3.4.12}$$

One can get N_s by measuring the capacitance - reverse voltage relation using (3.4.1). If we choose $10t_1$ for t_2, $S(T_m)$ simply becomes to $0.697\Delta C_0$ and the concentration of deep trap is,

$$N_d = 2.87 N_s \frac{S(T_m)}{C} \tag{3.4.13}$$

Experimental block diagram of DLTS is depicted in Fig. 5. The sample is settled into helium refrigerator unit and the sample temperature is stabilized by computer controlled temperature controller. Capacitance signal is get by digital capacitance meter which can get the whole time variation

of transient behavior of capacitance at one pulse. Pulsed reverse bias is applied to the sample by utilizing the trigger output from the capacitance meter which is once attenuated from 5V to one tenth of required voltage and amplified 10 times by pulse amplifier. Impedance matching was made by serially configured resistance. Temperature data from the temperature control unit and transient capacitance data from digital capacitance meter is obtained and treated by personal computer.

3.5 Electron Spin Resonance

Electron Spin Resonance measurements were examined at IPCR (Institute of Physical and Chemical Research) in cooperation with Dr. Katsumata and Dr. Hagiwara. Figure 6 shows the configuration diagram of our experimental equipment. The sample is settled at the end of a quartz rod and put into a microwave cavity. The frequency of microwave was 9.21 GHz and its power was usually 4mW. The usual modulation frequency was 100kHz and its amplitude in magnetic field was 5G. The sample temperature was controled by a heater coiled at the injector and changed from 4K to 300K.

For instance, we should handle the case of Mn in Si. Interstitial Mn can exist in Si with five possible charge state according to the published article [14, 15, 16] and four of five had been observed in ESR and DLTS measurements. They are $Mn^{-}(3d)^{8}$,$Mn^{0}(3d)^{7}$,$Mn^{+}(3d)^{6}$ and $Mn^{2+}(3d)^{5}$.

Effective spin Hamiltonians of the system of total (3d)–spin interacting

with external magnetic field and nuclear spin is,

$$\mathcal{H} = g\mu_B \boldsymbol{H} \cdot \boldsymbol{S} + \boldsymbol{I}\widetilde{A}\boldsymbol{S} \tag{3.5.1}$$

where $\boldsymbol{H}$ is the static magnetic field and $\boldsymbol{S}$ is the total spin of unfilled 3d–electron and $\boldsymbol{I}$ is nuclear spin and $\widetilde{A}$ is the hyperfine interaction constant. If we choose the axis to diagonalize $\widetilde{A}$ and apply the magnetic field $H = (0, 0, H_z)$, equation (3.5.1) becomes,

$$\begin{aligned} \mathcal{H} &= g\mu_B S_z H_z + A_z I_z S_z + A_x I_x S_x + A_y I_y S_y \\ &= g\mu_B S_z H_z + A_z I_z S_z + \frac{1}{4}(A_x + A_y)(I^+ S^- + I^- S^+) \\ &\quad + \frac{1}{4}(A_x - A_y)(I^+ S^+ + I^- S^-) \end{aligned} \tag{3.5.2}$$

Let us treat the case that Mn spin is $S = \frac{1}{2}$. For almost all Mn exists, nuclear spin is $I = \frac{5}{2}$, so the number of basis spin fu nction is $2 \times 6 = 12$. Diagonalizing (3.5.2) leads to the energy,

$$E_\pm = \pm\frac{g\mu_B H_z}{2} \pm \frac{mA_z}{2} \pm \frac{I(I+1) - m^2}{8g\mu_B H_z}(A_x^2 + A_y^2) - \frac{m}{4g\mu_B H_z} A_x A_y \tag{3.5.3}$$

where m is the nuclear spin quantum number ($I_z |m\rangle = m\hbar |m\rangle$) and an approximation $A \ll g\mu_B H_z$ is used.

If the H_z is small, S and I are not a good quantum number because of the relatively large mixing term. The states will be specified by F which is eigen value of $\boldsymbol{F} = \boldsymbol{I} + \boldsymbol{S}$. But, once H_z become larger so that we can neglect the last two term in (3.5.3), then energy becomes,

$$E_\pm \sim \pm\frac{g\mu_B H_0}{2} \pm \frac{mA_z}{2} \tag{3.5.4}$$

Energy diagram is depicted in Fig. 7. In zero magnetic field, Energy is separated in 7-fold states (F=3) and 5-fold sates (F=2). As magnetic

field is increased, the folded states become separated and quantum number I and S again become good number to specify states. Usual ESR measurement satisfies the condition for large magnetic field and magnetic transition occurs when the selection rule $\Delta S = \pm 1$ and $\Delta I = 0$ are satisfied. So, we can expect to observe six lines in the ESR measurement of Si:Mn.

3.6 Photoluminescence

Configuration diagram for photoluminescence measurement is depicted in Fig. 8. All measurements were done at helium temperature. Excitation light is Ar^+ laser (4880 Å line) which is filtered to cut the light with wave length above 6000 Å and below 4000 Å. PL light from the sample is focused by lens and filtered to cut the light with wavelength below 6500 Å in front of the monochromater which has 600 mm^{-1} grating and about $2m$ radius. The monochromated light is detected by Ge-PIN diode detector appropriately biased and cooled with liquid nitrogen. Signal from the detector is processed by Lock-in Amplifier and its output is stored into personal computer via digital voltmeter.

3.7 DC measurements

For Hall measurements, electrodes must be attached but we must not apply any annealing treatment because of high diffusivity of transition metals in Si crystal. Finally, for n-type Si, electrode was successfully made by evapolating Al onto Si surface and for p-type Si, that was realized by

rubbing In:Ga arroy. He refrigerator was used

4 Experimantal Results

4.1 DLTS measurements

We firstly made the DLTS measurements on Mn doped n-type CZ-Si to certify that aimed diffusion of Mn into Si host is achieved. Usual DLTS measurements require the certain amount of shallow impurities to supply free electron to fill up the deep level within the period the forward bias is applied. So, we must use rather highly doped Si instead of pure one we used in cyclotron resonance measurement. Table 3 shows the previously

Energy Level	Type	Assignment	Ref
$E_c - 0.12eV$	acceptor	interstitial	[20, 21]
$E_c - 0.27eV$	donor	Mn_4	[21]
$E_c - 0.41eV$	donor	interstitial	[20, 21]
$E_c - 0.51eV$		substitutional	[20]
$E_c - 0.54eV$	donor	Mn-B pair	[20]
$E_v + 0.32eV$	donor	interstitial	[20, 21]
$E_v + 0.39eV$	donor	substitutional	[22, 23]

Table 3: Previously observed DLTS signal for Si:Mn

obtained DLTS signal for Si:Mn. The typical DLTS signal we obtained is depicted in Fig. 9. The reverse bias is 5V, filling bias 0V, and rate window ratio $t_2/t_1 = 0$ for t_1 is 10 μs to 10 ms. The injection pulse width is 1ms. Making use of the standard rate window variation technic described in section 3.4, we can obtain for $E + E_i$, $E_c - 0.11eV$, $E_c - 0.20eV$ and

$E_c - 0.39eV$ from Arrhenius plot as shown in Fig. 10. The temperature dependence of capacitance is shown in figure 11 from which we can obtain the trap density was obtained from temperature dependence of capacitance by making use of the relation (3.4.13). The signal of $E_c - 0.39eV$ is close to the level position of interstitial Mn ($Mn_i^0 \rightarrow Mn_i^+$) shown in Table 3 and that of $E_c - 0.11eV$ is correspond to ($Mn_i^- \rightarrow Mn_i^0$). We have not succeeded in the assignment of $E_c - 0.20eV$ signal. The signal appears around this energy was attributed to Mn_4 cluster [21, 20] or a defect signal [24]. Mn_4 signal is reported to have energy level at about $E_c - 0.27eV$. The defect signal is reported to have signal at abour $E_c - 0.20eV$ and they obserbed it in only quenched sample, too. But, we have not observed any signal in only quenched sample.

DLTS measurement was also done using the back side surface of the same sample, and almost the same result was obtained and the fact shows uniform diffusion of Mn in host Si is achieved.

DLTS measurement for p-type Si doped with Mn in the same way did not succeed because of its high resistivity which is known as caused by the coupling of Mn and shallow acceptor (boron in this case). Mn-B pair is known to become donor with activation energy of $E_c - 0.54eV$. This pairing not only reduce the density of acceptor boron but also compensate it. The DLTS measurement for p-type Si:Mn requires the well controlled sample preparation. If we want to observe the DLTS signal in p-type Si:Mn, the sample with boron density higher than $10^{16}cm^{-3}$ will be required.

4.2 Cyclotron resonance

The data obtained and stored into personal computer system were fit numerically as superposition of several Lorentzian curves using the non-linear minimum square technic referred to as the Gauss-Newton method described in appendix A and separated into each constituting Lorentzian curve to obtain accurate line width. The typical result of fitting is depicted in Fig. 12. The rather broad peak at around B=1.9kG named as HCR1 is light hole resonance and HCR2 is heavy hole resonance. Because Si has the six fold degeneracy in conduction band and have three equivalent pairs if ellipsoidal iso-energy surface is assumed, three resonance for electron can be obtained. Magnetic field was applied to separate these peaks. We decided to evaluate the relaxation time of electron using ECR1 which has cyclotron effective mass $m^*/m_0 = 0.208$ obtained from the actual resonance peak using the relation (2.1.28).

Figure 13 shows the time resolved microwave absorption for stepping magnetic field drawn in three dimensional plot from which we obtain the time resolved cyclotron resonance curves as shown in Fig. 14. We also get the time resolved inverse relaxation time as depicted in Fig. 15. The initial enhancement of line width is due to momentum relaxation of electron caused by carrier-carrier scattering and its decaying feature depends on the carrier recombination process. The evaluation of line width was done at time position where the broadening caused by carrier-carrier scattering become negligible. The final line width to be analysed was obtained by averaging the several number of resonance curve obtained in the way

described above and from which we can get the electron inverse relaxation time according to (2.1.29). Figure 16 shows the typical cycrotron resonance line of FZ pure Si and that doped with Mn measured at liquid He temperature. One can see the remarkable enhancement of line width in Si:Mn sample compared to pure Si. Let us concentrate into the peak named ECR1 as mentioned above. Figure 17 shows the obtained temperature dependence of inverse relaxation time of FZ-Si doped with various transition metal obtained from ECR1 peak. Straight line shows the acoustic phonon contribution which has $T^{\frac{3}{2}}$ dependence to temperature as described in section 2.3.1. Quenched Si has slightly broader line width compared to pure host. We did not yet identified the origin of this broadening, but it should be attributed to defect center or some deep impurities entered at the annealing process, but not to shallow impurity. The reason will become clear in the PL measurement where postannealing procedure decreases the Si defect which act as nonradiative recombination center. It can be seen that transition metal impurity other than Mn have line width almost same to quenched Si and do not significantly affect the relaxation time of electron. It is notable that only Mn doped Si exhibits extraordinary enhancement in inverse relaxation time among Si doped with the transition metal impurity. We have not yet certified the diffusion of these metal impurity other than Mn. There rest a little possibility that these metals have not diffused in Si sufficiently. We only expected the diffusion of these metal impurities by their diffusion constant in Si comparable to Mn. Figure 18 shows the inverse relaxation time for Si:Mn

and host Si where host Si contribution to line width which is expected to contain acoustic phonon scattering only was subtracted. The temperature dependence of $1/\tau$ obtained by least square method is about $T^{0.41}$. Next, we show the result of annealing effect on signal. Figure 19 shows the cyclotron resonance line of the sample which experienced various annealing treatment. The sample named "Slowly cooled Si:Mn" is that experienced no quenching process after the diffusion of Mn and naturally cooled with the furnace. It takes about a half day to be cooled down to room temperature. The sample named "Annealed Si:Mn" is a quenched one, but after quenching it was annealed at $500°C$ for about 4 hours and cooled slowly. "Quenched Si" is a non-doped one which experienced the same process to doped ones including quenching without Mn doping. We can see that Mn doped Si has the large line width but Slowly cooled Si:Mn has as large width as pure Si. And even in the quenched Si:Mn, rather low temperature annealing ($500°C$) made line width narrower to the size as narrow as that of quenched Si. This result shows the precipitation of Mn atom occurs even at $500°C$ because of their high mobility and very low solubility in Si and make it sure that the broadening of cyclotron resonance line width is caused by Mn doping.

4.3 ESR measurements

Typical ESR signal of Si:Mn obtained is depicted in Fig. 20. These signals were not seen in host Si and Quenched reference sample. The corresponding g-value calculated is $g = 3.375$. This signal is already attributed to

$Mn^0(S = 1/2)$ in the previous work as depicted in Table 4. The sample

state	configuration	spin	g	A
Mn^{2+}	$(3d)^5$	$\frac{5}{2}$	2.0066	-53.47
Mn^+	$(3d)^6$	1	3.01	73.8
Mn^+	$(3d)^6$	2	1.68	46.1
Mn^+	$(3d)^6$	3	1.34	
Mn^0	$(3d)^7$	$\frac{1}{2}$	3.362	92.5
Mn^0	$(3d)^7$	$\frac{3}{2}$	1.46	
Mn^-	$(3d)^8$	1	2.0104	-71.28

Table 4: Previously obtained ESR signal of interstitial Si:Mn

made using pure Si as host exhibits the strongest signal, while that made using p-type Si shows weakest signal of the three. We could not get the signal other than Mn_i^0 in these three type sample. Figure 21 shows the signal around $g = 2.0$. Quenched Si exhibits the remarkable structure at g=2.076 and g=2.009 which is not seen in pure Si. Si:Mn exhibits the similar behavior but not with sharp peak. This sharp signal is probably related to some kind of defect produced at the quenching procedure. Therefore it may exist in the Si:Mn sample. This result implies that certain amount of coupling of Si defect center and Mn atom which produces the ESR-inactive center and make the sharp signal decrease in Si:Mn sample. Figure 22 shows the temperature dependence of $Mn_i^0(S = 1/2)$ signal at g=3.375. The steep decrease occurs when temperature is raised and signal is almost hidden into noise at above 7 K. It is known that Mn_i^0 can

exist with two spin states which has deferent g-value as shown in Table 4, that is S=3/2 (g=1.46) and S=1/2 (g=3.362). It is also known that S=3/2 state is the excited state of S=1/2 state (see section 3.5). This quenching behaviour of ESR-signals seems to be caused by thermal excitation, but the signal expected to grow at around $g = 1.46$ was not observed probably because of weak signal intensity. Since the excited states generally has unstable feature, it is probable that such state is hard to observe compared to the ground state.

Next, we examine the illumination effect on the ESR signal because our cyclotron resonance measurement was always done under the condition that the excitation by the Xe flash lamp exist. Sample illumination was made by use of Xe continuous lamp. Figure 23 shows the illumination effect on $Mn_i^0(g = 3.362)$ signal of Mn doped p-type Si. The signal intensity was enhanced when the filtered light was illuminated on the surface. But without filter, the signal is weakened on the contrary. The dependence of signal intensity on illumination intensity is shown in Fig. 24. When weak illumination is applied, signal grows as illumination intensity is raised. This enhancement with illumination can be recognized even with the weakest illumination intensity we applied. On the contrary, it is observed that much stronger illumination decreases the signal intensity as shown in figure. Reminding the strong temperature dependence of this signal, it may be caused by heating of the sample under strong photoexcitation. Because our cooling system is the gas flow type, we can not say it is much efficient under strong illumination. These illumination was

also applied on Si:Mn made using pure Si and that made using n-type Si. But Si:Mn with pure Si exhibits no detectable change in signal strength except for damping caused by heating. The sample with n-type Si shows the slight enhancement with illumination, but its not as large as that of p-type Si:Mn.

Illumination of continuous light on n-type Si:Mn yield the new peak at around g=2 which is shown in Fig. 25. This signal can be attributed to neutral phospher. Phospher atom has the I=1/2 nuclear spin which yield two peaks in ESR signal according to equation (3.5.4). Figure 26 shows the dependence of peak to peak intensity of phospher signal on illumination strength. The signal can be seen to be almost proportional to illumination. This result implies that in n-type Si:Mn at low temperature, phospher donors are fully compensated with certain acceptors created by thermal treatment they are neutralized by photoexcitation. The signal appeared in quenched Si at around g=2.0 showed no response to illumination except for the growth of small signal at g=2.004 which should be attributed to free electron signal because of its g-value.

4.4 PL measurements

The result of photoluminescence is depicted in Fig. 27. The peak labeled FE is free exciton luminescence and EHD means that of electron-hole drop. BE denotes neutral donor bound exciton for n-type Si and neutral acceptor bound exciton for p-type Si. Pure Si exhibits the well known peak of FE and EHD due to the lack of luminescent center like shallow impurities.

On the other hand, quenched Si and Si:Mn shows no luminescence with detectable intensity which seems to be due to the defects introduced at the quenching which act as the efficient non radiative recombination center. And p-type Si and n-type Si exhibits the bound exciton luminescence which feature is also well known. The points one should notice is that Si:Mn sample which experienced the post annealing process of $500°C$ 4 hours recovers the FE and EHD feature and slowly cooled Si:Mn exhibits the feature same as pure Si not as n-type or p-type Si. This means that the Mn diffusion process at the temperature as high as $1100°C$ did not introduce shallow impurities which usually act as luminescent center as seen in n-type or p-type Si and that broadening of cyclotron resonance line width in Si:Mn is not caused by such shallow impurities which are in danger of introduction by heat treatment and are usually hidden under high compensation ratio.

4.5 DC measurements

The room temperature resistivity of various Si and Si:Mn sample measured by usual four-point technic is shown in Table 5. It is seen that Si:Mn has very low resistivity while pure Si and Quenched Si and slowly cooled Si:Mn have high resistivity and that high resistivity is recovered after post annealing procedure. The remarkably high resistivity of p-type Si:Mn is due to coupling of Mn and boron. Si-B complex is well known to become the donor at around $E_c - 0.53eV$. This donor level may compensate the shallow acceptor and donor itself is too deep to supply carriers to conduction

band even at room temperature. This makes sample resistivity very high. Figure 28 shows the temperature dependence of carrier density of Si:Mn sample derived from Hall coefficient. Carrier type obtained is electron and the activation energy is fit to $227meV$. Donor density can not be obtained straightforward by this figure because the temperature does not yet reach to the extrinsic range even at room temperature. But slight bending at near 300K allows us to estimate it to be order of $10^{15}cm^{-3}$. Comparing this with cyclotron resonance result and photoluminescence result, we can say that this donor level related to Mn doping is the cause of CR line width broadening.

4.6 FIR cyclotron resonance

We made the cyclotron resonance experiment at 4.2K using far infrared laser to investigate the magnetic field dependence of inverse relaxation time of electron. The results is depicted in Fig. 29 and 30. In Fig. 29, it can be seen that Si:Mn has almost the same line width compared to pure Si while micro wave mesurement shows the remarkable difference between these two sample. Figure 30 shows the genuin inverse relaxation time due to the Mn introduction which is derived by subtracting pure Si component from the obtained bare line width. It can be seen that for cyclotron resonance experiment under high magnetic field, the effect of Mn introduction is reduced, that is similar to the case of scattering by shallow impurities.

4.7 Room temperature postannealing

Because of their large diffusion constant, transition metal atoms easily move around in Si crystal even at rather low temperature and precipitate onto surface and which is the reason why we must quench samples into liquid after Mn diffusion at high temperature. Figure 31 shows the room temperature annealing effect on cyclotron resonance line width and ESR signal intensity for Si:Mn. We prepared the several sample which were made at different day to execute this experiment. We decide the annealing time to the days past from the day it made to the day it measured. The sample which suffer longest annealing time is that of about 400 days. We can immediately see the fact that inverse relaxation time is decreasd only by apploximately 40 % with annealing time while ESR signal is decreased by $2 \sim 3$ % in 100 days. ESR signal is saturated to decrease after 100 days past. This result apparently says that the origin of cyclotron resonance line broadening and that of ESR signal are different. The similar fast decreasing is obtained by Nakashima [20] for DLTS signal of interstitial Mn.

4.8 Stress effect on line width of cyclotron resonance

Figure 32 shows the stress dependence of inverse relaxation time for Si:Mn. The stress was applied to $< 111 >$ direction not to change the occupation of the six equivalent valley relatively. In the case of p-type Si with shallow acceptors, it is known that the electron momentum relaxation time at low temperature is almost governed by the neutral acceptor bound exciton

scattering. [25] Neutral acceptor has the smaller scattering cross section compared to that of donor. But when it capture the exciton, it is known that it turn to be donor like. This make cross section larger according to the theory of neutral impurity scattering as described in section 2.3.3. It is also known that the stress applied to lower the system symmetry makes the generation of bound exciton difficult. Our result shows no damping of inverse relaxation time in increasing stress. And moreover no luminescence line was observed near band gap energy. It is expected that some kind off luminescence should be observed if the bound exciton exist because of its high radiative recombination efficiency. Its energy is expected to be one tenth of impurity binding energy (Heynes rule) less than free exciton luminescence energy. Accordincly, in the present case we can say that the bound exciton is not responsible for the broadening of cyclotron resonance line width.

Sample	Resistivity (Ω-cm)
Pure FZ Si	3196
Quenched Si	3251
Si:Mn	106
Si:Mn (postannealed)	3951
Si:Mn (slowly cooled)	2569
n-type Si:Mn	6.78
p-type Si:Mn	27000

Table 5: four-probe resistivity

5 Discussions

5.1 ESR, DLTS and DC measurements

It is known that transition metal in Si favour the interstitial site [14, 15, 16]. Mn in Si interstitial site can have four charge state according to the theory. These are $Mn_i^-(3d)^8$,$Mn_i^0(3d)^7$,$Mn_i^+(3d)^6$ and $Mn_i^{2+}(3d)^5$. These Mn_i state transferred initial 4s electrons into 3d orbital or other atom. In n-type Si which have sufficient number of donor, Mn atom act as acceptor and traps one electron from donor, compensate it and become Mn^- state. The number of this Mn^- is owes to the number of Mn atom and donor atom and to distribution function. If the number of donor atom is insufficient to fill all Mn atom, the rest remains neutral, that is, Mn^0 state exists in the same time. When these negatively charged and neutral Mn atom is put into depletion layer neighboring to the Schottky barrier interface, each Mn atom will release one electron and become Mn^0 and Mn^+ respectively. So, we can observe following two process in DLTS results in such sample.

$$Mn_i^0 \overset{filling}{\longrightarrow} Mn_i^- \overset{0.11eV}{\longrightarrow} Mn_i^0$$

and

$$Mn_i^+ \overset{filling}{\longrightarrow} Mn_i^0 \overset{0.41eV}{\longrightarrow} Mn_i^+$$

Energy diagram of interstitial Mn is depicted in Fig. 7. In p-type Si, on the contrary, Mn can act as donor and compensate acceptor. We can expect two states, Mn^+ and Mn^{2+} which are the states which traps one and two holes respectively. The number of occupation of these states is owing to the number of compensating acceptor. In actual, only $Mn^{2+/+}$

can observed in DLTS on p-type Si:Mn. It is,

$$Mn_i^+ \xrightarrow{filling} Mn_i^{2+} \xrightarrow{0.30eV} Mn_i^+$$

The transition $Mn^{-/0}$ is called as acceptor, $Mn^{0/+}$ as first donor and $Mn^{2+/+}$ as second donor. We have observed the former two signal in n-type Sample.

In ESR measurement, we have observed the strongest Mn_i^0 signal in the sample with pure Si host. This is consistent with above description. In n-type Si:Mn we observed the rather strong signal intensity of Mn_i^0. So, we can say that the concentration of interstitial Mn exceeds that of shallow phospher donor which amount is $3 \times 10^{14} cm^{-3}$. In p-type Si:Mn ESR result shows that most of interstitial Mn is charged to Mn_i^+ and the signal intensify of Mn_i^0 become least of the three type of sample we measured. But, we observed the enhancement of Mn^0 signal when weak illumination was applied on p-type Si sample. This means that the neutralization of Mn_i by the carrier generated by illumination was occurred. It is remarkable that even with the very weak illumination, signal enhancement occurred. It is known that the pulse illumination applied to generate free carriers necessary for cyclotron resonance neutralize almost all shallow impurities and make it hard to observe the ionized impurity scattering at low temperature. We can say that about the same situation occurs in our Si:Mn case. Reflecting the occupancy of Mn^0 states, n-type Si:Mn exhibits the weak response to illumination but signal is enhanced slightly. The appearance and growth of phospher signal by illumination in n-type Si:Mn can be understood bye the assumption that the full compensation of donor by

Mn acceptor occurs. This also support the excess of Mn concentration to that of phospher. But the strongest illumination we applied could not lead to the saturation of the signal intensity.

Room temperature DC measurement revealed the very low resistivity of Si:Mn with pure Si host compared to other pure Si originated sample. The conduction type of this sample known from Hall measurement is n-type and its activation energy is found to be about $E_c - 0.23eV$ and its concentration is deduced to be $10^{14} \sim 10^{15} cm^{-3}$. This value for activation energy is slightly different from $E_c - 0.27eV$ which is assigned by Czaputa et. al. [21] to be Mn_4 cluster. But there is no energy level other than Mn_4 around this energy which is previously assigned as Mn related states in Si. Our DLTS measurement shows the small peak at around 130K which is assigned by Nakashima [20] as the $Mn_4(E_c - 0.27eV)$ signal. He observed the growth of this signal accompanied with the decreasing of the signal of interstitial Mn in the long period room temperature annealing. This behavior is to be attributed to the Mn_4 cluster formation. In Si:Mn with host Si doped to n-type or p-type, Mn is charged up because of the compensation as described above. So, the clustering of Mn atom probably prevented by coulomb repulsive force. It is known that Mn_4 cluster is formed easier in pure Si host [26] because it retains the neutralized feature. So we conclude that the Mn_4 cluster is formed in very high concentration in excess of $10^{14} cm^{-3}$ in this type sample.

Room temperature resistivity for Si:Mn made using n-type Si exhibits the value about the same but slightly smaller to initial value. We have

seen that the phospher donor in this sample is fully compensated by Mn_i^-, but its activation energy is obtained from DLTS about $E_c - 0.11eV$ which is small enough to supply almost all electrons to conduction band. Indeed, temperature dependence of resistivity exhibits steep rising at temperature about 100K which is twice as high as initial n-type Si where shallow donor has activation energy about 45meV and exhibits steep rising in resistivity at temperature around 50K.

5.2 Cyclotron resonance

From Fig. 17, we see that only Mn diffusion affects inverse relaxation time of electron significantly. DLTS, ESR and DC measurements revealed that about $10^{15}cm^{-3}$ interstitial Mn exist in sample with doped host Si. Comparable amount of interstitial Mn also expected in sample with pure Si host. But it is also revealed that room temperature annealing process decreases the number of interstitial Mn significantly while inverse relaxation time decreases only slightly. On the other hand, we see that Mn_4 cluster formation in excess of $10^{14}cm^{-3}$. We executed Hall measurement again on the same sample after about 200 days of room temperature annealing, but we observed no significant change in room temperature Hall coefficient. Instead, it even looks increased slightly in carrier concentration. So, we conclude that this Mn_4 cluster is responsible for broadening of electron cyclotron resonance line width. It is peculiar that the room temperature annealing effect for inverse relaxation time exhibits the slight decreasing feature while Mn_4 cluster density seems to remain constant. This can be

justified by the assumption that interstitial Mn also affect the electron relaxation time as well as Mn_4 cluster.

5.3 Neutral impurity scattering

It is already known from the previous discussion that Mn_4 as well as Mn_i may be neutralized under pulsed illumination in the cyclotron resonance measurement. We must treat the neutral impurity scattering firstly. Because these center is deep and its Bohr radius of ground state is expected to be very small, usual neutral impurity scattering treatment become no longer applicable because its cross section becomes too small to affect the line width.

5.3.1 Spin scattering

In the case of transition metal in semiconductor, it is known that Hund's rule is often broken if the p-d hyblidization is large compared to exchange energy among (3d)-electron.[14, 15, 16] transition metal in Si is generally the case because of strong covalency of Si. In Si, TM usually expected to prefer the low spin ground state. But it is known that Cr and Mn can have high spin state in Si according to the calculation. And five spin state had observed for interstitial Mn and two for substitutional Mn as shown in Table 4. In addition, Si:Mn shows the ESR signal of Mn_4 cluster [21]. It is probable that these spin can interact with conduction by the spin-spin interaction expressed as

$$\mathcal{H} = J\boldsymbol{S}_M \cdot \boldsymbol{s}_e \tag{5.3.1}$$

where J is the exchange integral, S_M the impurity spin, s_e the spin of conduction electron. This interaction lead to the $T^{\frac{1}{2}}$ temperature dependence of cyclotron resonance line width according to the discussion in section 2.6.2. Neutral impurity scattering case seems to be the special case of spin scattering where J becomes large because of the widely extended Bohr radius of effective mass impurity. Vikhnin et. al. calculated the scattering cross section for the interstitial Fe in Si and conduction electron using the s-d exchange interaction approximation principally same to the theory described in section 2.6.2. The result is

$$\sigma_k = \frac{2l}{3\pi} S(S+1)\eta_k(0)\frac{m^{*2}}{\hbar^4}J_0^2 \tag{5.3.2}$$

where $\eta_k(\boldsymbol{r}) = \frac{1}{\lambda}\left|u_k(\boldsymbol{r})\right|^2$ and $u_k(\boldsymbol{r})$ is a Bloch function of incident electron and l is the number of equivalent valley of conduction band. He obtained the total cross section for the case of Fe in Si ($(3d)^8$,S=1),

$$\sigma = 1.3 \times 10^{-14} cm^2$$

This cross section leads to the inverse relaxation time for the impurities of $10^{15} cm^{-3}$ at T=4.2K,

$$\frac{1}{\tau} = 1.8 \times 10^7 s^{-1}$$

Because the parameters emerged in Vikhnin's theory are not expected to differ so much in Mn case, this value seems too small to explain our Si:Mn result for inverse relaxation time of about $\sim 10^{10} s^{-1}$. The spin scattering is treated by Kasuya et.al. in the case that spins are more concentrated such as the case of diluted magnetic semiconductor.

5.3.2 Resonant scattering

For the next, we can imagine the case that resonant scattering play an important role in the relaxation time of conduction electron. The square well potential is known to have probability of generating a semi-localized resonant states in the $E > 0$ region which is originated in the steep change of potential at the boundary (see section 2.6.1). In the solid state, this situation is enhanced by the band structure.[27] If there is remarkable amount of intervalley transition, that is, $U(\boldsymbol{k}, \boldsymbol{k}')$ has the applicable value between the different valley, the bound state associated to one valley may mix with the continuum state of another valley (valley orbit interaction) which situation is depicted in Fig. 33. This mixed state resonantly scatters the electron in that continuum states according to the manner of Breit–Wigner scattering where the scattering cross section is of the order of the square of electron De Broglie wave length. Therefore, if such resonant state lies near the band edge of conduction band, this resonant scattering is very much responsible in the electron relaxation time in the case of non-degenerate semiconductor. Figure 34 shows our simple calculation of the inverse relaxation time of electron for the resonant scattering with the Breit-Wigner formula. They have about $T^{\frac{1}{2}}$ dependence on temperature at low temperature which originate in the fact that only electrons resonating is responsible to relaxation time and rising of temperature make the population of electron occupies the resonant state high according to the Boltzmann distribution. Further rising of temperature lowers the occupation of the resonant states on the contrary which yield the maximum.

Sankey [28] et. al. shows theoretically that the resonant scattering can dominate the low temperature mobility in the case of sp^3-bonded substitutional deep impurity in zincblende host. Its temperature dependence is almost linear to T at low temperature while our simple calculation yields the $T^{\frac{1}{2}}$ dependence. It seems that the same situation can arise in deep impurity in Si case where strong sp^3 hybridization exist. But our attempt to detect the resonant state using FTIR measurement failed. And the possibility of resonant scattering became much more controversial.

5.4 Ionized impurity scattering

We must not forget the case Mn_4 are not fully neutralized. It is well known that ionized impurities strongly affect the carrier mobility if they exist. But there are only a few sufficient experimental result which detect the ionized impurity scattering directly at low temperature such as $T < 10K$, because of the difficulty for detection of such scattering at low temperature. One reason is that DC measurement fails at low temperature where no carrier is available for they are trapped to shallow impurity. Second, even if one can avoid the shortage of carrier by illumination, as in the case of cyclotron resonance, generated carrier immediately neutralize the ionized impurity even in the compensated sample. There are no longer exist ionized impurities enough to affect the mobility. In such circumstances, Ohtsuka et. al. [29] succeed to detect the ionized impurity scattering by use of cyclotron resonance. They made free carrier necessary for resonance by illuminating sample with far infrared light of energy adjusted to the

binding energy of the impurity. They obtained the scattering coefficient two times less then that obtained from Conwell-Weisskopf (C-W) formula and about ten times less then that from Brooks-Herring (B-H) formula. It evidently demonstrate the collapse of Born approximation at low temperature. The same can be said to our result if our measurement is that capture the ionized impurity scattering. We firstly evaluate our result with B-H formula and C-W formula described in section 2.3.2 which are widely used to evaluate the ionized impurity scattering. If we try to evaluate B-H type scattering formula, it is necessary to evaluate the number of free electron concentration which screen the impurity Coulomb potential. From the result of time resolved cyclotron resonance measurement depicted in Fig. 15, we can evaluate the carrier-carrier scattering contribution. Since other scattering probability is almost independent on carrier concentration, the decaying behavior can be entirely attributed to the contribution of carrier-carrier scattering. Approximating this decaying behavior by simple exponential decay with constant offset, we can get the inverse relaxation time due to carrier-carrier scattering to be $1/\tau = 8.7 \times 10^9 cm^{-3}$ at just after the excitation. Here we can utilized the previous result done by Kawamura et. al. who investigated the broadening of cyclotron resonance line width caused by carrier-carrier scattering. They evaluated the carrier concentration under the light illumination using the plasma shift of absorption peak. They obtained experimentally the value $1/\tau = 1.8 \times 10^{10}(s^{-1})$ for Ge at 4.2K with the electron concentration of about $10^{13} cm^{-3}$. We

here define the experimental condition parameter γ as

$$\gamma = \frac{\omega_c^{\frac{1}{2}}}{\epsilon m^{*\frac{1}{4}} T^{\frac{3}{4}}} \tag{5.4.1}$$

They obtained as the final result that inverse relaxation time caused by carrier-carrier scattering is proportional to $\gamma n^{\frac{1}{2}}$ in the case where condition $k_B T > \hbar\omega$ is satisfied. Here n is the carrier concentration. We can evaluate the value at same temperature,

$$\frac{\gamma_{Ge}}{\gamma_{Si}} \sim 1.03$$

Because also in our case ($T = 4.2K, \omega_c = 35GHz$) the condition $k_B T > \hbar\omega_c$ is satisfied, we can evaluate the carrier concentration for just after the excitation,

$$\begin{aligned} n &= 10^{13} \cdot \left(\frac{1.8 \times 10^{10}}{8.7 \times 10^{9}} \cdot \frac{\gamma_{Ge}}{\gamma_{Si}} \right)^2 \\ &= 2.5 \times 10^{12} cm^{-3} \end{aligned}$$

Because the area under the resonance curve is proportional to carrier concentration participate in resonance, we can plot the time variance of electron concentration. This is shown in Fig. 35 from which we obtain the electron concentration $20\mu s$ after the excitation to be about $5 \times 10^{11} cm^{-3}$. We did not evaluate the carrier concentration for all measurement, and this can vary with the experimental configuration or sample character, but our measurement was always done under almost the same configuration with weakest excitation as possible to extract this carrier-carrier effect, the carrier concentration is expected to be same in order in each measurement. Figures 36 and 37 show the calculated inverse relaxation time using B-H

formula and C-W formula respectively for several impurity concentration. For B-H formula, obtained carrier concentration is used to evaluate the screening length but it is too small to affect the temperature dependence of inverse relaxation time and appeared to have less meaning. It can be seen for any impurity concentration, C-W formula and B-H formula don't explain the temperature dependence of experimental data.

But after the work of C-W and B-H, several authors had proposed the invalidity of Born approximation oriented theory such as C-W and B-H in low energy scattering problem. Sclar's theory [7] and Blatt's calculation [8] both suggests the smaller cross section of ionized impurity for low temperature such as $T < 20K$ than C-W and B-H theory. Moreover their partial wave oriented theory suggests that the negative derivative of mobility respect to temperature while high temperature mobility obeys to $T^{\frac{3}{2}}$ (see section 2.3.2). So, the ionized impurity scattering may explains our slightly temperature dependent relaxation time if impurities are ionized.

6 Conclusions

We conclude that the broadening of the cyclotron resonance line in the Mn-doped Si is mainly due to Mn_4 clusters of density $\sim 10^{15}cm^{-3}$ which have the activation energy of $\sim 230meV$. In the n-type or p-type Si, Mn atoms compensate shallow impurities and ionize themselves, then, the Coulomb repulsion force makes it difficult for Mn atoms to form clusters. Moreover, the ionized Mn atoms tend to couple with ionized shallow impurities. This is remarkable in the case that shallow impurities are acceptors. In pure Si, the Mn atoms hold their neutral feature and it may relatively easy to form clusters. The Mn atoms which remain in the interstitial site will move around even by the room temperature annealing, and some of them precipitate to the surface and some of them form the Mn_4 cluster and others are found at other stable site. SIMS result at just after the preparation of sample showed the Mn density of $\sim 2 \times 10^{15}cm^{-3}$ and it became $5 \times 10^{14}cm^{-3} \sim 1 \times 10^{15}cm^{-3}$ after the room temperature annealing of $\sim$ one year. The result of ESR measurement showed that the density of interstitial Mn decreases rapidly for first 100 days and the ESR signal becomes hard to observe. The Hall measurement showed the 230meV donor with the density of $\sim 10^{15}cm^{-3}$ which is ascribed to Mn_4 cluster, and showed no decreasing after 200 days. By considering above results, we can conclude that both the interstitial Mn atoms and the Mn_4 clusters are responsible for the scattering of electrons in the Mn-doped Si. The initial density of the interstitial Mn is obtained to be $\sim 10^{14}cm^{-3}$ from the DLTS measurements. It is probable that pure Si doped with Mn has

less density of the interstitial Mn because of the Mn_4 formation.

The scattering process should be treated by the formalism of the neutral impurity scattering. If we assume that the density of Mn_4 cluster is $\sim 10^{15}cm^{-3}$, the scattering coefficient $\langle v\sigma \rangle$ becomes $\sim 10^{-5}cm^3s^{-1}$. It is almost same order as the value for the case of Si:P which is a typical shallow donor in Si. In general the wave function of a deep impurity is localized around the atom, and we can say the above coefficient is so large in magnitude. The obtained temperature dependence of the inverse relaxation time is $T^{0.41}$. This temperature dependence is explained by assuming that the scattering is treated as the hard core scattering as the potential become localized and deep.

In the case that (3d)-transition metal impurities have localized spins, the s-d spin interaction can cause the scattering of conduction electrons, and its temperature dependence in semiconductor is calculated to $T^{\frac{1}{2}}$. But the calculation of Vikhnin [30] implies that the inverse relaxation time of $\sim 10^7 s^{-1}$ for $N_I = 10^{15}cm^{-3}$ at 4.2K. It is too small to affect the cyclotron resonance line width.

The deep impurity states are characterized by the shape of impurity potential and the intervalley matrix element. If the energy of deep impurity correspond to one valley coincides the band energy of another valley, and if appropriate amount of invervalley matrix element exist, the resonant state can exists in the band. This resonant state efficiently scatters the band electrons if its energy is near the conduction band edge. The inverse relaxation time due to this resonant scattering is calculated to have

the temperature dependence of $T^{\frac{1}{2}}$. We can not neglect the possibility that such resonant scattering occurs in Si:Mn, but our measurements of the infrared absorption and photo-conductivity spectroscopy showed no evidence for such resonant state.

This work examined the scattering of electrons by deep impurities, and it is probably the first one for Si. Even as a global scattering problem in semiconductor, the investigation of the mechanism of the scattering caused by the central cell potential is not enough. Recently, the first principle calculations have gradually revealed the nature of deep impurity state such as lattice defects, interstitial impurities, substitutional isoelectronic impurities, DX centers and so on. Therefore, We can expect that the scattering problem with these impurities will make progress. I hope this work will become one of the helps for them.

Acknowledgement

I would like to express my gratefullness to Professor Tyuzi Ohyama for supporting my study and experiment, and especially for profitable discussions.

And I am also gratefull to Professor Hiroyasu Nakata for giving me the valuable informations about the exciton problems in semiconductor. I owe a great debt to Dr. Ken-ichi Fujii for his fruitfull discussions about global solid state physics, especially semiconductor physics, and for supporting my computational activities. I am also indebted to Dr. Hiromi Kobori for discussing about the scattering problem, and for giving me the reliable informations about it. I am also indebted to Dr. Katsumata and Dr. Hagiwara of RIKEN for allowing me to use their ESR experimental equipment, and helping me in measurements. I would also like to express my gratitude to my co-workers in Ohyama-Lab., they are, Dr. S.Yoshimura, Dr. Y.Harada, Mr. S.Tsubouchi, Mr. M.Inoue, Mr. T.Iwao, Mr. K.Hirose, Mr. K.Sato and Mr. A.Sugio.

I am especcially thankfull to my parents for supporting me financially and mentally for such long time. I will never forget their help forever.

A Gauss-Neuton Fitting of resonance curve

Here we define the Error function,

$$E(\boldsymbol{p}) = \sum_j (f_j(\boldsymbol{p}) - m_j) \equiv \sum_j s_j \tag{A.0.2}$$

$$s_j = f_j(\boldsymbol{p}) - m_j \tag{A.0.3}$$

where $f_j(\boldsymbol{p})$ is the fitting function with parameter vector $\boldsymbol{p}$, and m_j is experimentally obtained data point. If $\boldsymbol{p}$ is at minimum point of $E(\boldsymbol{p})$, the condition

$$\xi(\boldsymbol{p}) = \frac{\partial}{\partial p_i} E(\boldsymbol{p}) = 0 \qquad (i = 0, 1, 2, \cdots) \tag{A.0.4}$$

Let us expand $xi(\boldsymbol{p})$ around the initial parameter values $\boldsymbol{p}_0$.

$$\begin{aligned}
\xi(\boldsymbol{p}) &= \xi(\boldsymbol{p}_0) + \sum_k (p_k - p_{0k}) \frac{\partial \xi(\boldsymbol{p}_0)}{\partial p_k} \\
&= \frac{\partial}{\partial p_i} E(\boldsymbol{p}_0) + \sum_k (p - p_{0k}) \frac{\partial}{\partial p_k} \frac{\partial}{\partial p_i} E(\boldsymbol{p}_0) \\
&= 2 \sum_j s_j \frac{\partial s_j}{\partial p_i} + \sum_k (p_k - p_{0k}) \frac{\partial}{\partial p_k} 2 s_j \frac{\partial s_j}{\partial p_i} \\
&= 2 \sum_j s_j \frac{\partial s_j}{\partial p_i} + 2 \sum_k (p_k - p_{0k}) \left[\frac{\partial s_j}{\partial p_k} \frac{\partial s_j}{\partial p_i} + s_j \frac{\partial^2 s_j}{\partial p_k \partial p_i} \right]
\end{aligned} \tag{A.0.5}$$

If we set $\xi(\boldsymbol{p}) = 0$, for $\delta \boldsymbol{p} = \boldsymbol{p} - \boldsymbol{p}_0$,

$$\sum_j s_j \frac{\partial s_j}{\partial p_i} + \sum_k \sum_j \delta p_k \left[\frac{\partial s_j}{\partial p_k} \frac{\partial s_j}{\partial p_i} + s_j \frac{\partial^2 s_j}{\partial p_k \partial p_i} \right] = 0 \tag{A.0.6}$$

The third term is negligible at around the minimum point, and

$$\sum_j s_j \frac{\partial s_j}{\partial p_i} + \sum_k \sum_j \delta p_k \frac{\partial s_j}{\partial p_k} \frac{\partial s_j}{\partial p_i} = 0 \tag{A.0.7}$$

if we define $A_{ij} = \frac{\partial s_i}{\partial p_j}$, it becomes

$$\sum_j s_j A_{ji} + \sum_k \sum_j \delta p_k A_{jk} A_{ji} = 0 \tag{A.0.8}$$

$$A^t s + A^t A \delta p = 0 \tag{A.0.9}$$

therefore,

$$\delta p = -(A^t A)^{-1} A^t s \tag{A.0.10}$$

The obtained parameters $p_0 + \delta p$ is not the exact minimum point of $E(p)$ because of neglecting the third term of (A.0.6), but several iteration of this procedure rapidly minimize it.

References

[1] W.Shockley, Phys. Rev. **90**, 491 (1953).

[2] B.Lax, H.J.Zeiger, and R.N.Dexer, Physica **20**, 818 (1954).

[3] G.Dresselhaus, A.F.Kip, and C.Kittel, Phys. Rev. **98**, 368 (1955).

[4] J.Bardeen and W.Shockley, Phys. Rev. **80**, 72 (1950).

[5] E.Conwell and V.F.Weisskopf, Phys. Rev. **77**, 388 (1950).

[6] H.Brooks, Phys. Rev. **83**, 879 (1951).

[7] N.Sclar, Phys. Rev. **104**, 1548 (1956).

[8] F.J.Blatt, J. Phys. Chem. Solids **1**, 262 (1957).

[9] H.M.A.El-Ghanem and B.K.Ridley, J. Phys. C : Solid St. Phys. **13**, 2041 (1980).

[10] C.Erginsoy, Phys. Rev. **79**, 1013 (1950).

[11] H.S.W.Massey and B.L.Moiseiwitsch, Phys. Rev. **78**, 180 (1950).

[12] E.Otsuka, K.Murase, and J.Iseki, J. Phys. Soc. Jpn. **21**, 1104 (1966).

[13] N.R.Kestner, J.J.Morrel, H.Cohen, and S.A.Rice, Phys. Rev. **140**, A 56 (1965).

[14] H.K.Yoshida and A.Zunger, Phys. Rev. Lett. **53**, 1256 (1984).

[15] H.K.Yoshida and A.Zunger, Phys. Rev. B **31**, 7877 (1985).

[16] H.K.Yoshida, Ouyou Butsuri **22**, 326 (1987).

[17] D.Gilles, W.Schröter, and W.Bergholts, Phys. Rev. B **41**, 5770 (1990).

[18] T.Abe, M.Ogirima, and K.Taniguchi, *Silicon crystal and doping* (Maruzen, Tokyo, 1986).

[19] D.V.Lang, J. Appl. Phys. **45**, 3023 (1974).

[20] H.Nakashima and K.Hashimoto, J. Appl. Phys. **69**, 1440 (1991).

[21] R.Czaputa, H.Feichtinger, and J.Oswald, Sol. Stat. Comm. **47**, 223 (1983).

[22] M.Haider *et al.*, J. Appl. Phys. **62**, 3785 (1987).

[23] R.Czaputa *et al.*, Phys. Rev. Lett. **55**, 758 (1985).

[24] K.P.Abdurakhmanov, A.A.Lebedev, J.Kreissl, and Sh.B.Utamuradova, Sov. Phys. Semicond. **19**, 133 (1985).

[25] E. Otsuka, H. Nakata, and Y. Ichikawa, J. Phys. Soc. Jpn. **55**, 2064 (1986).

[26] H.H.Woodbury and G.W.Ludwig, Phys. Rev. **117**, 102 (1960).

[27] F.Bassani, G.Iadonisi, and B.Preziosi, Rep. Prog. Phys. **37**, 1099 (1974).

[28] O.F.Sankey, J.D.Dow, and K.Hess, Appl. Phys. Lett. **41**, 664 (1982).

[29] E.Otsuka, K.Fujii, and K.L.I.Kobayashi, Jpn. J. Appl. Phys. **12**, 1600 (1973).

[30] Vikhnin and Viknin, Phys. Rev. **80**, 72 (1950).

[31] H.Kawamura *et al.*, J. Phys. Soc. Jpn. **19**, 288 (1964).

Figure captions

Figure 1 : SIMS profile for Mn doped FZ pure Si. It can be seen that Mn of $\sim 2 \times 10^{15} cm^{-3}$ has diffused uniformly except for near surface. There can be seen the signals from Cu, Al and Na, but Cu is unimportant for the scattering of electrons, and Al and Na are not exceeding detectable limits which are $3 \times 10^{14} cm^{-3}$ and $1 \times 10^{14} cm^{-3}$, respectively.

Figure 2 : The SIMS profile for Mn doped FZ pure Si after room temperature annealing of about one year. The concentration of Mn is decreased to $\sim 1 \times 10^{15} cm^{-3}$, but it do not have changed more radically than expected.

Figure 3 : Block diagram of microwave cyclotron resonance. The sample is set at the bottom of wave guide, and illuminated by a Xe flush lamp through a glass lod. The light is sometimes filtered to cut high energy part not to make electrons hot and to suppress the high density excitation near the surface. Microwave is generated at the Klystron and guided to sample with 8 mm wave guide. The phase matching is made by Magic-T technique. The signal is put into two channel boxcar integrator, and its output is stored into the personal computer. Magnetic field up to 6000 Gauss is applied using an ordinary split magnet.

Figure 4 : Block diagram of the far infrared cyclotron resonance. The far infrared laser is optically pumped by electric discharge excitation type CO_2 laser and generate the 523 μm line. FIR light is chopped at frequency of 20 Hz before it is guided to sample by about 10mmϕ light pipe.

Figure 5 : Block diagram of DLTS measurements. The sample is settled into helium refrigerator. Capacitance signal is get by digital capacitance meter and stored into personal computer and analysed. The capacitance meter can get whole time variation of transient behavior at one pulse and therefore, it needs only one temperature scanning for several DLTS signal with different rate window which is necessary for arrhenius plot.

Figure 6 : Block diagram of ESR measurement. The sample was settled at the end of quartz rod and cooled to 4 K by blowing of He gas. The temperature is controlled by a heater coiled at the injector and changed from 4K to 300K. The frequency of microwave is 9.11GHz and its power is 4mW. The usual modulation amplitude is 5G and its frequency is 100kHz. The data is obtained in first derivative curve.

Figure 7 : (a):High and low spin state and Energy diagram of Mn spin in Si. If the exchange energy among d-electrons exceed the crustal field energy, the high spin state is favored according to the Hund's rule. On the other hand, under strong crystal field, electrons are tend to make pairs and lower the total spin.

(b):The ESR absorption in the S=$\frac{1}{2}$ case of Mn. The number of six resonant lines are originated in the Mn nuclei spin I=$\frac{5}{2}$.

Figure 8 : Block diagram of photoluminescence measurement. Ar^+ ion laser (4880 Å)is used for excitation light. The light is filtered to cut the plasma noise before illuminate the sample. The luminescent light is also filtered to cut the laser line scattered by the sample before entering into the monochromater which has 600 mm^{-1} grating and about 2 m radius. The monochromated signal is detected by Ge-PIN diode detector cooled with liquid nitrogen, and processed by lock-in technique and stored into personal computer.

Figure 9 : Obtained DLTS signal plot for various rate window. The reverse bias was 5V, the filling bias 0V, and rate window ratio $t_2/t_1 = 10$ where t_1 is varied 10 μs to 10 ms.

Figure 10 : Arrhenius plot of DLTS peak of Fig. 9. We can obtain activation energies for the peaks seen in Fig. 9 from their slope in this figure. They are $E_c - 0.39eV$, $E_c - 0.20eV$ and $E_c - 0.11eV$. The signals for $E_c - 0.39eV$ and $E_c - 0.11eV$ can be attributed to interstitial Mn which were obtained previously by several workers. The signal appears to around $E_c - 0.20eV$ was attributed to Mn_4 cluster [21, 20] or a defect signal [24]. The defect signal should be found in any quenched sample, but we have not observed any signal in such samples.

Figure 11 : Temperature dependence of capacitance of the Schottky barrier formed to achieve the DLTS measurement. We can obtain the density of the deep levels associated to the peak using the relation (3.4.13)

Figure 12 : Typical result of cyclotron resonance measurement on Si at 4.2K. "ECR" means the electron cyclotron resonance and "HCR" means the hole cyclotron resonance. The magnetic field is applied from the direction which separates the three peaks of electron resonance. The smooth solid lines are result of fitting of folded resonance curve. To resolve the folded curve, the non-linear minimum square method is used.

Figure 13 : Three dimensional plot of transient photoconductivity in varying Magnetic field. The magnetic field step of the practically obtained data is about ten times finer than the figure. We can get information from this figure about time resolved change of resonance line width as shown in Figs. 14 and 15.

Figure 14 : Time resolved cyclotron resonance curve obtained from figure 13. The line width of all resonance peak get narrower as time passes.

Figure 15 : Time resolved inverse relaxation time obtained from figure 14. The decaying feature is due to carrier-carrier scattering. The line width is evaluated after 20 μs where the broadening due to the carrier-carrier scattering become negligible. Initial carrier concentration is deduced from this figure to be $5 \times 10^{11} cm^{-3}$ using the result of Kawamura [31].

Figure 16 : Cyclotron resonance curve for Si:Mn and host Si. Remarkable broadening of line width is recognized in Si:Mn sample. Such broadening is not seen in Si:Cr or Si:Fe sample we prepared. The difference in peak position is due to slight deviation of the direction of magnetic field, and it do not affect the line width analysis significantly when we use ECR1 for evaluation.

Figure 17 : Obtained temperature dependence of the inverse relaxation time of Si doped with various transition metal impurities. For the evaluation, the ECR1 peak in Fig.16 is used. The inverse relaxation time for electrons in pure Si exhibits almost $T^{\frac{3}{2}}$ dependence on temperature which is due to the acoustic deformation potential scattering described in section 2.3.1. The Mn doped sample shows the inverse relaxation time about an order larger than that of pure Si, but Si:Cr and Si:Fe show the broadening almost the same to only quenched Si sample.

Figure 18 : Inverse relaxation time for Si:Mn sample subtracted with the host Si contribution. The slope shows about $T^{0.41}$ dependence on temperature.

Figure 19 : Cyclotron resonance curve of sample suffered different annealing process. Slowly cooled Si:Mn is a sample which is doped with Mn without quenching. The Most of Mn atoms are expected to precipitate onto surface and it exhibits almost the same line width to pure Si. Annealed Si:Mn is a sample which experienced the post annealing of 500 $°C$ for about 4 hour. The Mn atom is also expected to precipitate onto surface or moved to the site where Mn atoms are electorically inactive. Quenched Si is a sample which experienced the annealing and the quenching but without Mn doping. This sample is expected to include thermal defect or unintentional Cu doping.

Figure 20 : ESR signal of Mn_i^0 of three types of Si:Mn sample. The calculated g-value is 3.375. This signal is already attributed to $Mn_0^i(S = 1/2)$ in previous work. The sample made using pure Si host exhibits the strongest signal, while that made using p-type Si shows weakest signal of the three. The difference in signal intensity is mostly due to the position of Fermi level, or compensation ratio in another word.

Figure 21 : ESR signal around g=2 for host Si, quenched Si and Si:Mn. The quenched Si exhibits the remarkable structure at g=2.076 and g=2.009 which is not seen in pure Si. This signal is probably related to some kind of defect produced at the quenching procedure. In Si:Mn sample, the defects may passivated by coupling with Mn.

Figure 22 : Temperature dependence of ESR signal of Mn_i^0. The signal intensity steeply weakened as the temperature is raised.

Figure 23 : Illumination effect on Mn_i^0 signal of Mn doped p-type Si. The weak illumination enhances the signal intensity, but too much illumination weaken the signal. This weakening is probably due to the heating of the sample. The sample made with pure Si exhibits no response to illumination without weakening by heating. The sample made with n-type Si exhibits only weak response to illumination, and is slightly enhanced.

Figure 24 : Dependence of Mn_i^0 signal intensity of Mn doped p-type Si on illumination intensity We observed that even very weak illumination cause the enhancement of the signal intensity. As illumination power is raised, the heating of the sample weaken the signal intensity steeply.

Figure 25 : Donor ESR signal of P^0(I=1/2,S=1/2). The signal is very weak under no illumination. This means that phospher atom is initially ionized, and neutralized by illumination.

Figure 26 : Dependence of donor ESR signal intensity on the illumination intensity. The signal intensity is almost linear to the illumination intensity. We see that even under the maximum illumination we apply, the donors are not fully neutralized.

Figure 27 : Photoluminescence of samples which suffered various annealing treatment. Pure Si exhibits the typical free exciton (FE) and electron-hole drop (EHD) luminescence. In quenched Si and quenched Si:Mn, the peaks seen in pure Si disappear due to the rapid non radiative recombination through the defects made in the quenching process. Slowly cooled Si:Mn may have no defects due to the quenching, and it exhibits the same luminescent feature to pure Si. The n-type and the p-type Si exhibits the shallow impurity bound exciton (BE) luminescence instead of FE. When we post-annealed the quenched Si:Mn sample at $400°C$ for about four hour, the FE and EHD feature are recovered by a little amount. We see that the annealing and quenching procedure do not introduce the shallow luminescent centers which act as the efficient scatterers in the cyclotron resonance measurement.

Figure 28 : Hall measurement for Si:Mn sample made using pure host Si. The carrier type is electron, and its activation energy is about 227 meV. This donor can be attributed to Mn_4 cluster. The donor electron is not yet fully ionized even at room temperature, but we can deduce the donor density is under $10^{15} cm^{-3}$.

Figure 29 : Far infrared cyclotron resonance for Si:Mn and pure Si at 4.2K. The line width of Si:Mn is broader than pure Si, but its difference is not as large as in the case of microwave resonance. The cyclotron resonance line width in quantum limit is not accord to the classical description, but we can say that the Mn contribution is small under high magnetic field.

Figure 30 : Inverse relaxation time subtracted with the host contribution for FIR and micro wave cyclotron resonance at 4.2K. This figure shows the Mn contribution to the line width under different magnetic field and different wave frequency.

Figure 31 : Room temperature annealing effect on the inverse relaxation time and the ESR signal intensity. The ESR signal intensity rapidly decreases in 100 days, while the enhancement of the inverse relaxation time due to the Mn doping obtained from cyclotron resonance line width become about a half of initial value after 400 days. This means the origin of cyclotron resonance is not only from the interstitial Mn. The initial decrease in inverse relaxation time may be related to interstitial Mn.

Figure 32 : Stress effect on inverse relaxation time for Si:Mn. If the scattering by the acceptor bound exciton is responsible to the broadening of the cyclotron resonance line width, the application of stress on the sample may reduce the line width.[25] But our result shows no reduction of line width even under the stress of $\sim 1.5 \times 10^6 g/cm^2$.

Figure 33 : The conceptional figure of the resonant state originate in band structure. If there is remarkable amount of intervalley transition matrix element, the bound state associated to valley j may mix with the continuum state of valley i. This resonant state effectively scatters the conduction electron according to the Breit-Wigner formula.

Figure 34 : Calculated inverse relaxation time of resonant scattering using Breit-Wigner formula. We can see that the temperature dependence is $\sim T^{\frac{1}{2}}$ at low temperature. When the mean velocity of electrons exceeds the resonant energy, the mean scattering cross section start decreasing, and it may emerge in the decreasing in inverse relaxation time.

Figure 35 : Time decay of carrier density after excitation derived from the time resolved cyclotron resonance measurement by utilizing the fact that the area under the resonance line is proportional to the number of resonating electrons. The number of electrons just after the excitation is determined from the carrier-carrier scattering contribution to the line broadening.

Figure 36 : The temperature dependence of the inverse relaxation time calculated using Brooks-Herring formula. The density of conduction electron is set to $5 \times 10^{11} cm^{-3}$ which is derived from the carrier-carrier contribution to the line width at the time where resonance is measured. The points in figure show the experimental result for Si:Mn.

Figure 37 : The temperature dependence of the inverse relaxation time calculated using Conwell-Weisskopf formula. The inverse relaxation time depends on the density of ionized impurities, but not on the carrier density in this formula. The points in figure show the experimental result for Si:Mn.

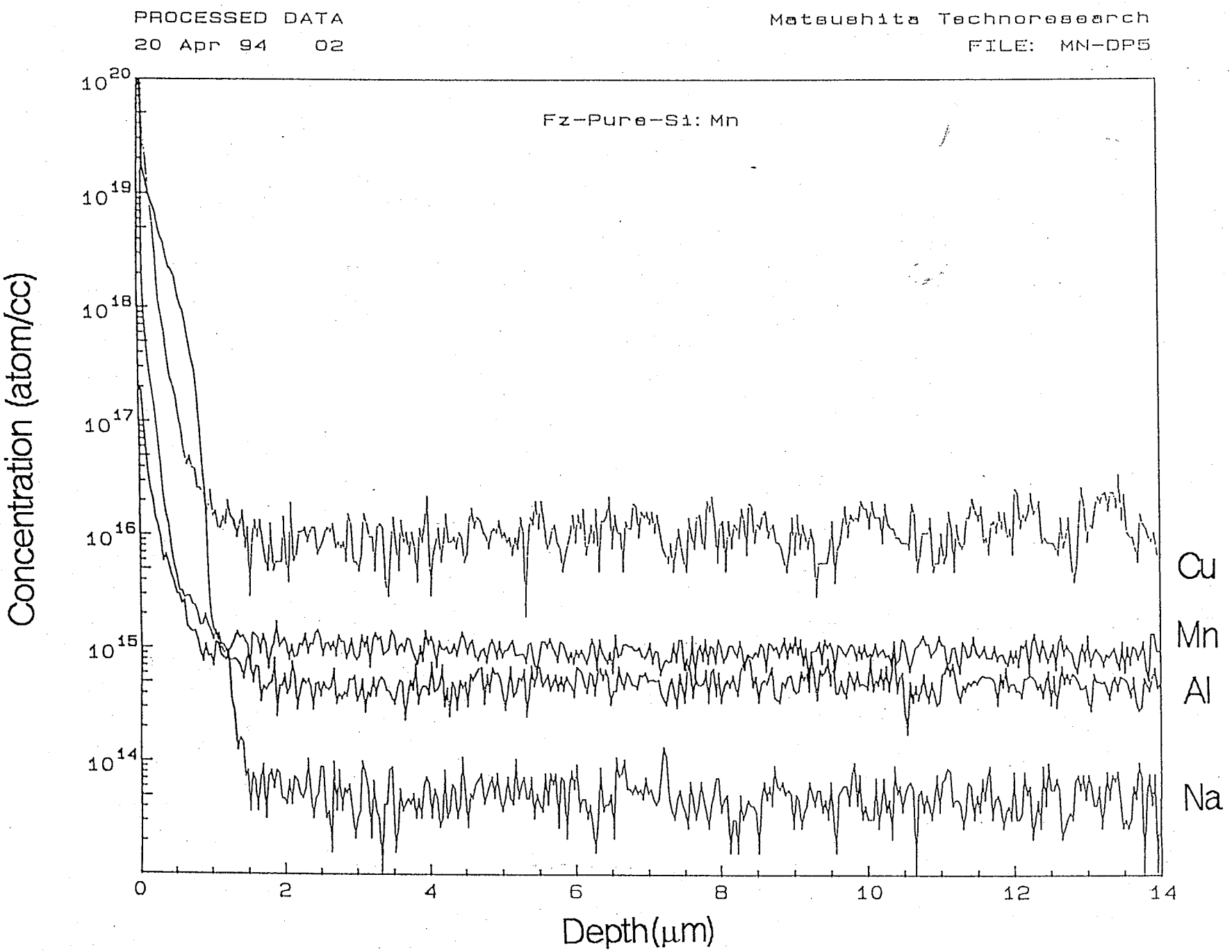
PROCESSED DATA
20 Apr 94 02
Matsushita Technoresearch
FILE: MN-DP5
Fz-Pure-Si: Mn
Concentration (atom/cc)
10^20
10^19
10^18
10^17
10^16
10^15
10^14
0
2
4
6
8
10
12
14
Depth(μm)
Cu
Mn
Al
Na

Figure 1

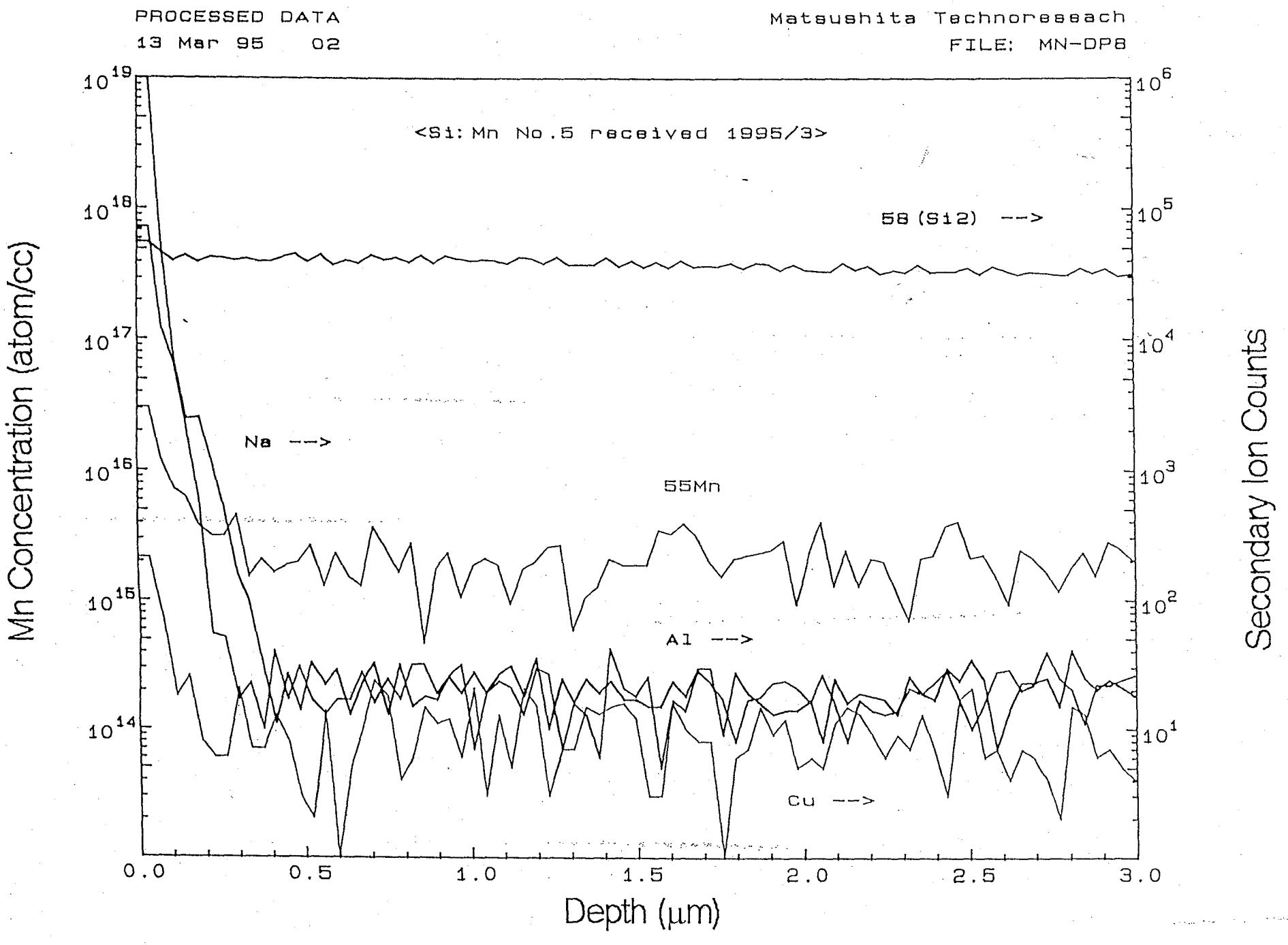
PROCESSED DATA
13 Mar 95 02
Matsushita Technoresearch
FILE: MN-DP8
<Si: Mn No.5 received 1995/3>
58 (Si2) -->
Na -->
55Mn
Al -->
Cu -->
Mn Concentration (atom/cc)
Secondary Ion Counts
Depth (μm)
10^{19}
10^{18}
10^{17}
10^{16}
10^{15}
10^{14}
10^{6}
10^{5}
10^{4}
10^{3}
10^{2}
10^{1}
0.0
0.5
1.0
1.5
2.0
2.5
3.0

Figure 2

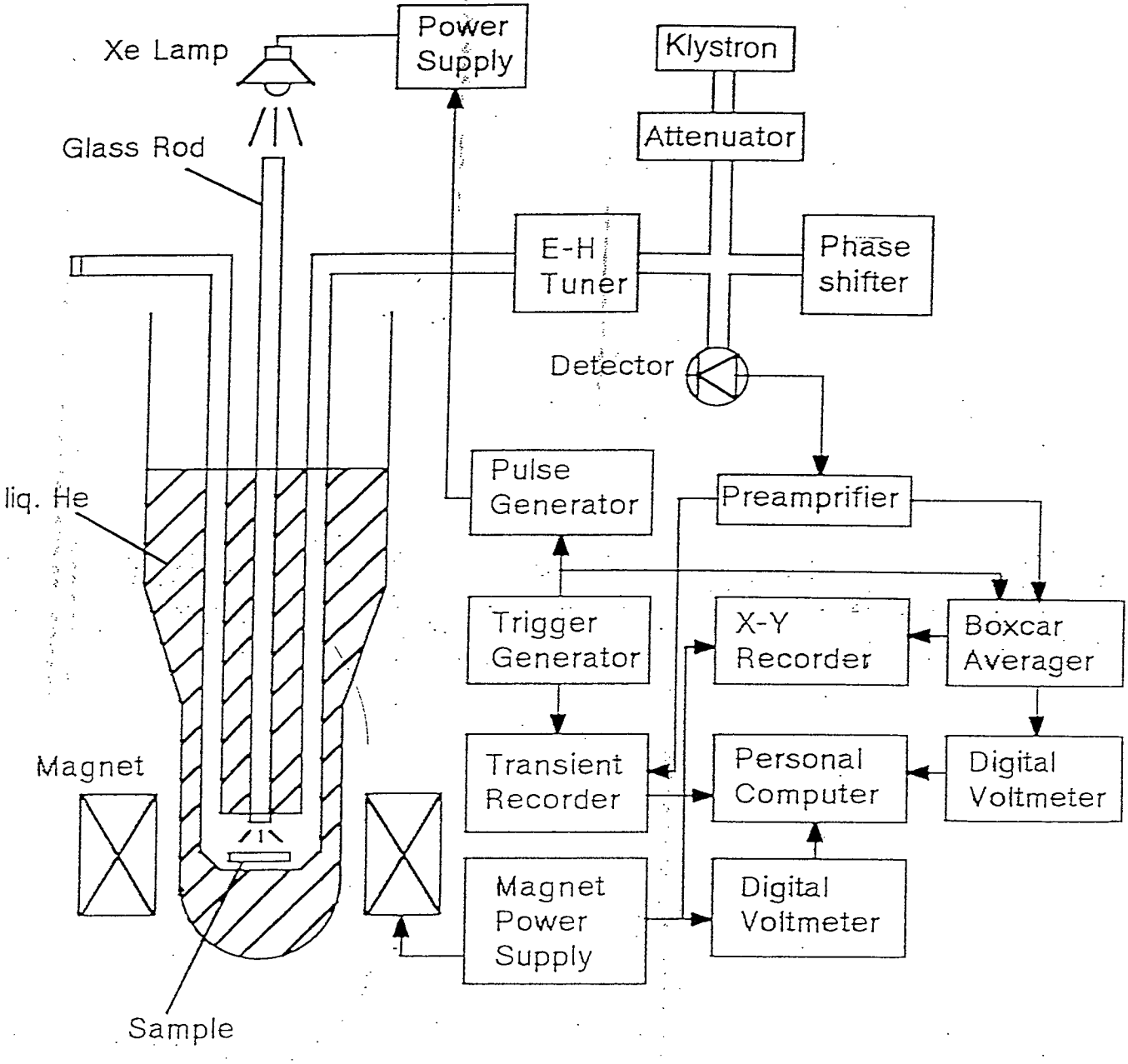
Xe Lamp
Power Supply
Klystron
Attenuator
Glass Rod
E-H Tuner
Phase shifter
Detector
liq. He
Pulse Generator
Preamprifier
Trigger Generator
X-Y Recorder
Boxcar Averager
Magnet
Transient Recorder
Personal Computer
Digital Voltmeter
Magnet Power Supply
Digital Voltmeter
Sample

Figure 3

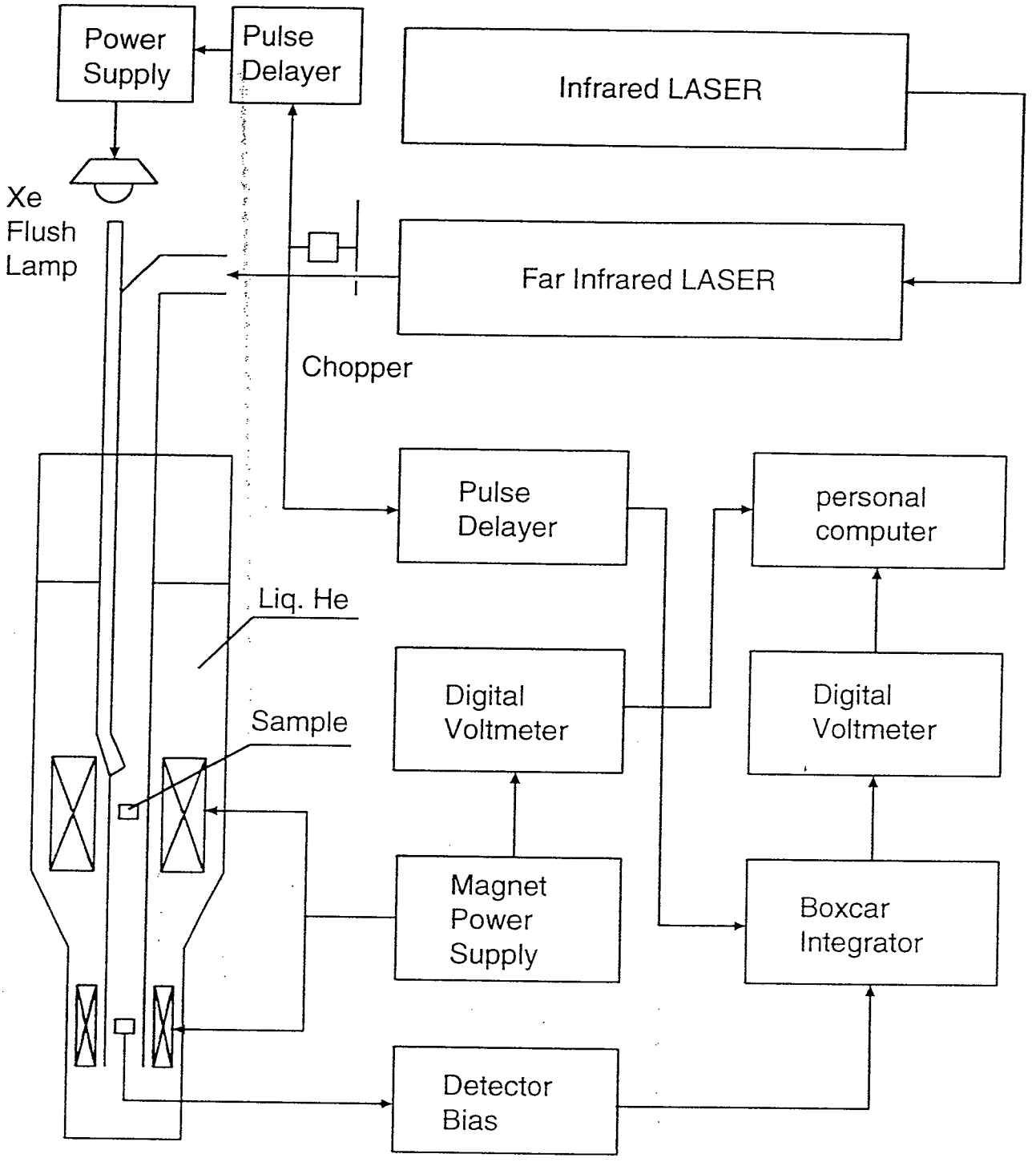
Power Supply
Pulse Delayer
Infrared LASER
Xe Flush Lamp
Far Infrared LASER
Chopper
Pulse Delayer
personal computer
Liq. He
Digital Voltmeter
Digital Voltmeter
Sample
Magnet Power Supply
Boxcar Integrator
Detector Bias

Figure 4

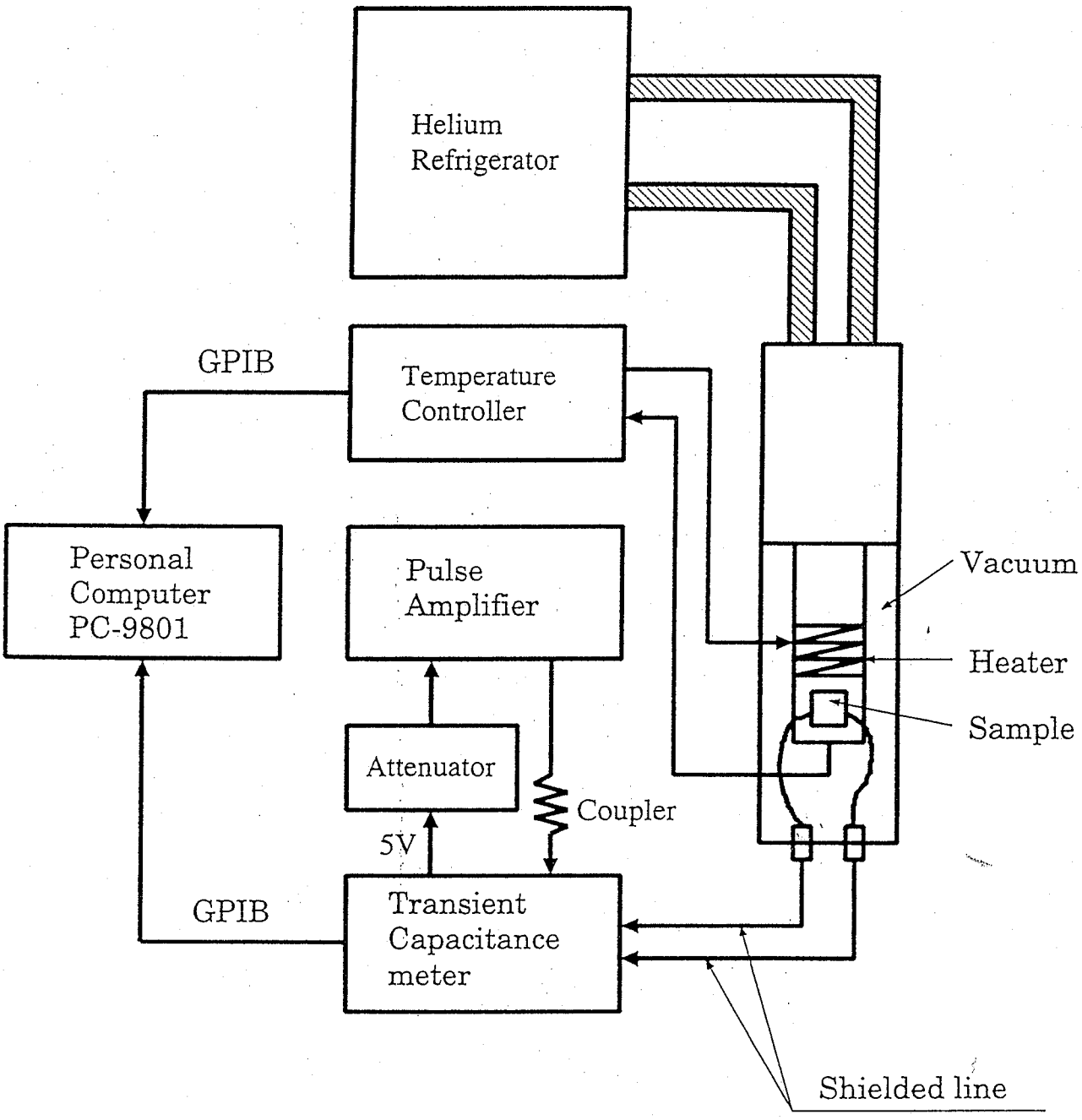
Helium
Refrigerator
GPIB
Temperature
Controller
Personal
Computer
PC-9801
Pulse
Amplifier
Vacuum
Heater
Sample
Attenuator
Coupler
5V
GPIB
Transient
Capacitance
meter
Shielded line

Figure 5

ESR Configuration

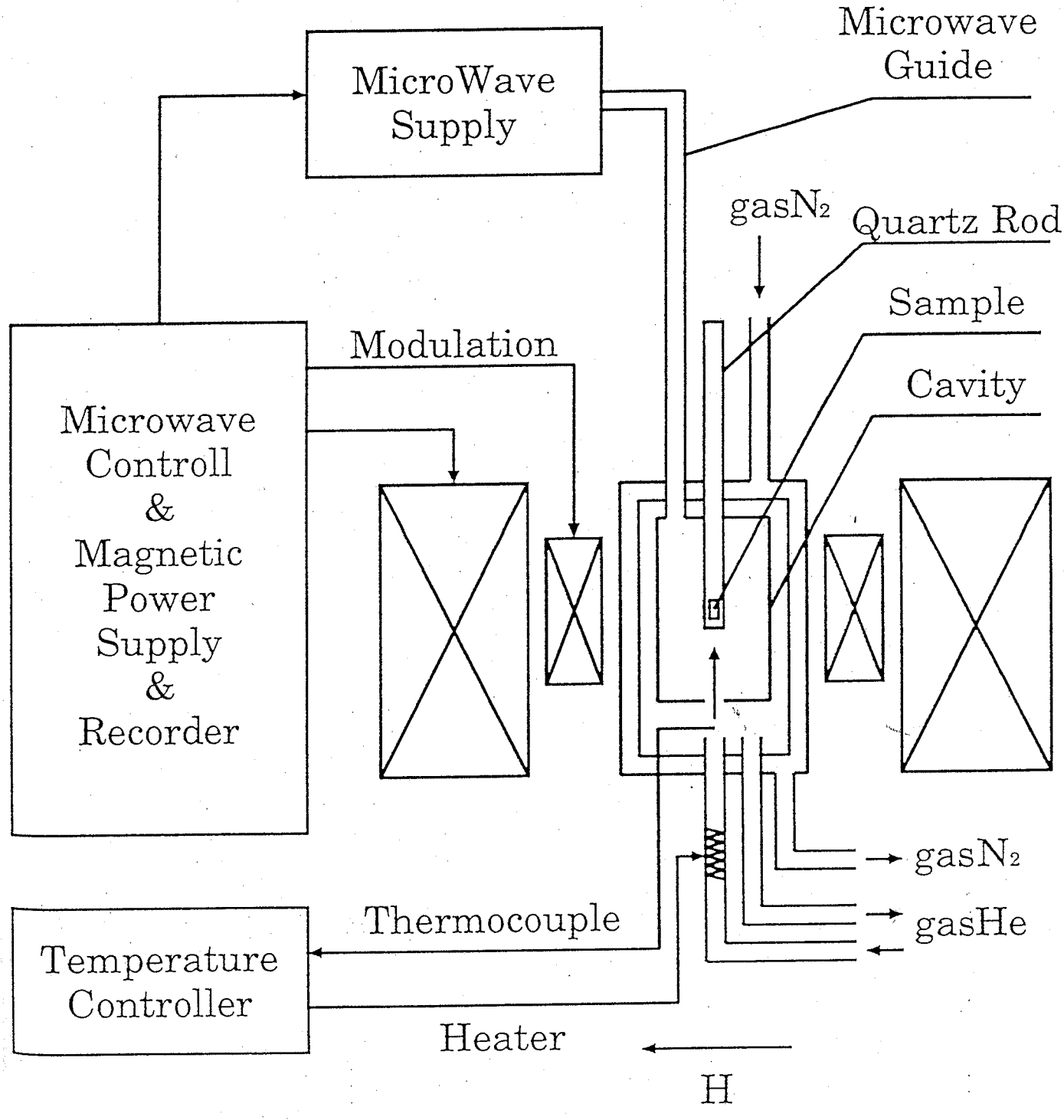

Figure 6

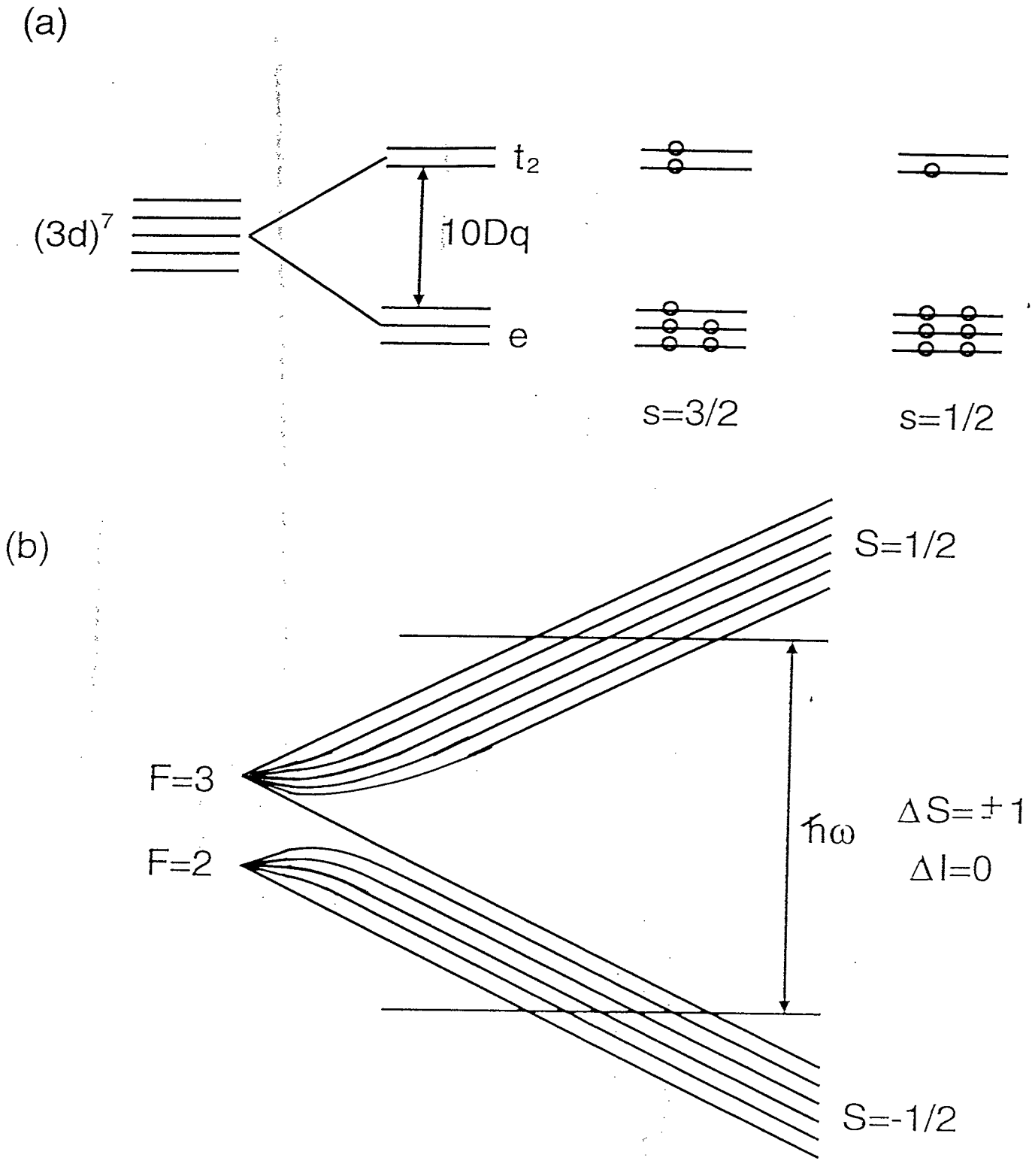
(a)
$(3d)^7$
t_2
10Dq
e
s=3/2
s=1/2
(b)
S=1/2
F=3
F=2
$\hbar\omega$
$\Delta S = \pm 1$
$\Delta l = 0$
S=-1/2

Figure 7

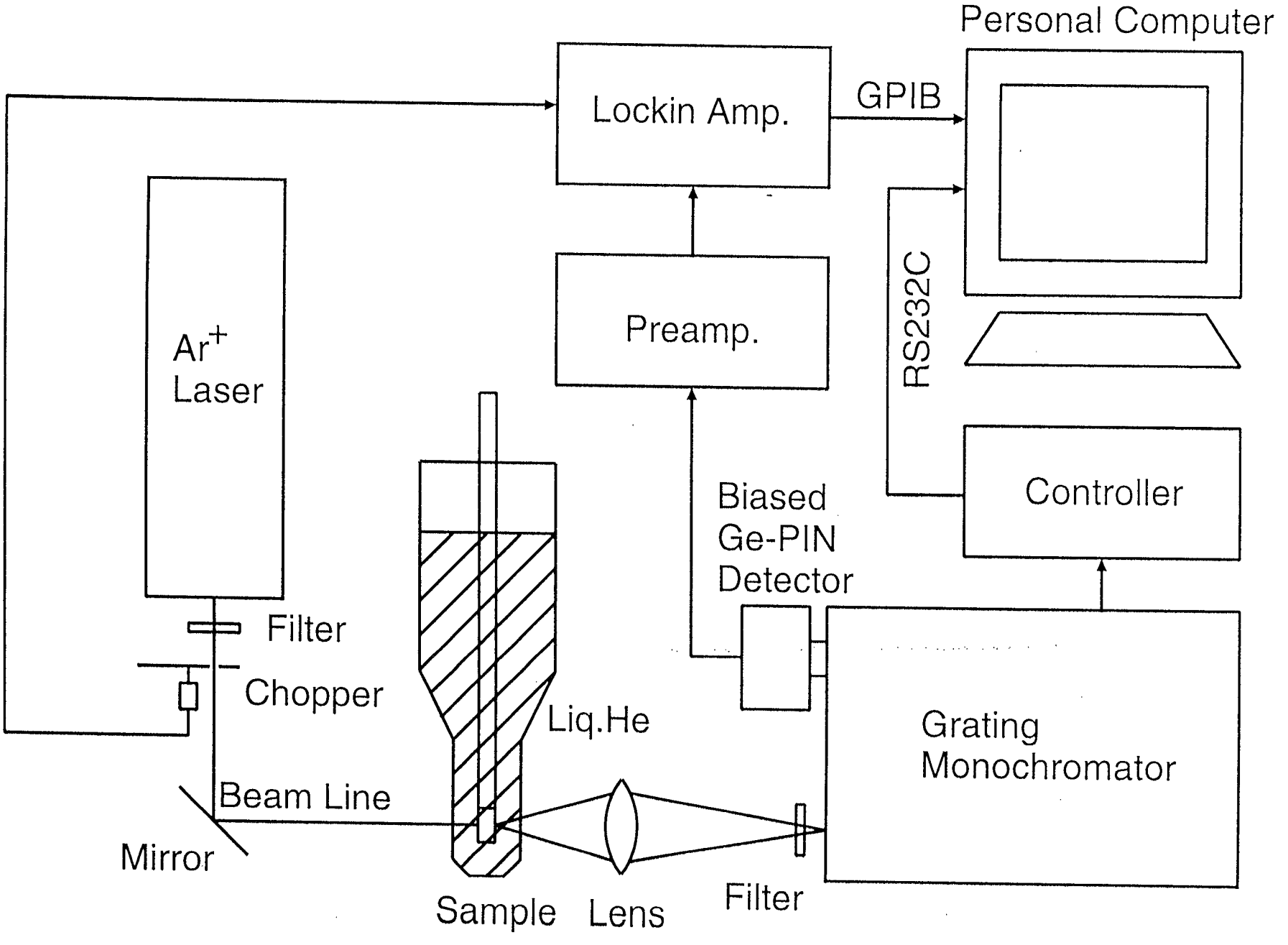
Personal Computer
Lockin Amp.
GPIB
Preamp.
RS232C
Ar+ Laser
Controller
Biased Ge-PIN Detector
Filter
Chopper
Liq.He
Grating Monochromator
Beam Line
Mirror
Sample
Lens
Filter

Figure 8

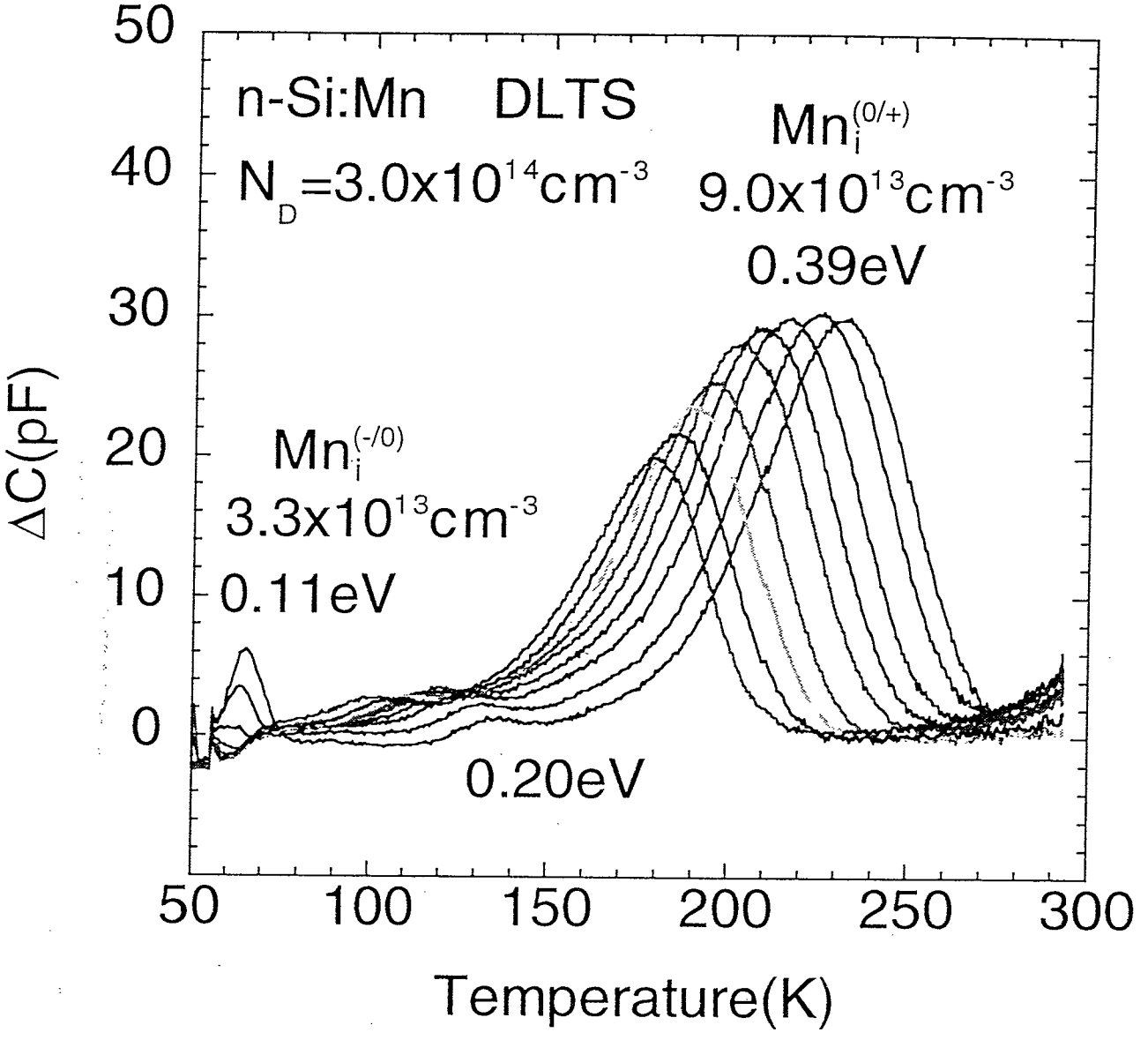
n-Si:Mn DLTS
N_D=3.0x10^14cm^-3
Mn_i^(0/+)
9.0x10^13cm^-3
0.39eV
Mn_i^(-/0)
3.3x10^13cm^-3
0.11eV
0.20eV
ΔC(pF)
Temperature(K)
50
40
30
20
10
0
50
100
150
200
250
300

Figure 9

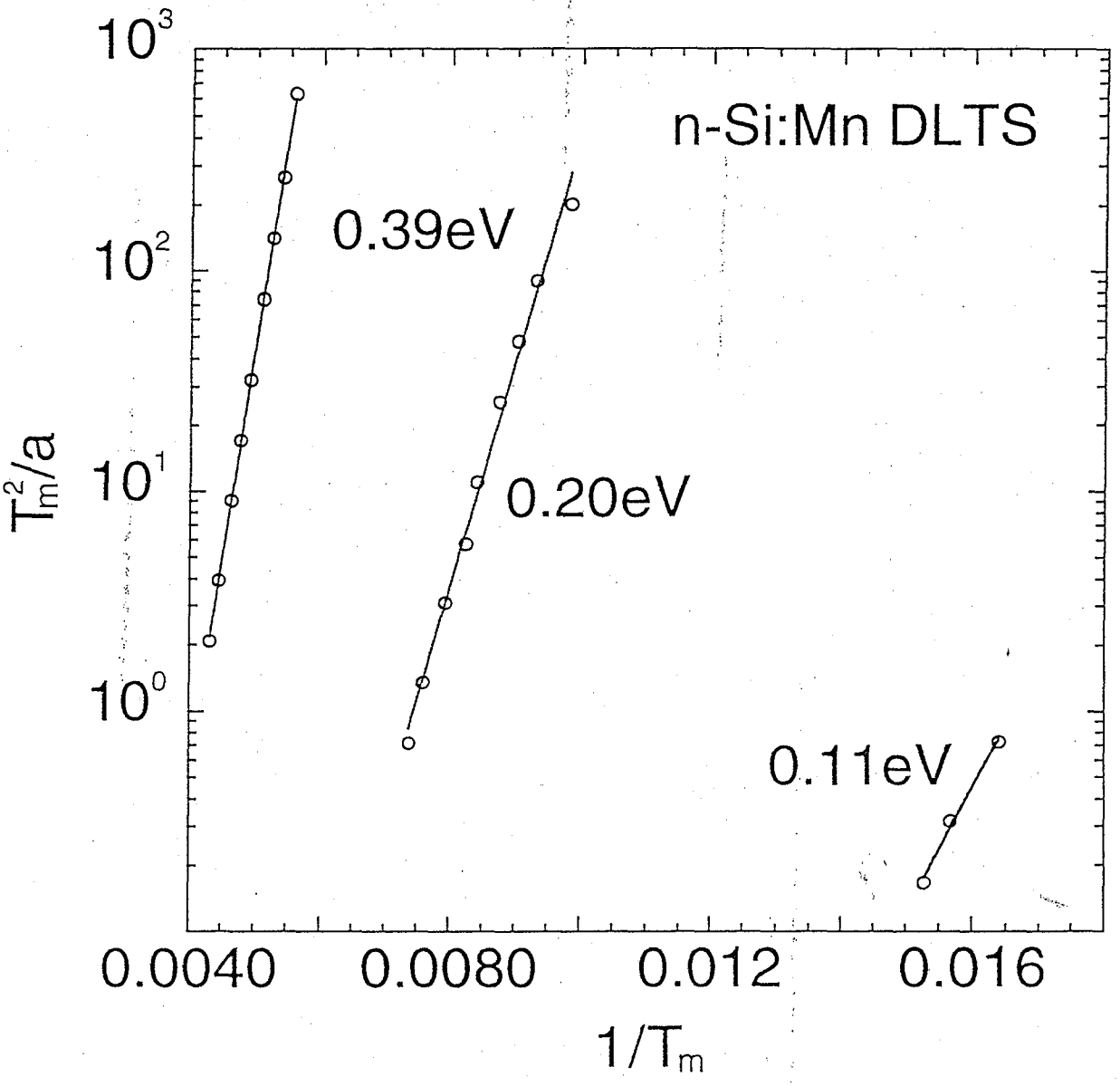
n-Si:Mn DLTS
0.39eV
0.20eV
0.11eV
10^3
10^2
10^1
10^0
T_m^2/a
0.0040
0.0080
0.012
0.016
$1/T_m$

Figure 10

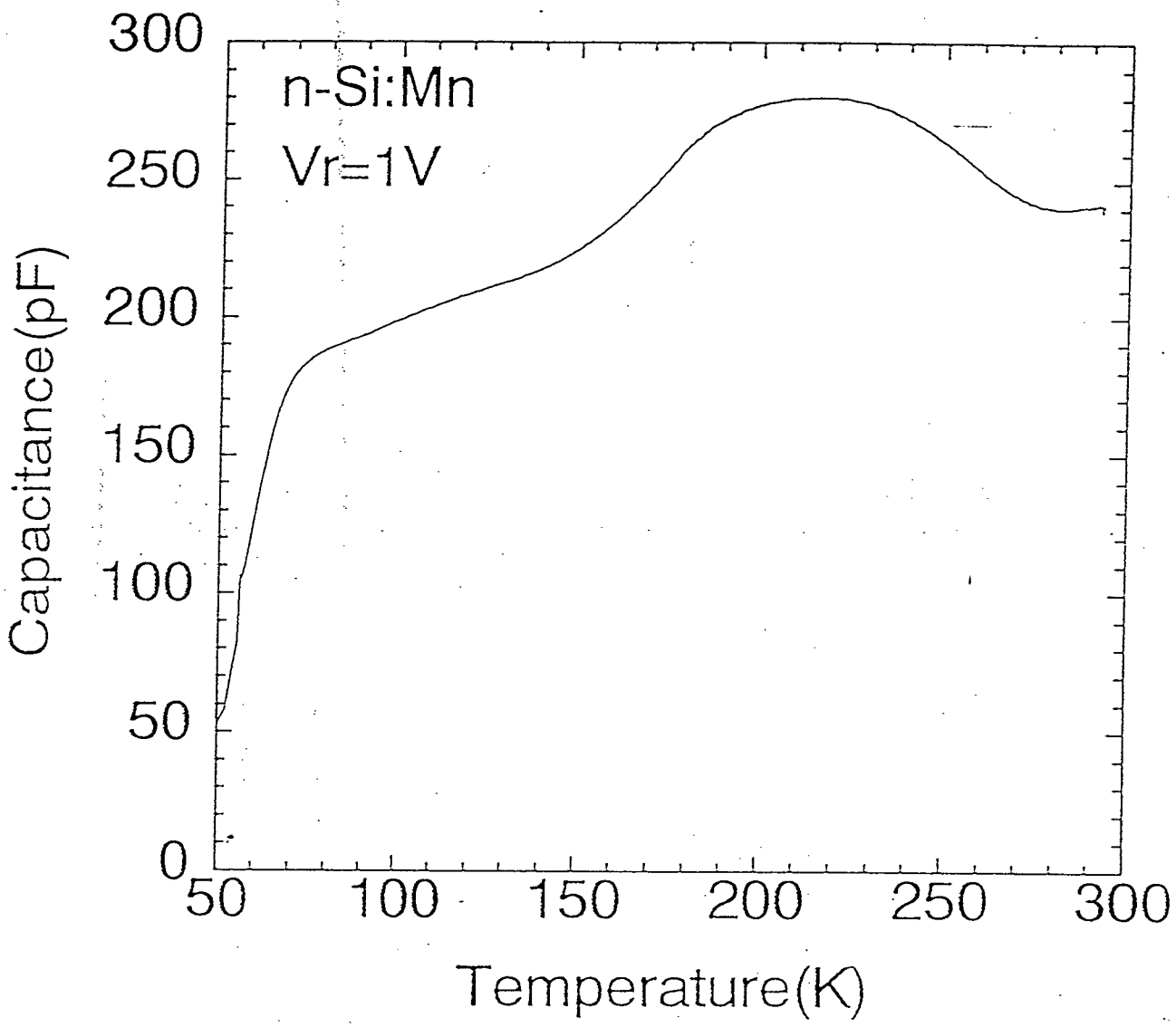
n-Si:Mn
Vr=1V
Capacitance(pF)
Temperature(K)
300
250
200
150
100
50
0
50
100
150
200
250
300

Figure 11

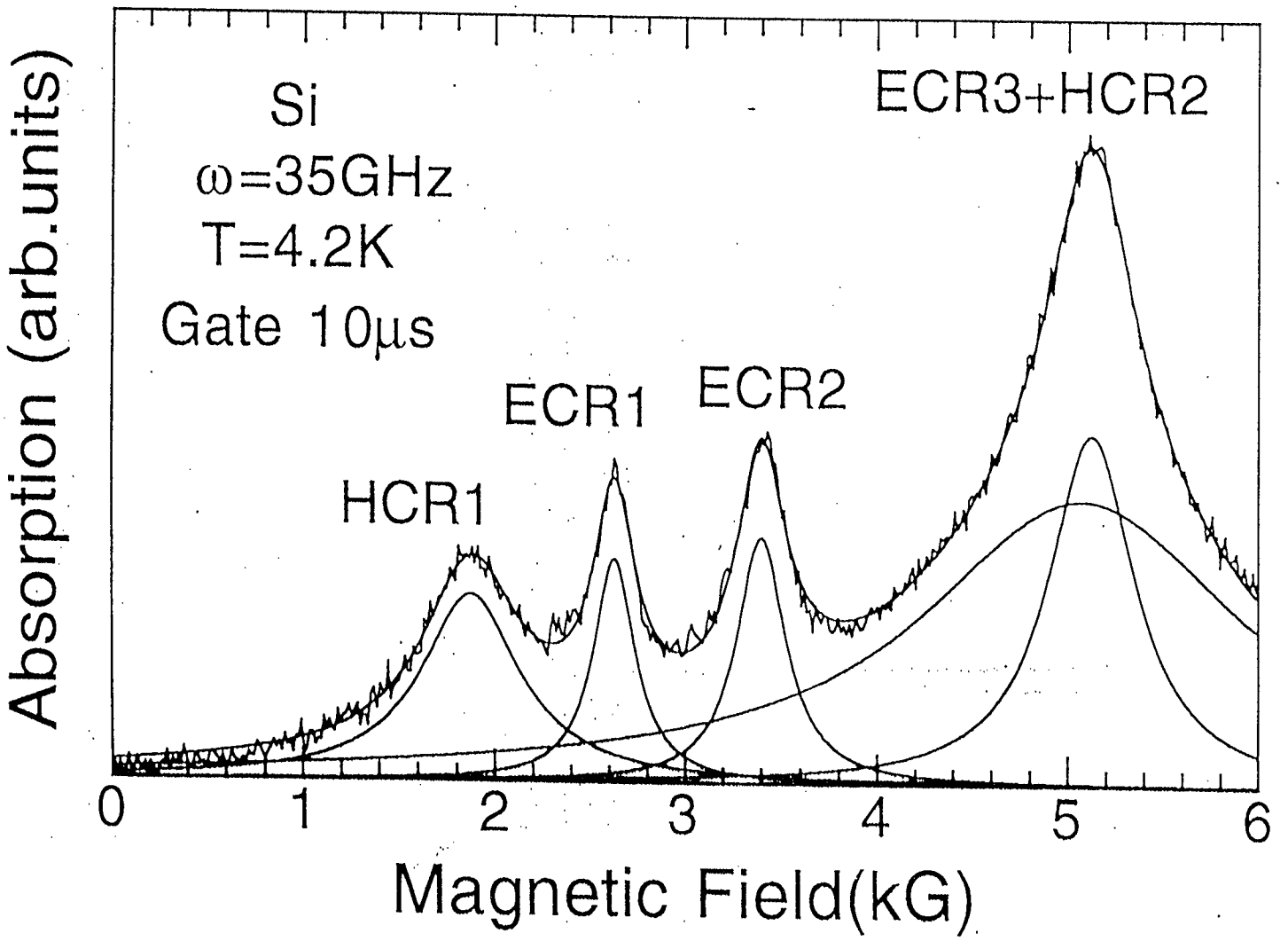
Si
ω=35GHz
T=4.2K
Gate 10μs
HCR1
ECR1
ECR2
ECR3+HCR2
Absorption (arb.units)
0
1
2
3
4
5
6
Magnetic Field(kG)

Figure 12

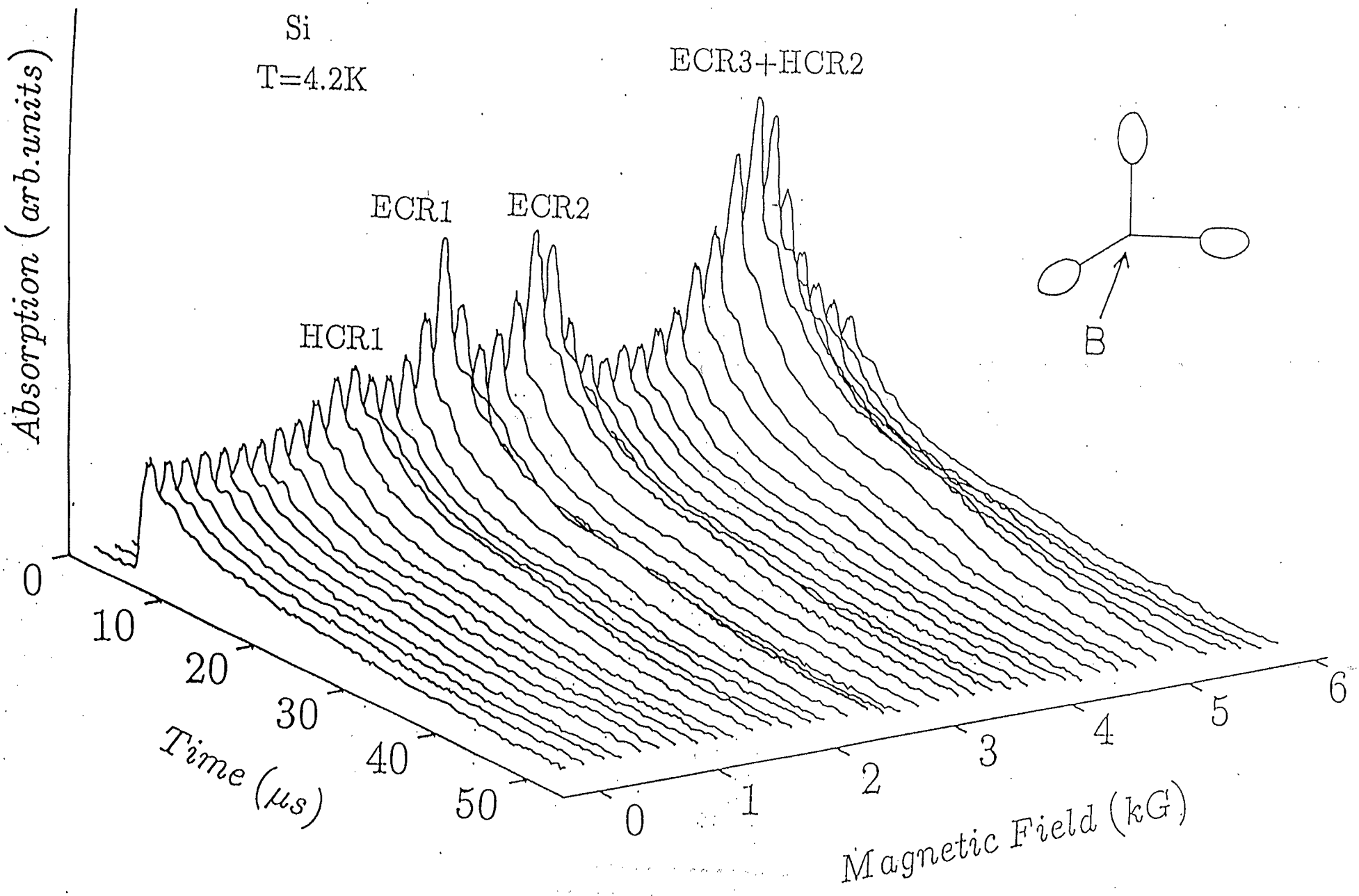
Si
T=4.2K
ECR3+HCR2
ECR1
ECR2
HCR1
B
Absorption (arb.units)
0
10
20
30
40
50
Time (μs)
0
1
2
3
4
5
6
Magnetic Field (kG)

Figure 13

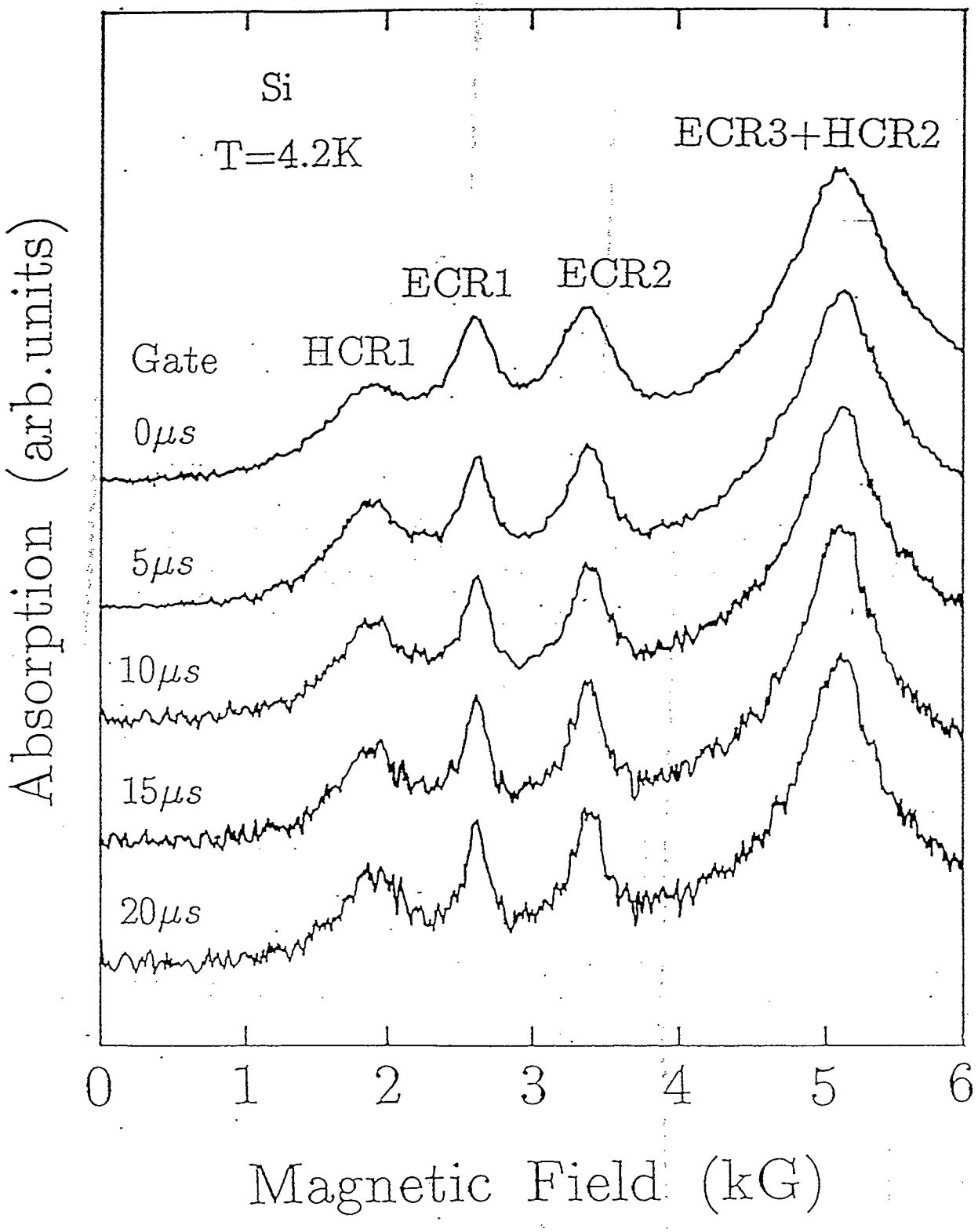
Si
T=4.2K
ECR3+HCR2
ECR1
ECR2
HCR1
Gate
0μs
5μs
10μs
15μs
20μs
Absorption (arb.units)
0
1
2
3
4
5
6
Magnetic Field (kG)

Figure 14

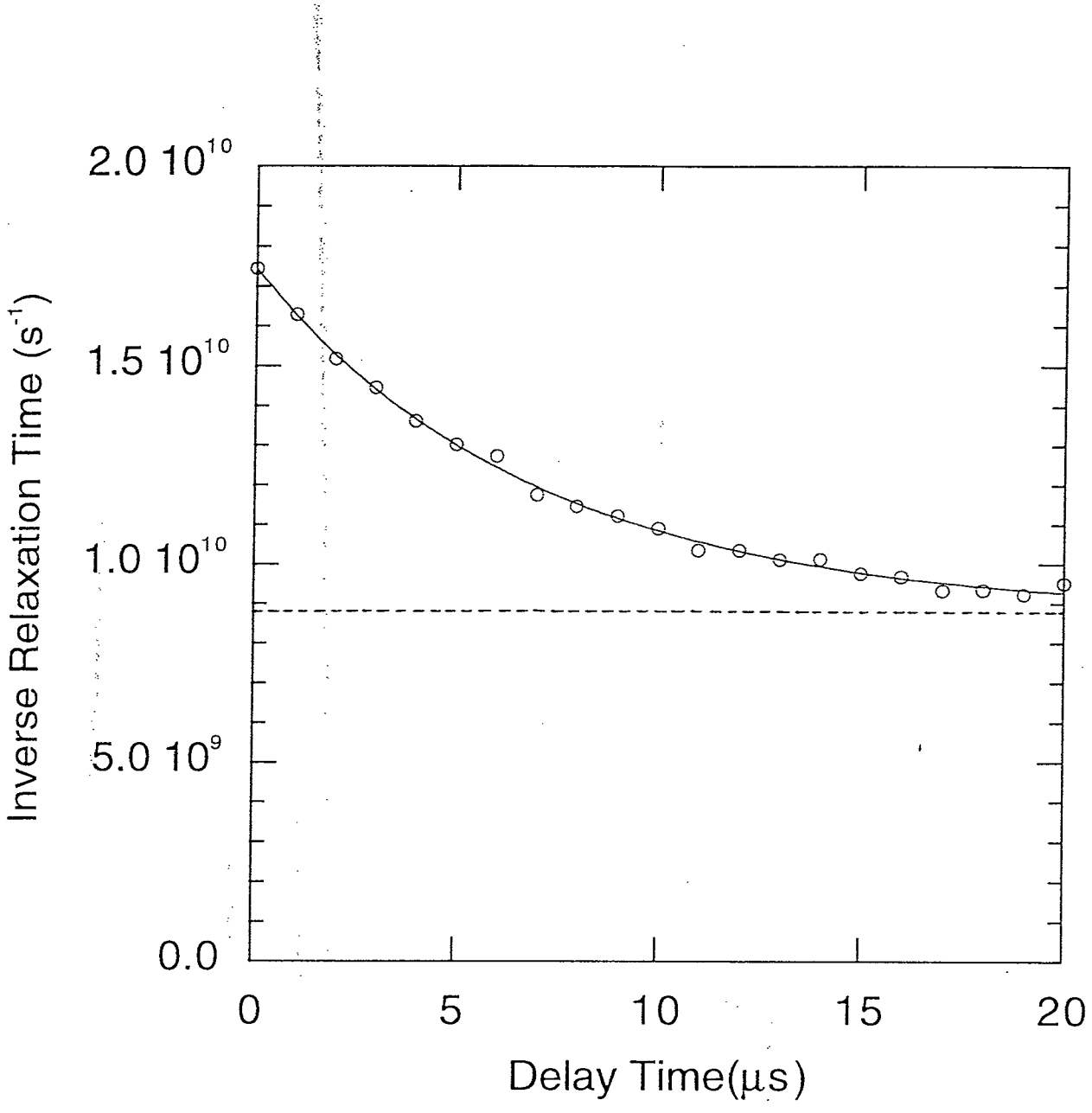
2.0 10^10
1.5 10^10
1.0 10^10
5.0 10^9
0.0
Inverse Relaxation Time (s^-1)
0
5
10
15
20
Delay Time(μs)

Figure 15

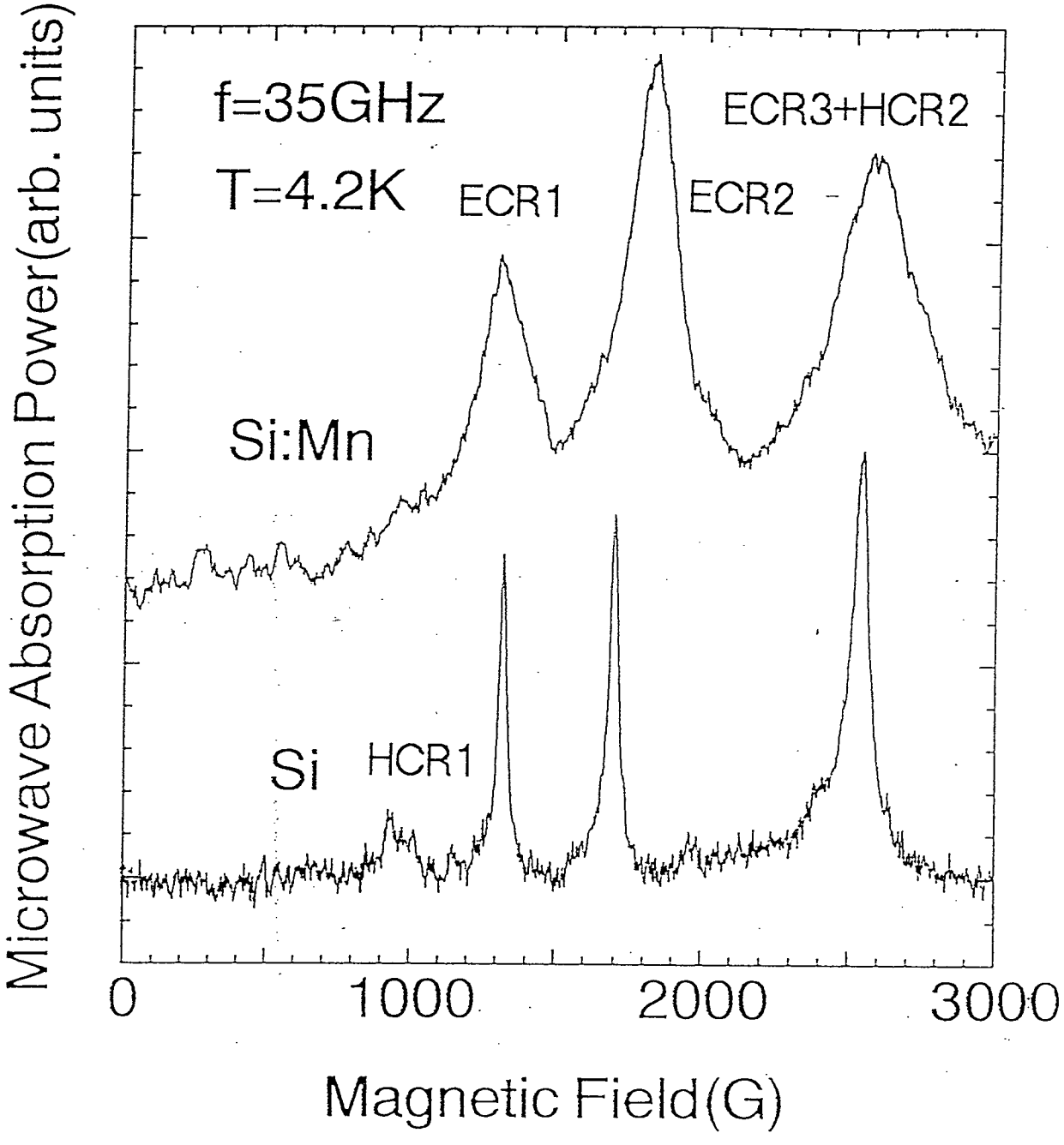
f=35GHz
T=4.2K
ECR1
ECR2
ECR3+HCR2
Si:Mn
Si
HCR1
Microwave Absorption Power(arb. units)
0
1000
2000
3000
Magnetic Field(G)

Figure 16

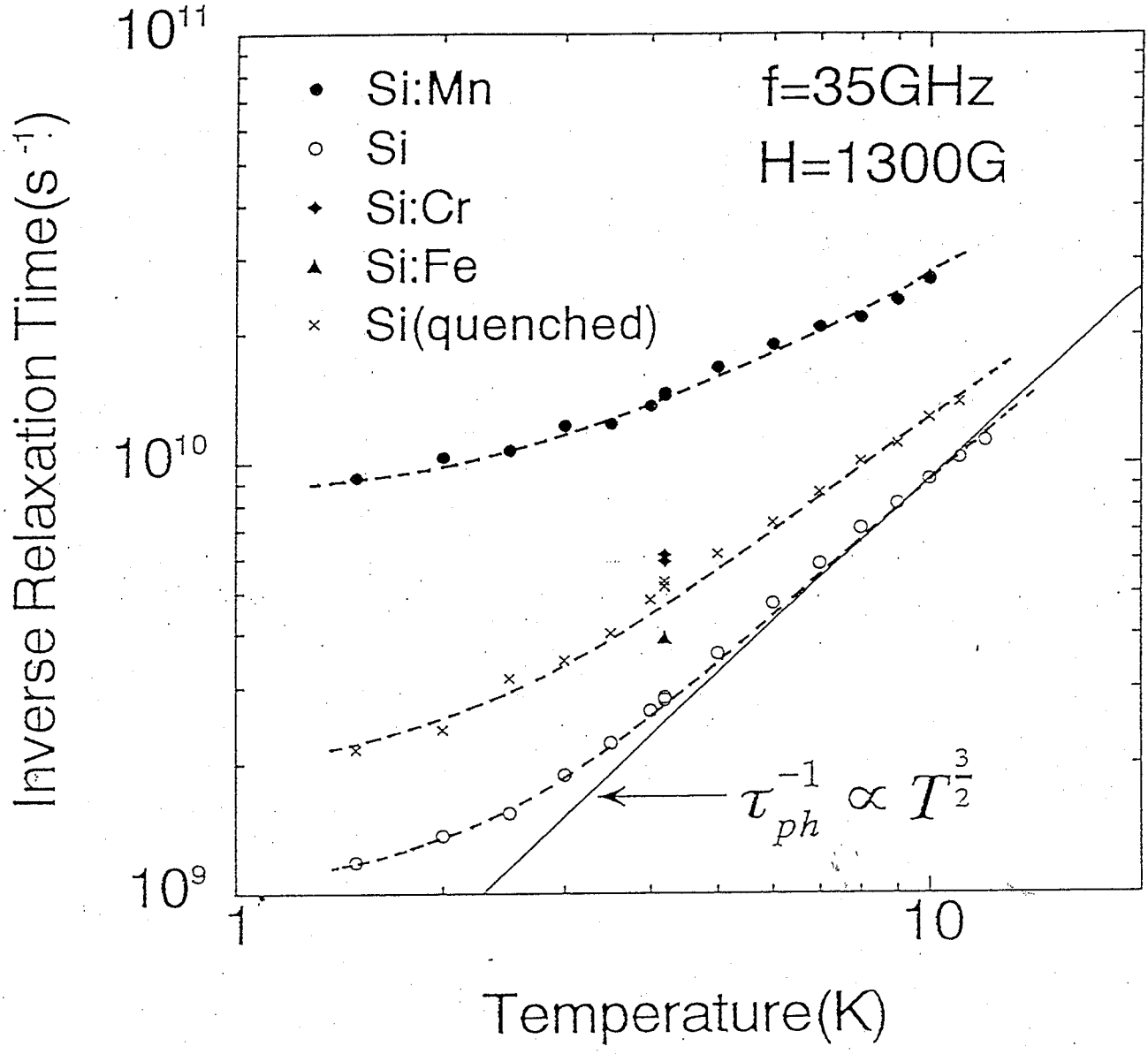
Inverse Relaxation Time(s^{-1})
10^{11}
10^{10}
10^{9}
1
10
Temperature(K)
Si:Mn
Si
Si:Cr
Si:Fe
Si(quenched)
f=35GHz
H=1300G
$\tau_{ph}^{-1} \propto T^{\frac{3}{2}}$

Figure 17

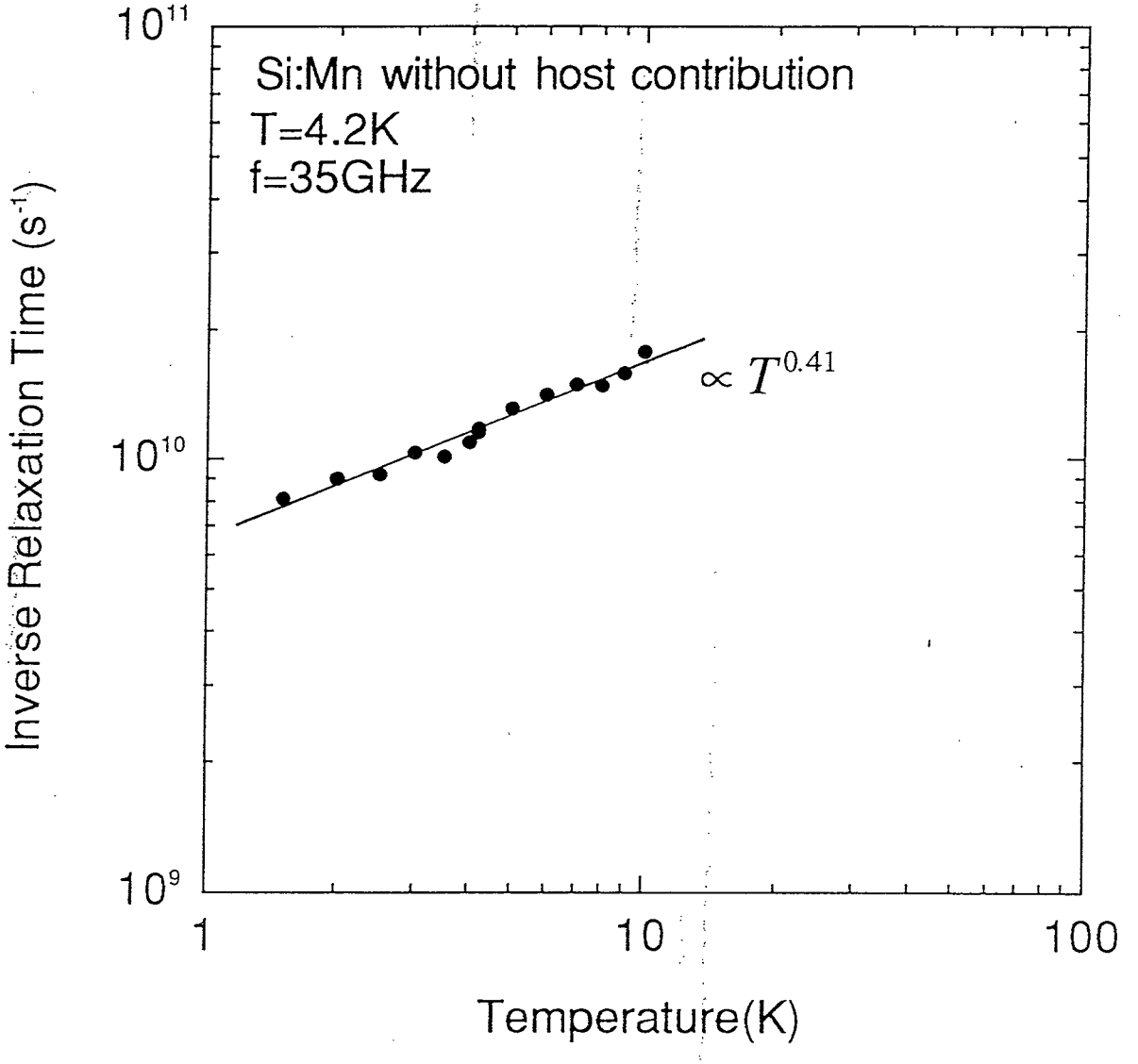
Si:Mn without host contribution
T=4.2K
f=35GHz
$\propto T^{0.41}$
Inverse Relaxation Time (s^{-1})
10^{11}
10^{10}
10^{9}
1
10
100
Temperature(K)

Figure 18

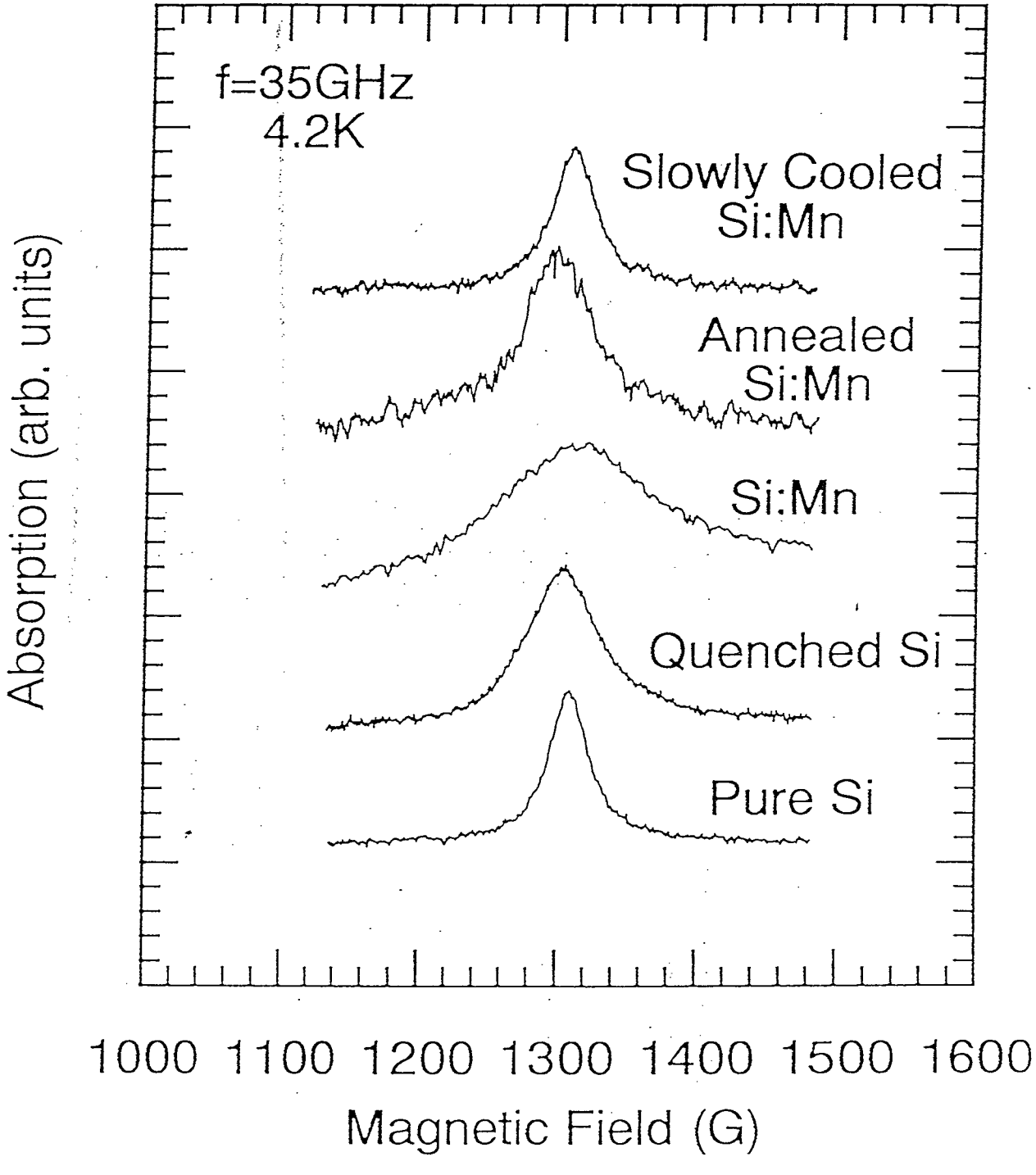
f=35GHz
4.2K
Slowly Cooled
Si:Mn
Annealed
Si:Mn
Si:Mn
Quenched Si
Pure Si
Absorption (arb. units)
1000 1100 1200 1300 1400 1500 1600
Magnetic Field (G)

Figure 19

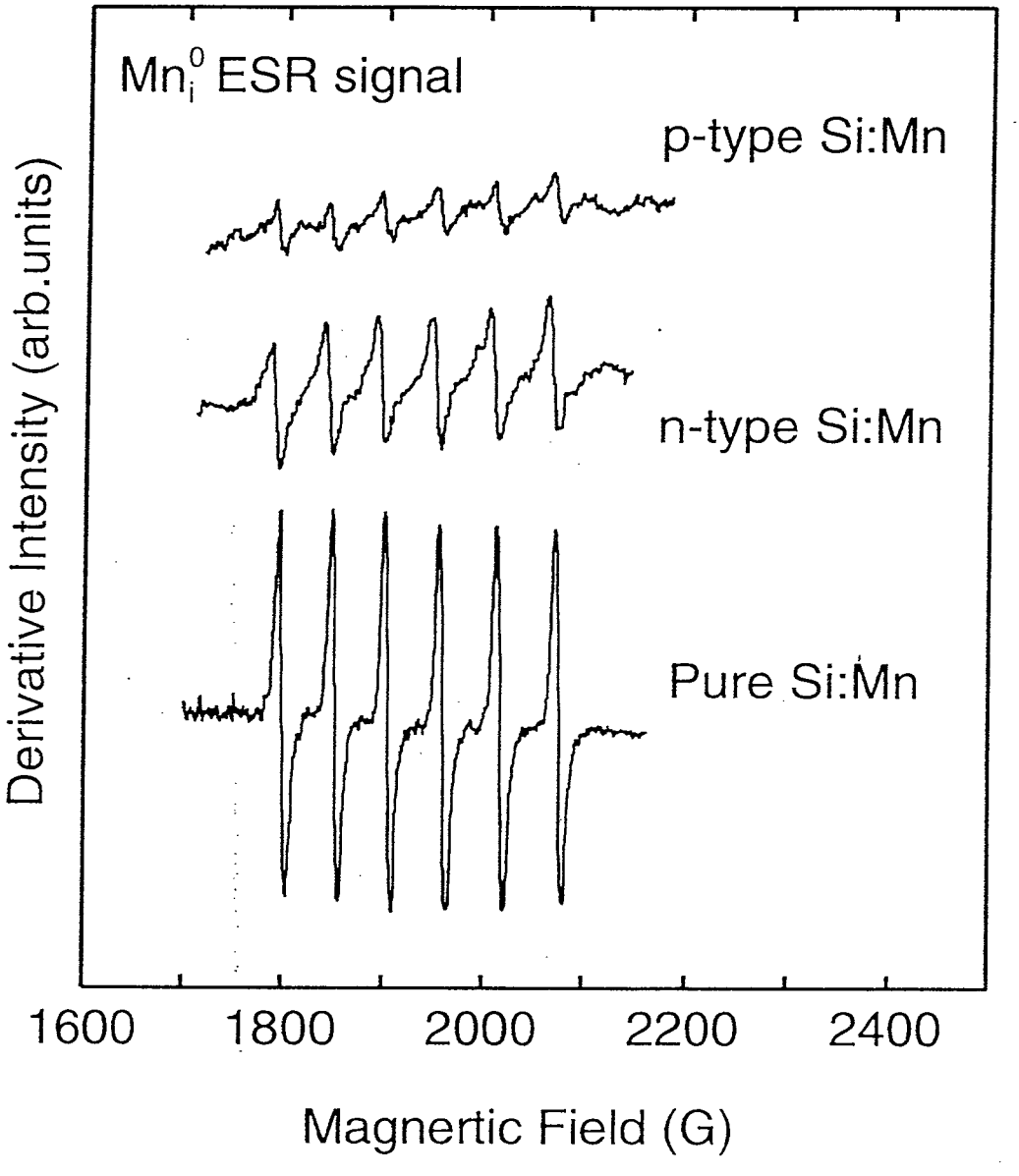
Mn_i^0 ESR signal
p-type Si:Mn
n-type Si:Mn
Pure Si:Mn
Derivative Intensity (arb.units)
1600
1800
2000
2200
2400
Magnertic Field (G)

Figure 20

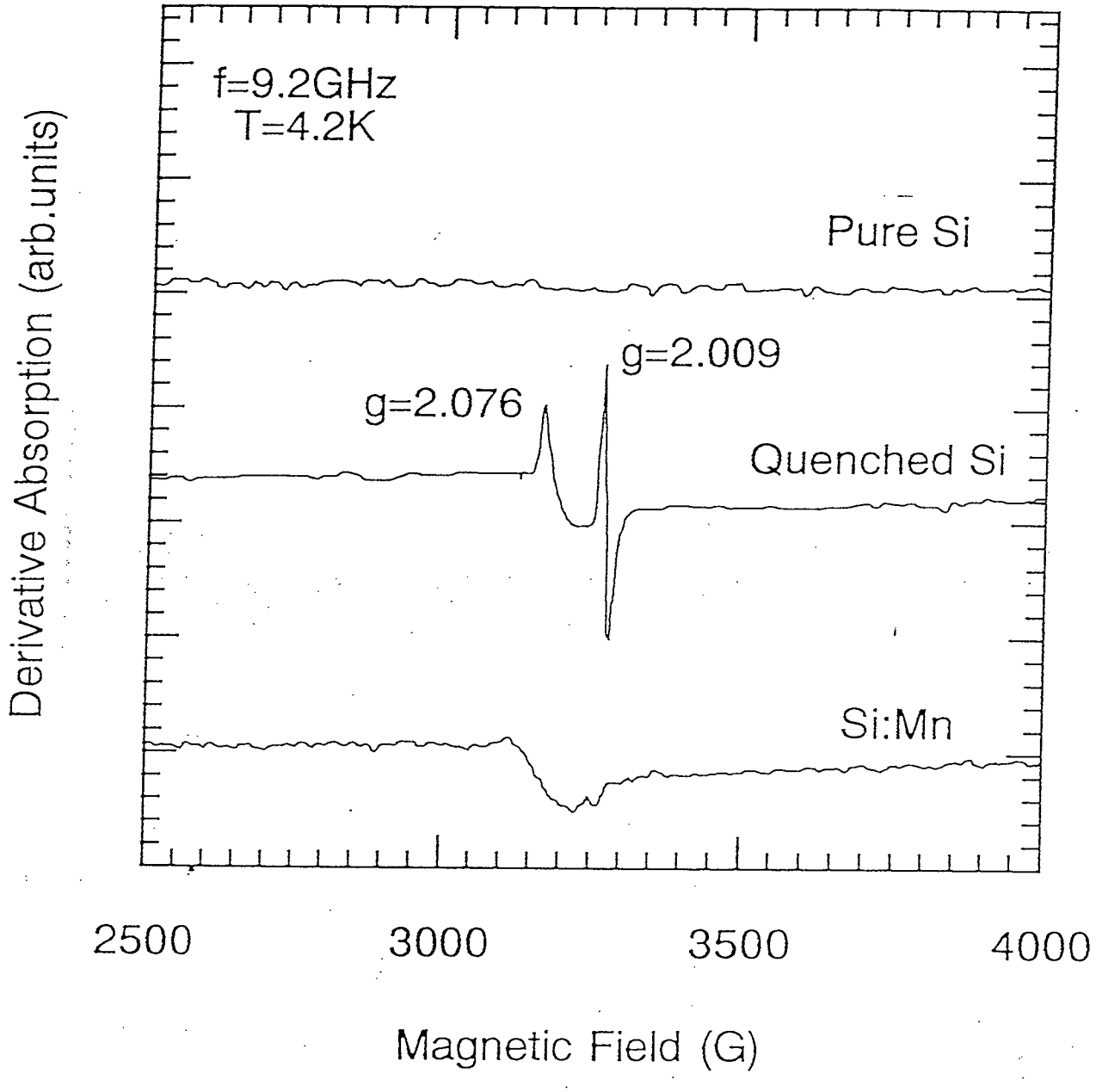
f=9.2GHz
T=4.2K
Pure Si
g=2.009
g=2.076
Quenched Si
Si:Mn
Derivative Absorption (arb.units)
2500
3000
3500
4000
Magnetic Field (G)

Figure 21

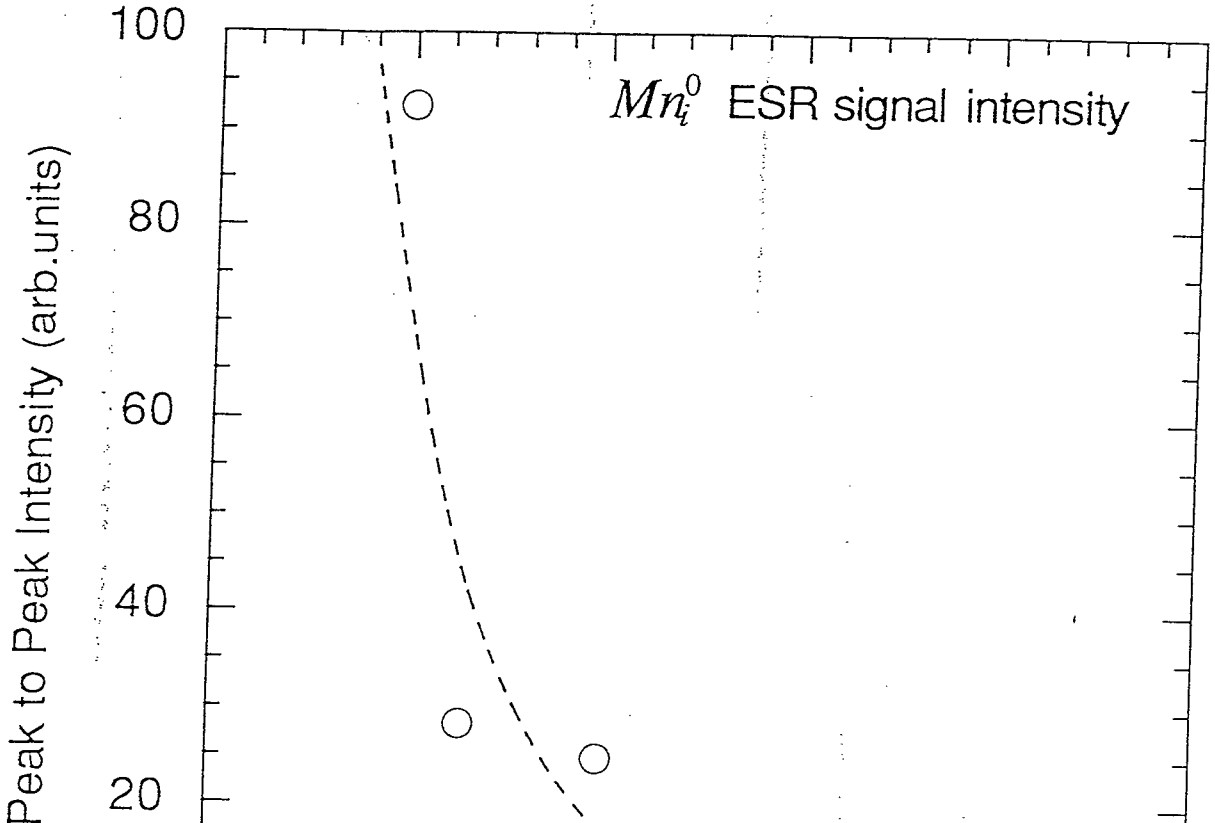
100
80
60
40
20
0
Mn_i^0 ESR signal intensity
Peak to Peak Intensity (arb.units)
3
4
5
6
7
8
Temperature(K)

Figure 22

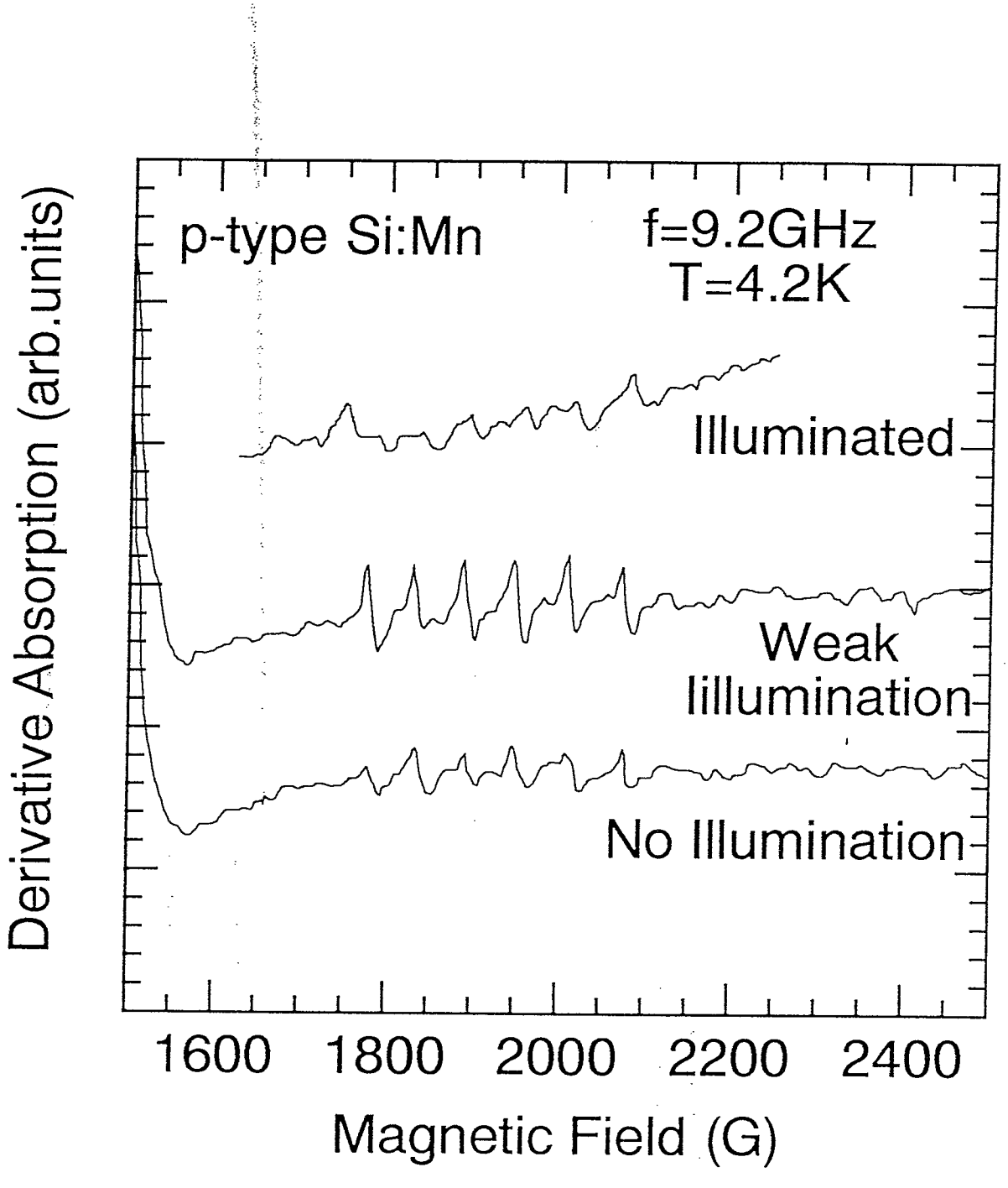
p-type Si:Mn
f=9.2GHz
T=4.2K
Illuminated
Weak
Illumination
No Illumination
Derivative Absorption (arb.units)
1600
1800
2000
2200
2400
Magnetic Field (G)

Figure 23

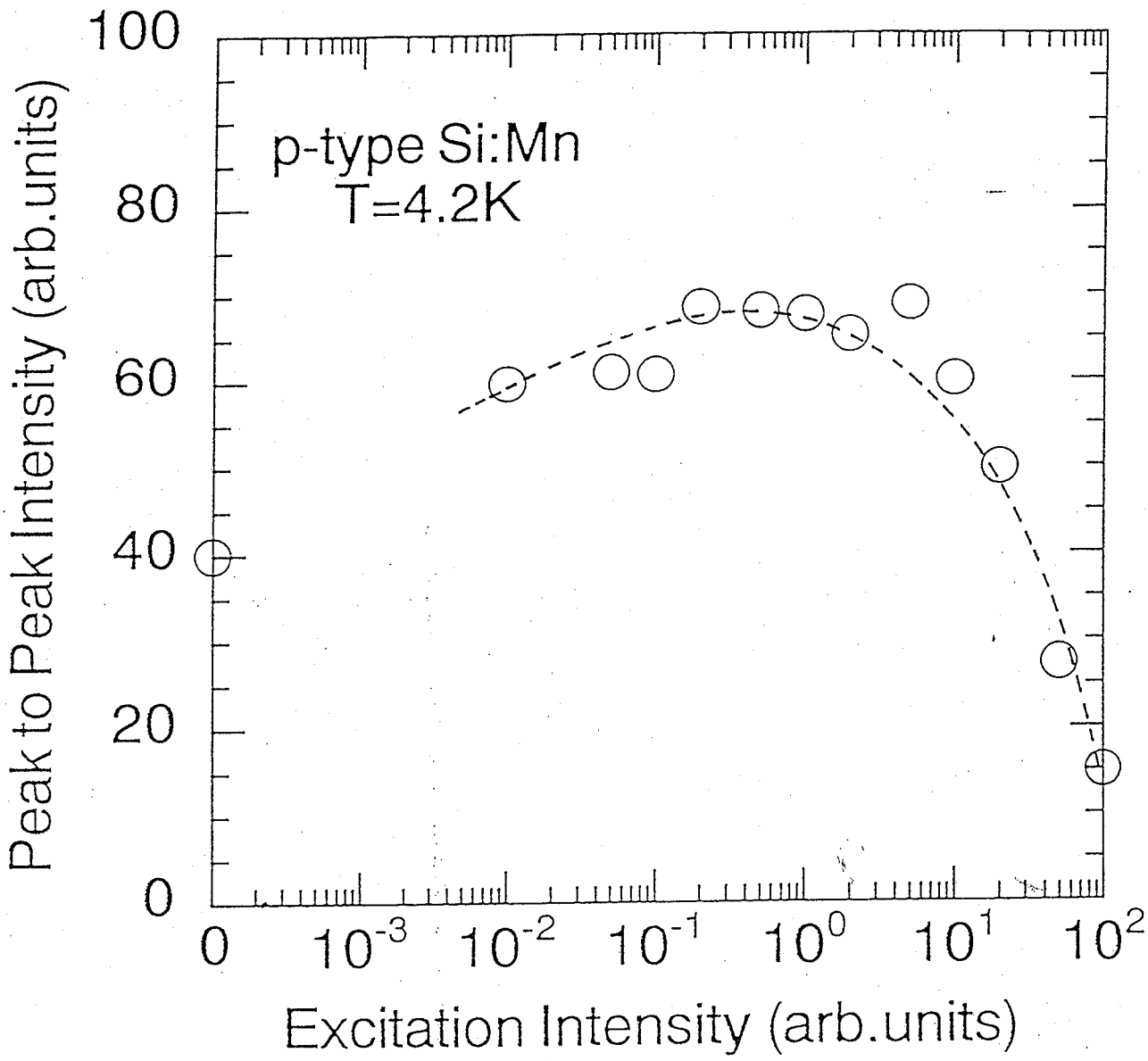
p-type Si:Mn
T=4.2K
Peak to Peak Intensity (arb.units)
Excitation Intensity (arb.units)
100
80
60
40
20
0
0
10^{-3}
10^{-2}
10^{-1}
10^{0}
10^{1}
10^{2}

Figure 24

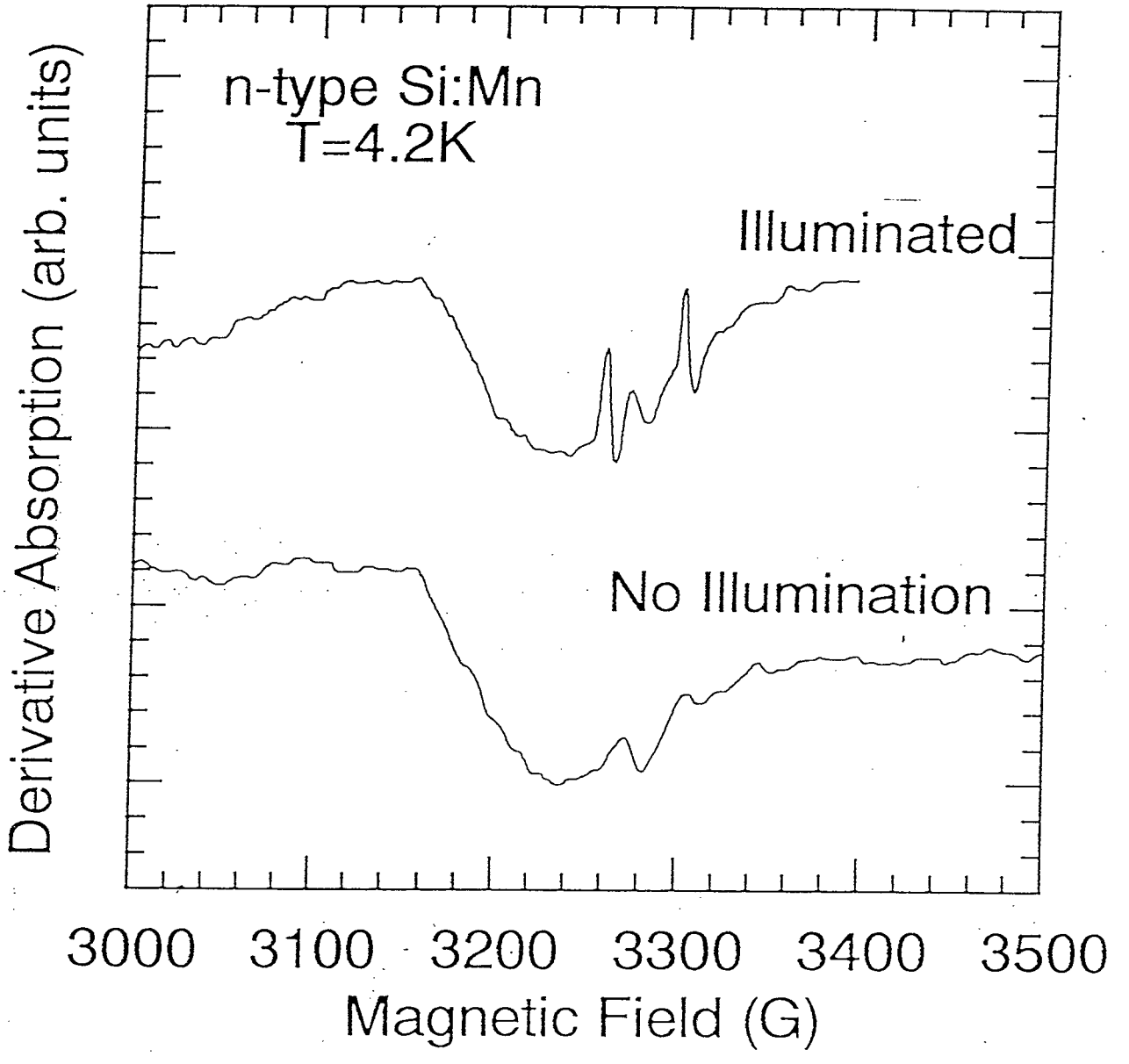
n-type Si:Mn
T=4.2K
Illuminated
No Illumination
Derivative Absorption (arb. units)
3000
3100
3200
3300
3400
3500
Magnetic Field (G)

Figure 25

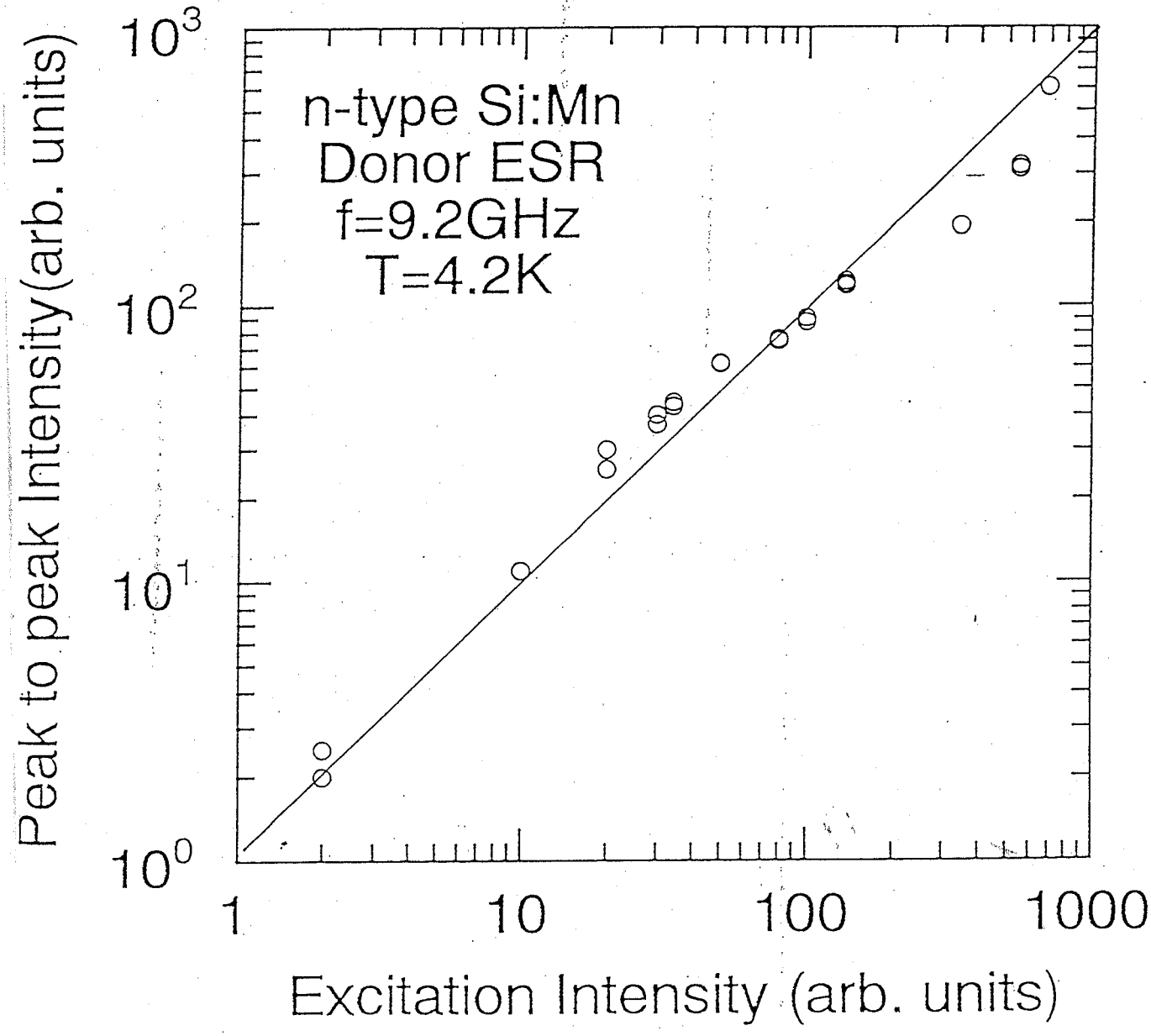
n-type Si:Mn
Donor ESR
f=9.2GHz
T=4.2K
Peak to peak Intensity(arb. units)
Excitation Intensity (arb. units)
10^3
10^2
10^1
10^0
1
10
100
1000

Figure 26

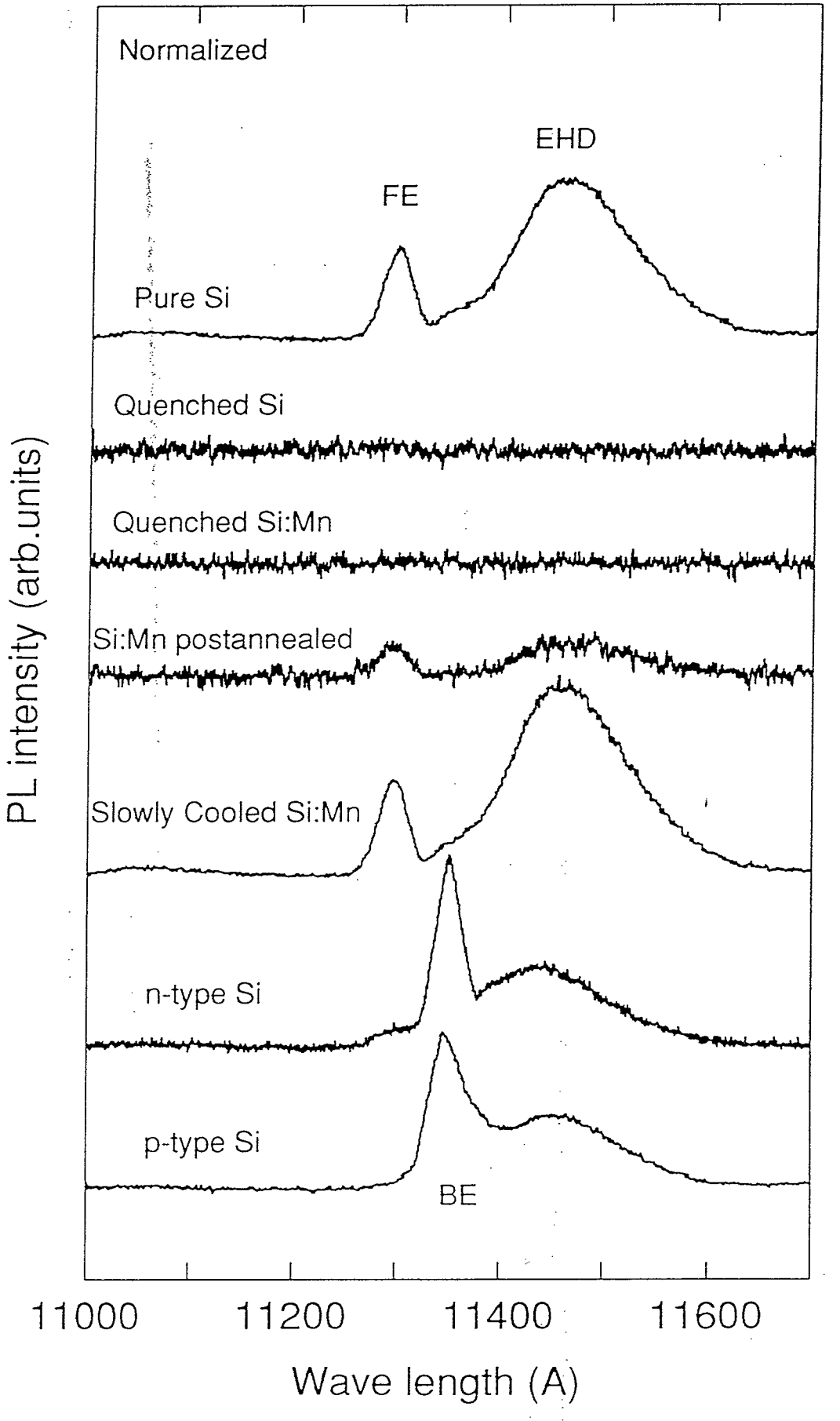
Normalized
EHD
FE
Pure Si
Quenched Si
Quenched Si:Mn
Si:Mn postannealed
Slowly Cooled Si:Mn
n-type Si
p-type Si
BE
PL intensity (arb.units)
11000
11200
11400
11600
Wave length (A)

Figure 27

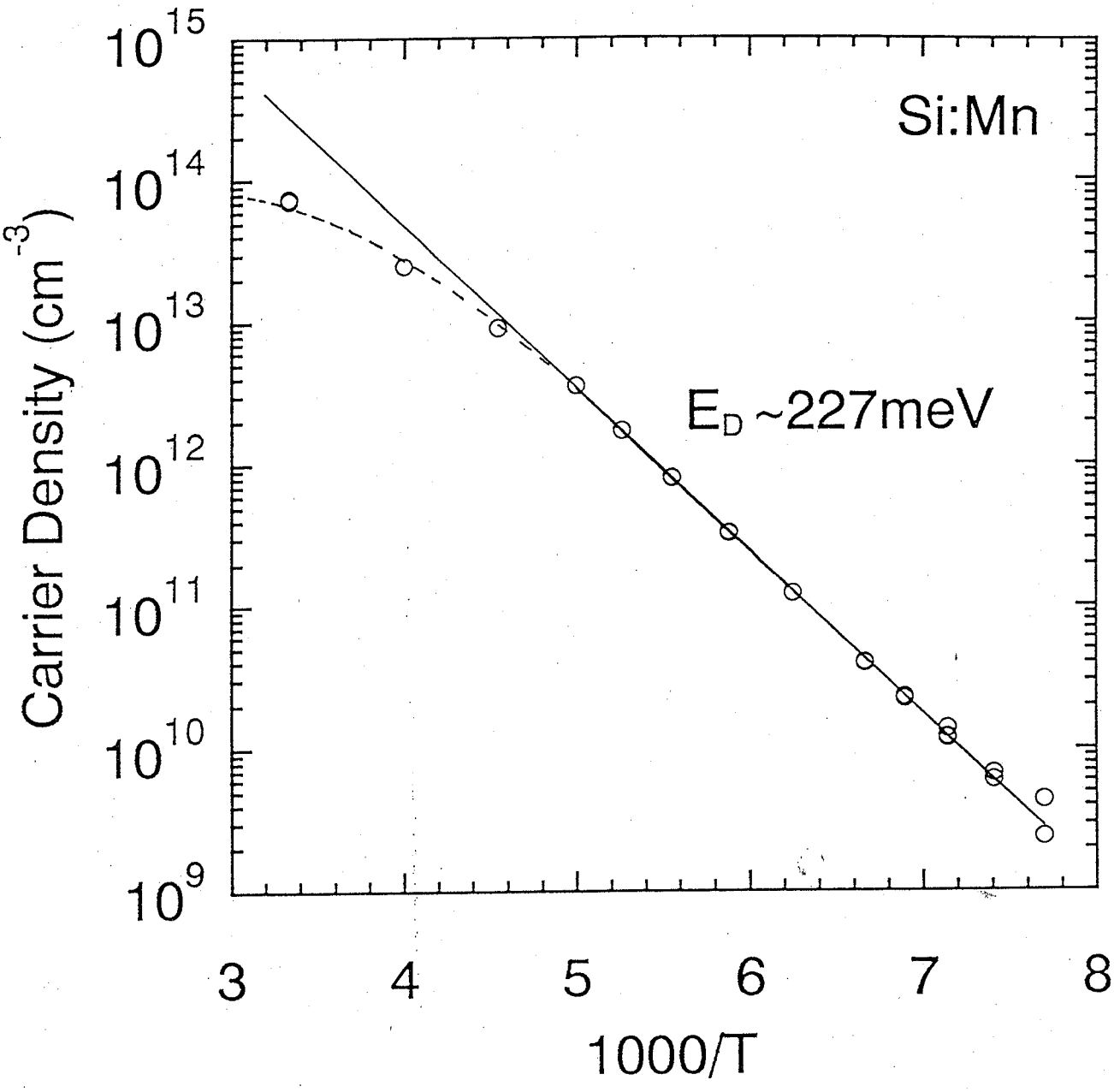
Si:Mn
E_D ~227meV
Carrier Density (cm^{-3})
10^{15}
10^{14}
10^{13}
10^{12}
10^{11}
10^{10}
10^{9}
3
4
5
6
7
8
1000/T

Figure 28

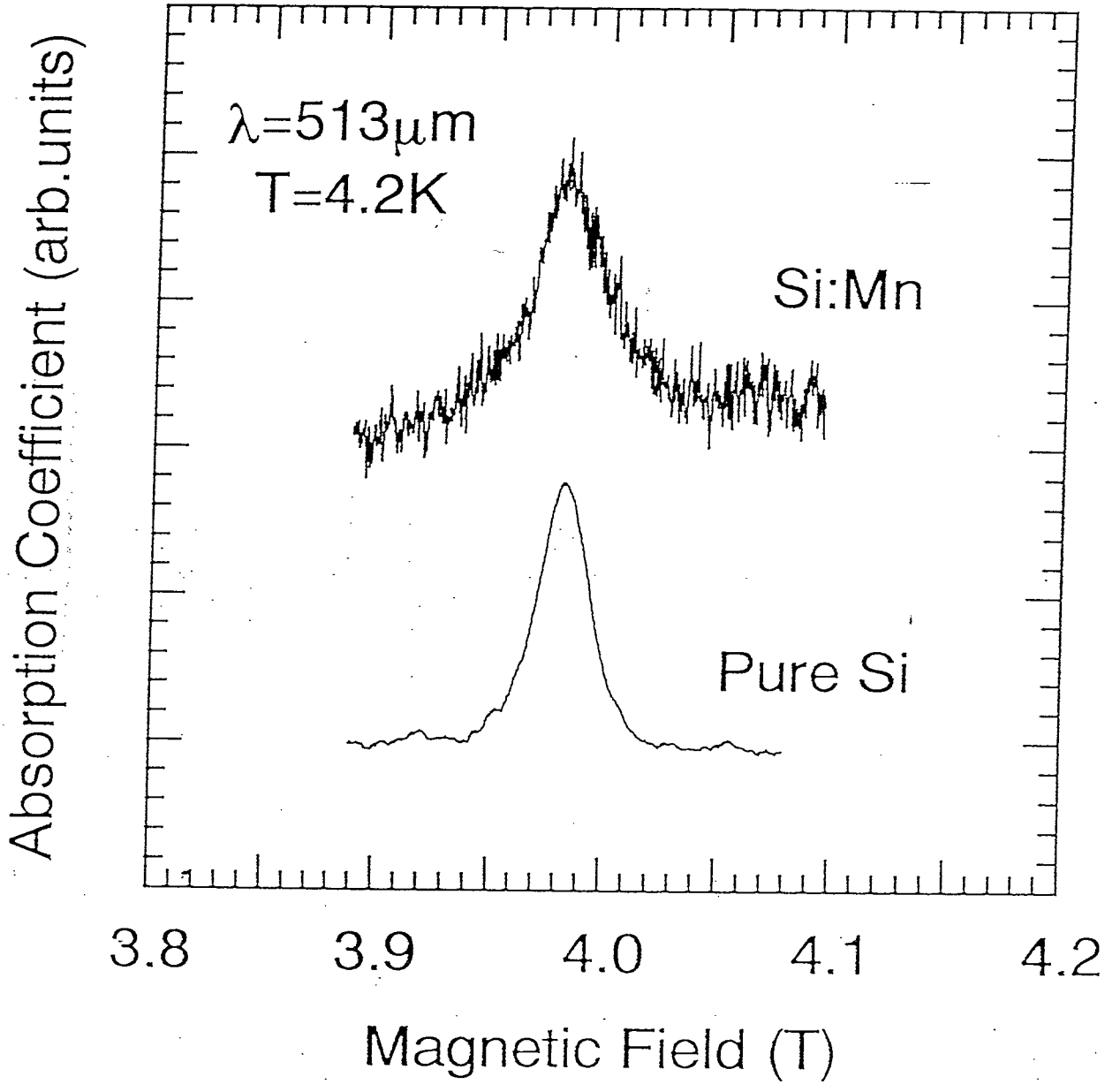
λ=513μm
T=4.2K
Si:Mn
Pure Si
Absorption Coefficient (arb.units)
3.8
3.9
4.0
4.1
4.2
Magnetic Field (T)

Figure 29

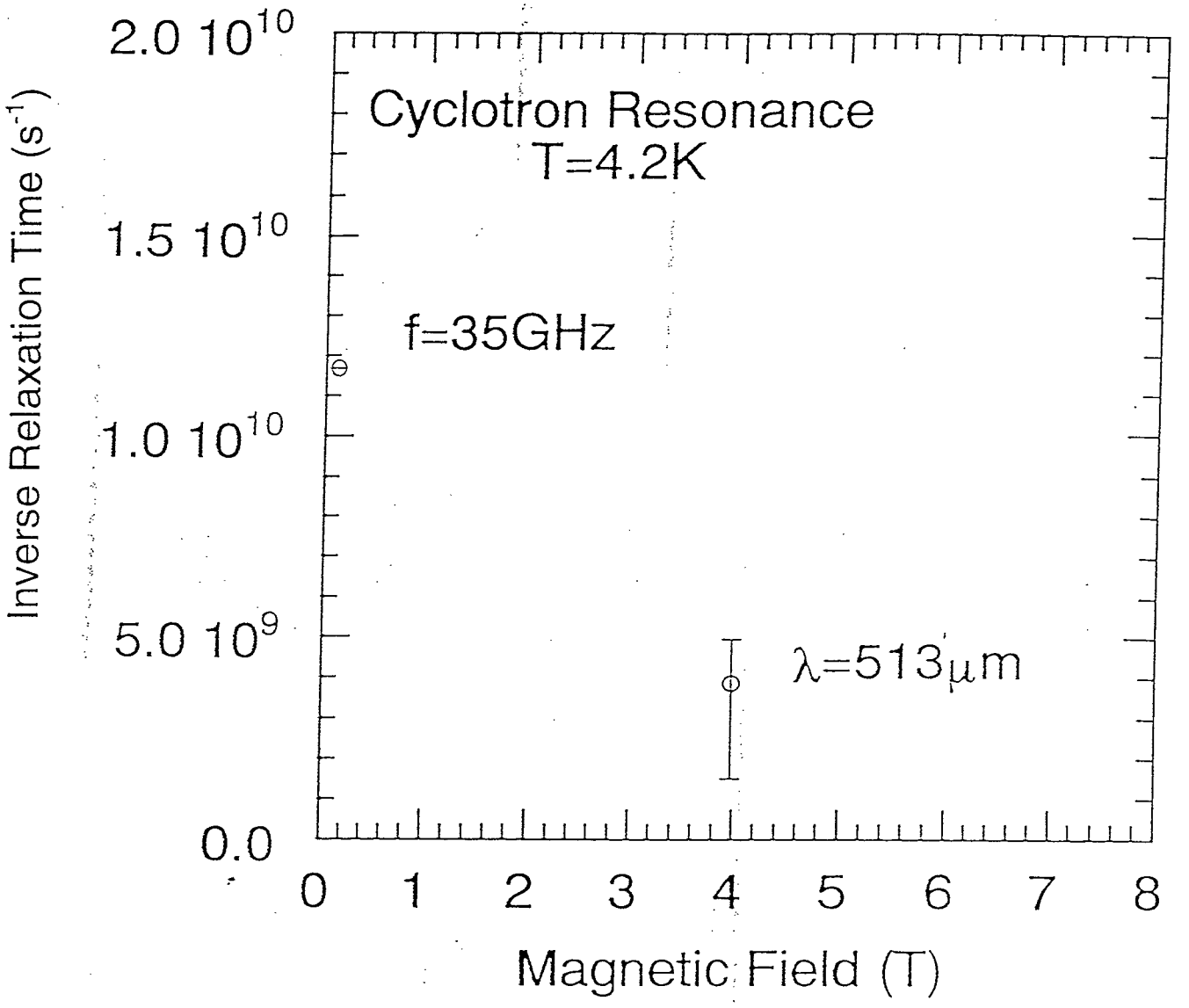
Cyclotron Resonance
T=4.2K
f=35GHz
λ=513μm
Inverse Relaxation Time (s-1)
2.0 10^10
1.5 10^10
1.0 10^10
5.0 10^9
0.0
0 1 2 3 4 5 6 7 8
Magnetic Field (T)

Figure 30

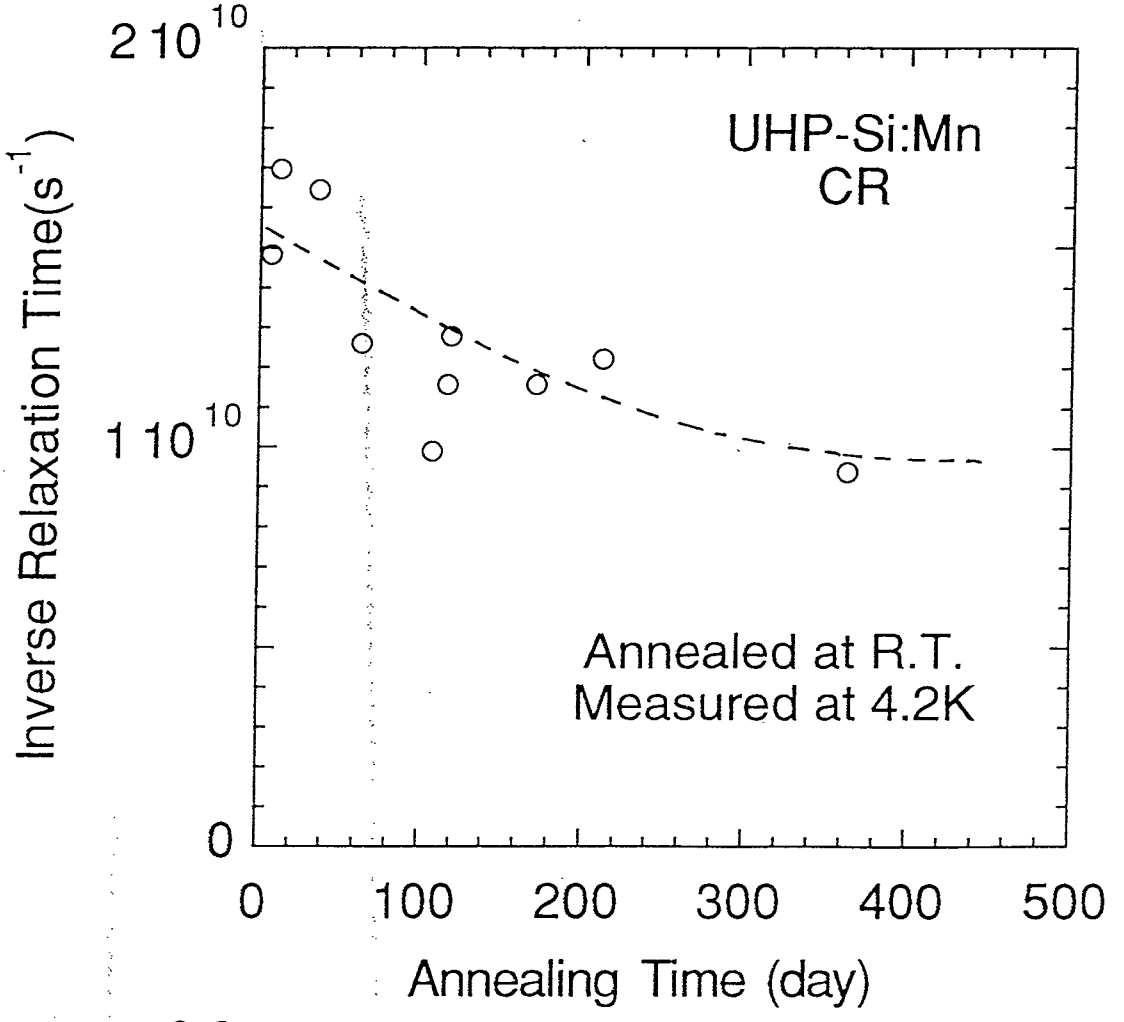
2 10^10
1 10^10
0
Inverse Relaxation Time(s^-1)
UHP-Si:Mn
CR
Annealed at R.T.
Measured at 4.2K
0
100
200
300
400
500
Annealing Time (day)

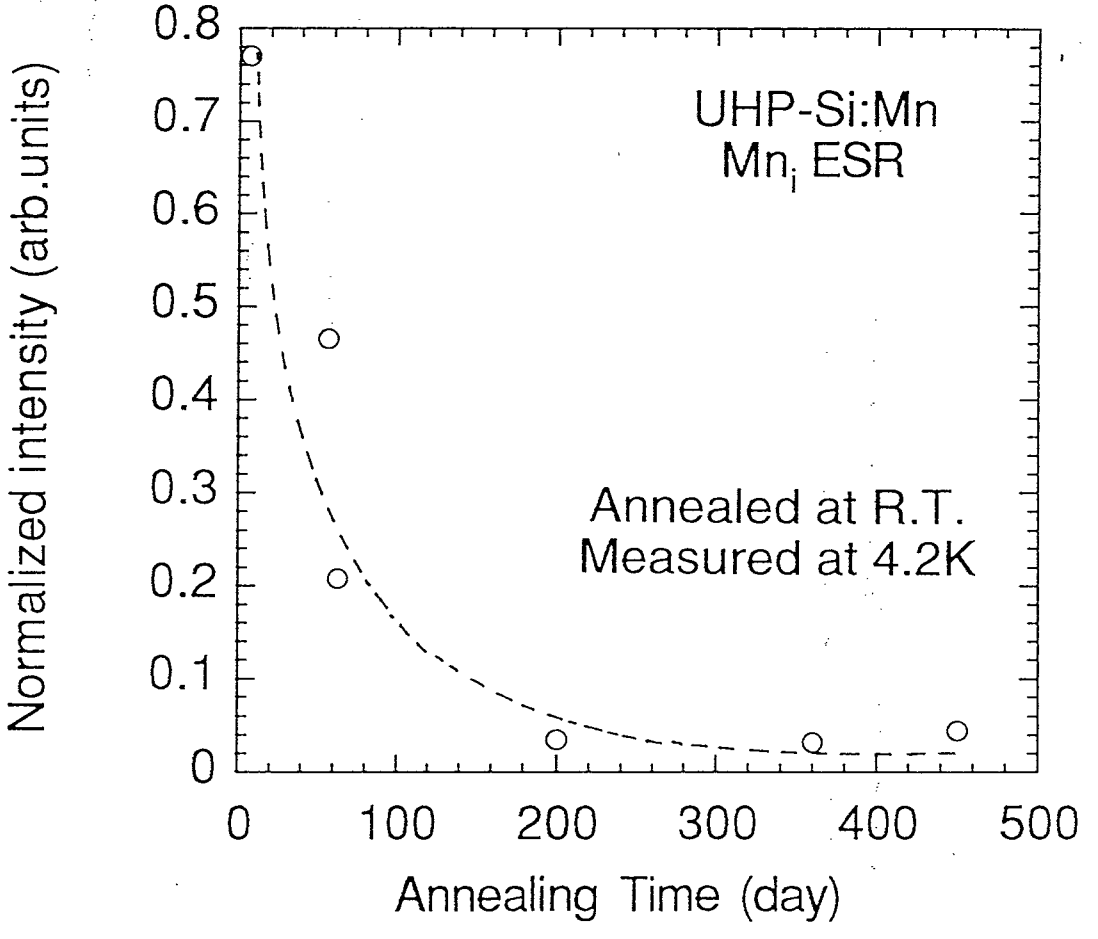
0.8
0.7
0.6
0.5
0.4
0.3
0.2
0.1
0
Normalized intensity (arb.units)
UHP-Si:Mn
Mn_i ESR
Annealed at R.T.
Measured at 4.2K
0
100
200
300
400
500
Annealing Time (day)

Figure 31

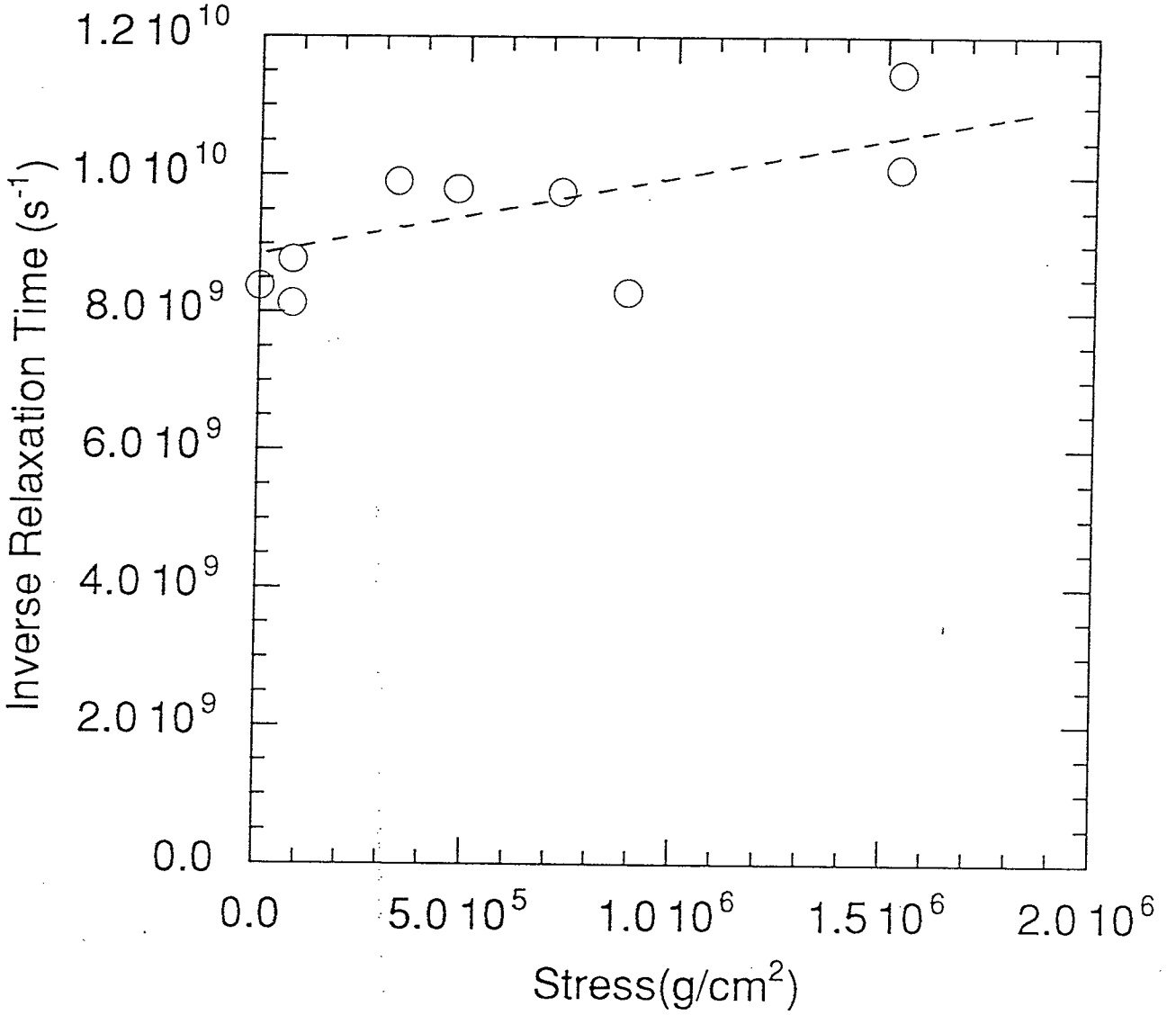
1.2 10^10
1.0 10^10
8.0 10^9
6.0 10^9
4.0 10^9
2.0 10^9
0.0
Inverse Relaxation Time (s^-1)
0.0
5.0 10^5
1.0 10^6
1.5 10^6
2.0 10^6
Stress(g/cm^2)

Figure 32

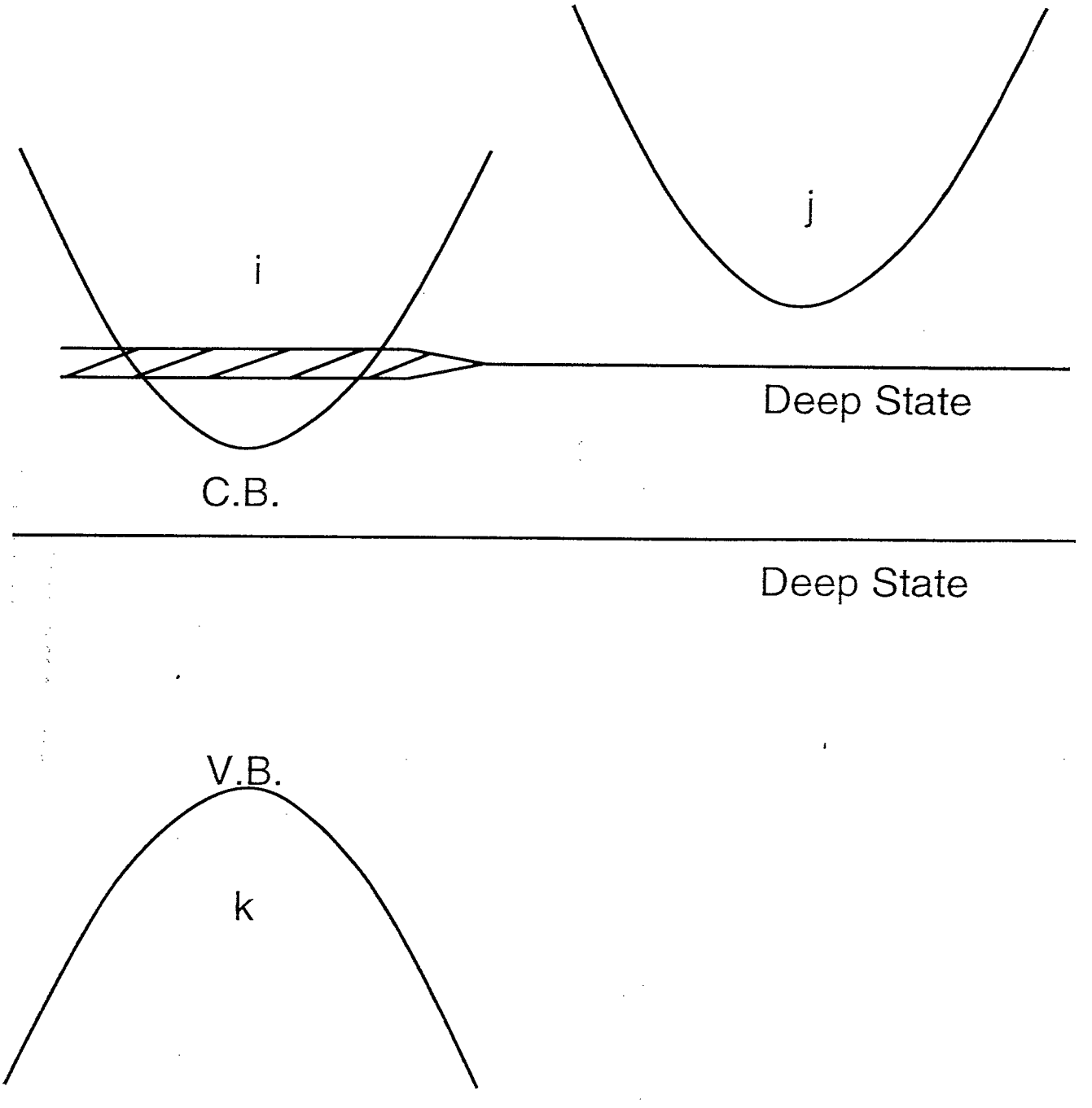

Figure 33

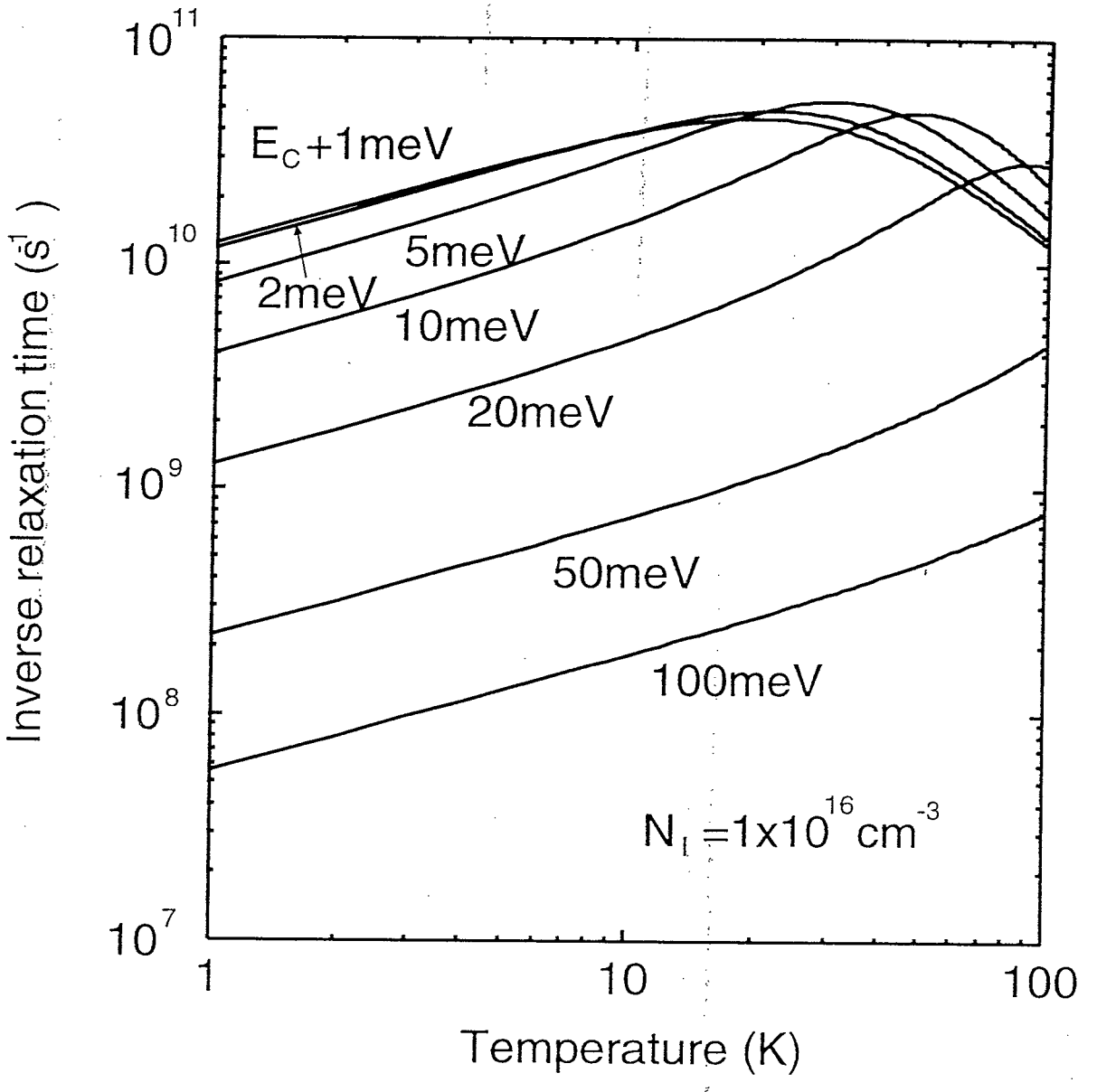
10^{11}
10^{10}
10^{9}
10^{8}
10^{7}
Inverse relaxation time (s^{-1})
E_C+1meV
5meV
2meV
10meV
20meV
50meV
100meV
N_I =1x10^{16} cm^{-3}
1
10
100
Temperature (K)

Figure 34

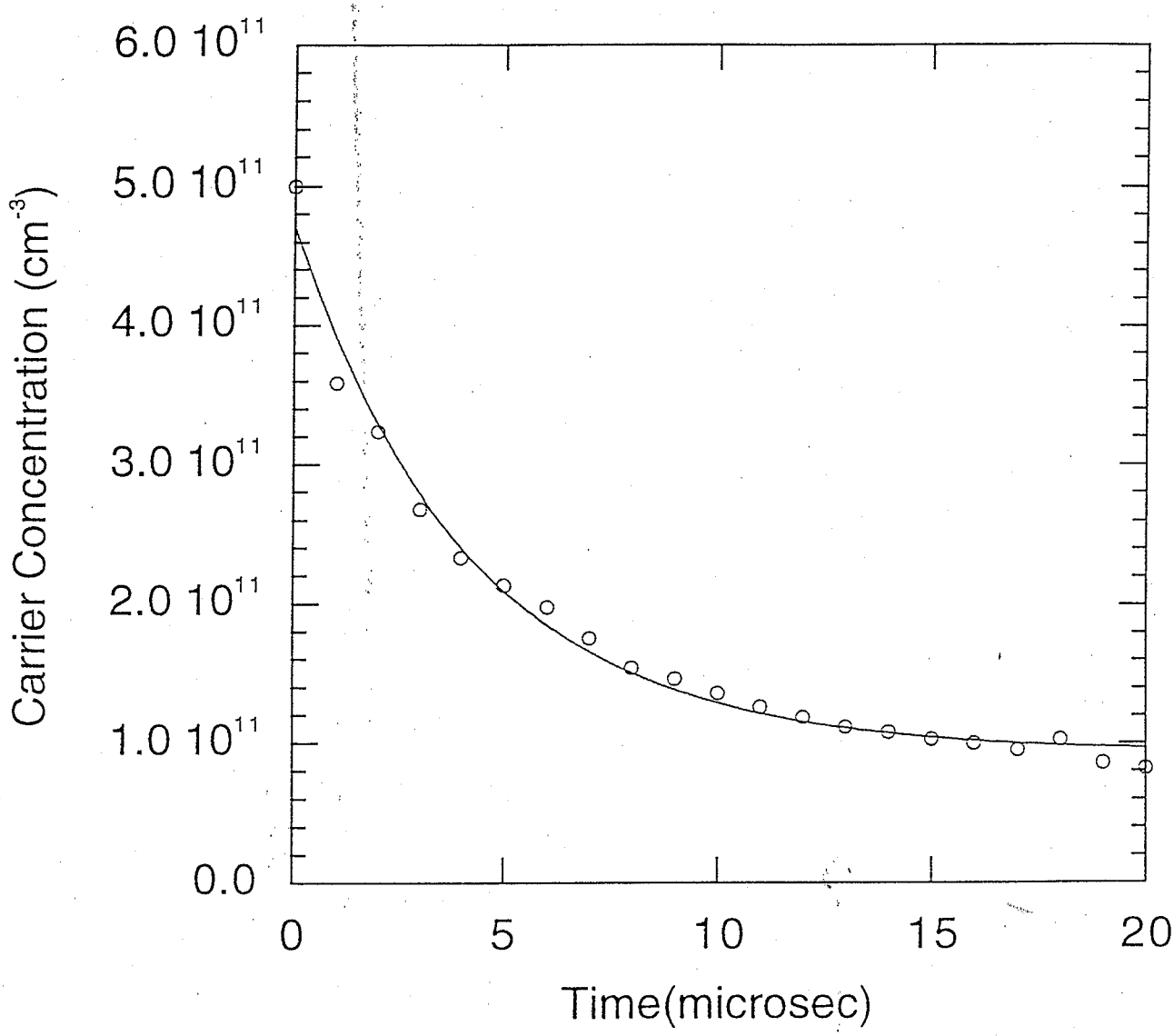
6.0 10^11
5.0 10^11
4.0 10^11
3.0 10^11
2.0 10^11
1.0 10^11
0.0
Carrier Concentration (cm^-3)
0
5
10
15
20
Time(microsec)

Figure 35

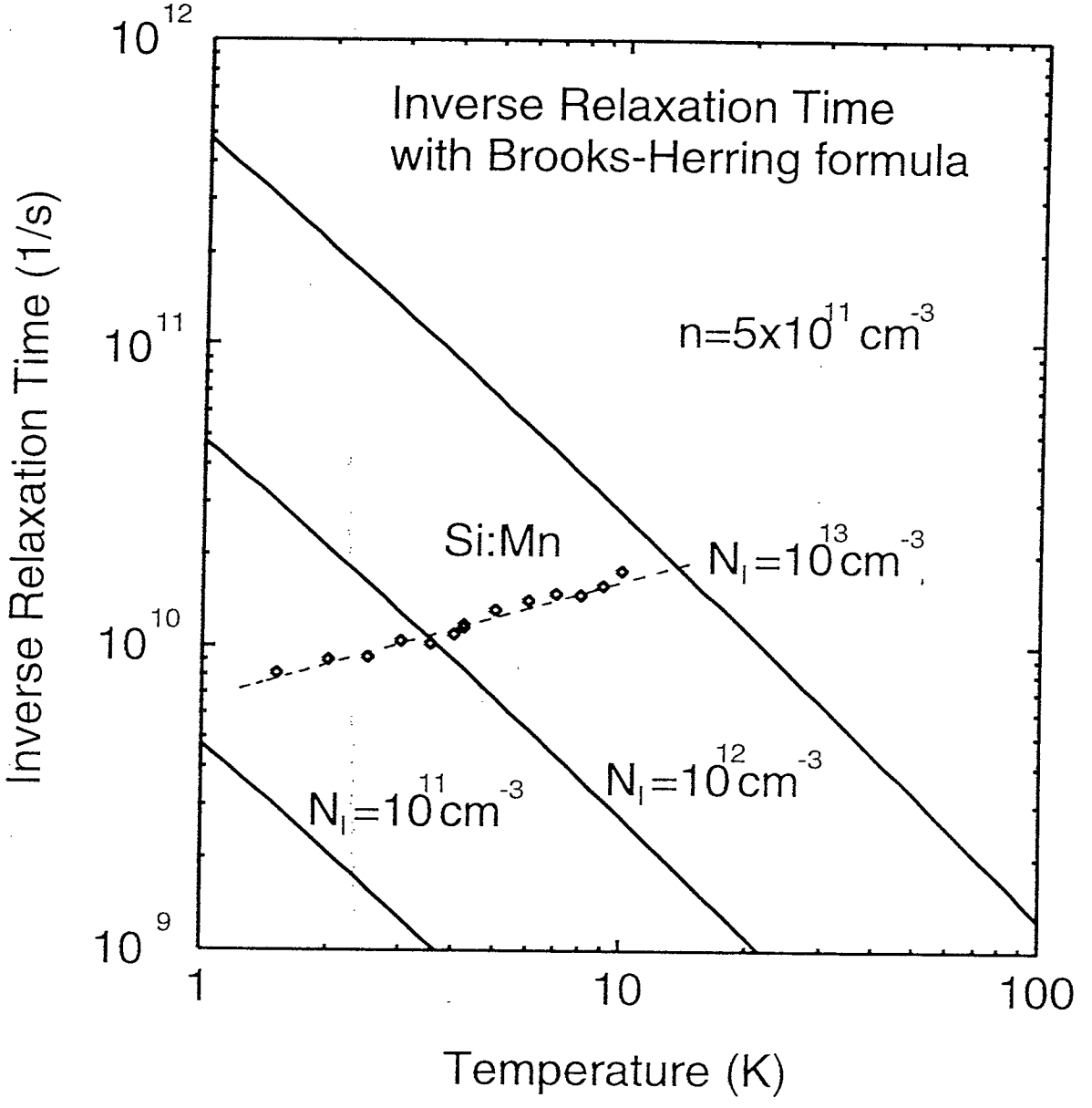
Inverse Relaxation Time
with Brooks-Herring formula
n=5x10^11 cm^-3
Si:Mn
N_I=10^13 cm^-3
N_I=10^12 cm^-3
N_I=10^11 cm^-3
Inverse Relaxation Time (1/s)
Temperature (K)
10^12
10^11
10^10
10^9
1
10
100

Figure 36

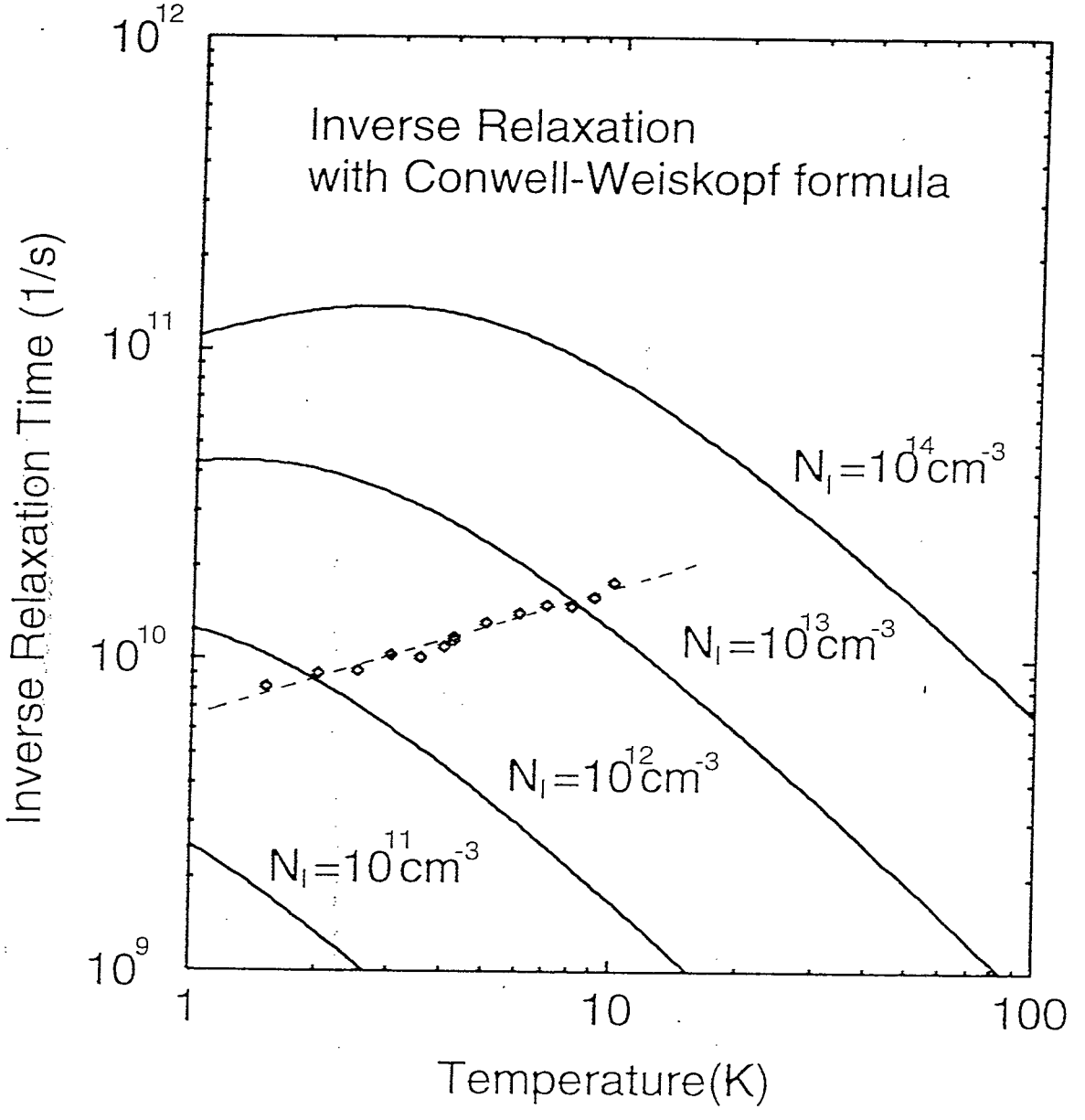
Inverse Relaxation
with Conwell-Weiskopf formula
Inverse Relaxation Time (1/s)
Temperature(K)
10^{12}
10^{11}
10^{10}
10^{9}
1
10
100
$N_I=10^{14}cm^{-3}$
$N_I=10^{13}cm^{-3}$
$N_I=10^{12}cm^{-3}$
$N_I=10^{11}cm^{-3}$

Figure 37